EXPERIMENTAL INVESTIGATIONS OF FLOW AND FILM COOLING WITH ENDWALL CONTOURING AND BLADE TIP EJECTION UNDER ROTATING TURBINE CONDITIONS

A Dissertation

by

MOHSEN REZASOLTANI

Submitted to the Office of Graduate and Professional Studies of
Texas A&M University
in partial fulfillment of the requirements for the degree of

DOCTOR OF PHILOSOPHY

Chair of Committee,	Meinhard Taher Schobeiri
Co-Chair of Committee,	Je-Chin Han
Committee Members,	Robert A. Handler
	Hamn-Ching Chen
Head of Department,	Andreas A. Polycrapou

December 2015

Major Subject: Mechanical Engineering

ABSTRACT

Very limited experimental data is available for aerodynamic and film cooling effectiveness under rotating condition in the literature. As a result, there is a strong need to study in detail and discover essential features of turbine platform and blade tip film cooling under engine representative flow and rotating conditions. This dissertation deals with the specific heat transfer and aerodynamics problematic inherent to high pressure (HP) turbine sections.

Major efficiency improvement has been achieved by introducing a completely new endwall contouring technology which decreases the strength of the secondary flow vortices. Efficiency measurements show for the contoured rotor a maximum efficiency of 89.9% compared to the reference non-contoured case of $\eta_{t-s} = 88.86\%$. This is an efficiency increase of $\eta_{t-s} = 1.04\%$.

The new method of endwall contouring not only has improved the turbine aerodynamic efficiency but it also has substantially improved the film cooling effectiveness of the contoured endwall. The film cooling experiments were carried out using pressure sensitive paint (PSP) measurement technique. Measurements were conducted for three coolant-to-mainstream mass flow ratios (MFR) of 0.5%, 1.0% and 1.5%. Film cooling data is also obtained for three rotational speeds, 3000 rpm (reference condition), 2550 rpm and 2400 rpm and they are compared with non-contoured endwall

data. For 3000 rpm two more coolant to mainstream mass flow ratio of 0.75% and 1.25% are performed to have a better view of how film cooling effectiveness is changing. Comparing experimental results of the film cooling effectiveness investigations of the contoured case with the reference non-contoured case, clearly shows the improving effect of contouring on film cooling effectiveness for all cases investigated in this report.

Four different blade tip ejection configurations were utilized to determine the impact of the hole arrangements on the film cooling effectiveness. plane tip with tip hole cooling, squealer tip with tip hole cooling, plane tip with pressure-side-edge compound angle hole cooling and squealer tip with pressure-side-edge compound angle hole cooling. To avoid rotor imbalance, every pair is installed radially. Film cooling effectiveness measurements were performed for three blowing ratios (M) of 0.75, 1.25 and 1.75. Film cooling data was also obtained for three rotational speeds; 3000 rpm (reference condition), 2550 rpm and 2000 rpm. Film cooling measurements were performed using pressure sensitive paint (PSP) technique.

The experimental investigations were performed in the three-stage multi-purpose turbine research facility at the Turbomachinery Performance and Flow Research Laboratory (TPFL), Texas A&M University.

DEDICATION

I dedicate my dissertation to my father, Hossein, who is fighting against bone marrow cancer for six years. I couldn't have gotten here without his encouragement and love. I love you dad. Keep fighting and BTHO cancer.

I also dedicate this work to my best friend Hoda, the kindest wife, and my wonderful son Rosstin for being there for me. <3 <3

ACKNOWLEDGEMENTS

I would like to thank my committee chair, Dr. Schobeiri, my committee co-chair, Dr. Han, and my committee members, Dr. Handlers, and Dr. Chen, for their guidance and support throughout the course of this research.

Thanks also go to my friends and colleagues and the department faculty and staff for making my time at Texas A&M University a great experience. I also want to extend my gratitude to Toshiba International Corp. by donating a 350 HP VFD to the Turbomachinery Performance and Flow Research Laboratory (TPFL).

Finally, thanks to my mother and father for their encouragement and to my wife for her patience and love.

NOMENCLATURE

C	Oxygen concentration
C_x	Axial chord length of the rotor blade (C_x=4.16 cm)
D	Mass Diffusion Coefficient (m^2/s)
f (P_{ratio})	Relation between intensity ratio and pressure ratio
G	Mass flux ($kg/m^2 - s$)
I	Pixel intensity for an image
LE	Leading edge of the blade
M	Average blowing ratio ($=\rho_c V_c / \rho_m W_2$)
MFR	Mass Flow Ratio (% of mainstream core flow)
M_r	Relative Mach number
PS	Pressure Surface
SS	Suction Surface
T_c	Stator-Rotor gap Coolant temperature (K)
T_f	Local film temperature (K)
T	temperature (K)
U	Tangential average velocity (m/s)
V	Average absolute velocity of mainstream air (m/s)
V_u	Tangential component of absolute velocity (m/s)

W	Relative average velocity of mainstream air (m/s)
P_{O_2}	Partial pressure of oxygen
P_t	Total pressure (Pa)
P_{tr}	Relative total pressure (Pa)
V_c	Avg. velocity of coolant air from the stator-rotor gap (m/s)
DR	Coolant-to-mainstream density ratio
MW	Molecular weight of gas
Re	Reynolds number, $V_2 Chord/\nu$

Greek symbols

α	Absolute velocity flow angle (°)
β	Relative velocity flow angle (°)
η	Local film-cooling effectiveness
ν	Kinematic viscosity
ρ	Density (kg/m^3)
$\eta_{t\text{-}s}$	total-to-static efficiency
α_D	Thermal diffusivity (m^2/s)
ϵ	Turbulent diffusivity
ω	Turbine rotational speed (rad/s)

Subscripts

∞	Pertaining to mainstream (outside film)
air	Mainstream air along with air as coolant
aw	Adiabatic Wall
mix	Mainstream air along with nitrogen as coolant
ref	Reference image with no mainstream and coolant flow
blk	Image without illumination (black)
C	Coolant
m	Mainstream
M	Pertaining to mass transfer
X	Pertaining to x co-ordinate direction
Y	Pertaining to y co-ordinate direction

TABLE OF CONTENTS

Page

Page

Page

LIST OF FIGURES

Page

Page

Page

Page

Page

Page

Page

LIST OF TABLES

Page

1. INTRODUCTION AND LITERATURE REVIEW*

1.1. Turbine Aerodynamic Research

Improvements in instrumentation and measurement techniques lead to regularly updated, more accurate findings in the field of aerodynamic measurement and analysis of gas turbines. These findings allow design engineers to design machines that have greater efficiencies. Secondary flow in the rotor tip and hub region is a major source of inefficiency in turbomachines. This flow generates vortices that induce drag forces, reducing the total pressure of the mainstream. Mainstream flow near the hub is also negatively impacted by the low energy boundary layer flow as well as cross flow across the blade pressure and suction surfaces on the rotor hub. Mitigation of these losses could increase efficiency, resulting in large energy savings. However, the 3-D nature of these secondary flow factors makes measurement difficult and complicated. Nevertheless, researchers have made several attempts to measure and quantify characteristics of these secondary flows in order to understand how they affect turbine performance.

* Part of the materials are reprinted with permission from "A Combined Experimental and Numerical Study of the Turbine Blade Tip Film Cooling Effectiveness under Rotation Condition" by Mohsen Rezasoltani, Kun Lu, Meinhard T. Schobeiri and Je-Chin Han, J. Turbomach. 2015; 137(5), Copyright © 2015 by ASME, and "Experimental Investigation of the Effect of Purge Flow on Film Cooling Effectiveness on a Rotating Turbine With Non-Axisymmetric Endwall Contouring," by M. Rezasoltani, M. T. Schobeiri and J. C. Han, J. Turbomach. 2014; 136(9), GT2013-94807, Copyright © 2014 by ASME.

The secondary flow and its impact on efficiency and performance of turbine components are described extensively by Lakshminarayana [1] and Schobeiri [2]. As explained in detail by Schobeiri [2] turbomachinery losses can be divided into endwall or secondary losses, profile losses and leakage losses. Profile loss is considered loss effects due to boundary layer development on suction and pressure surfaces of the blade in question. Analyses for profile loss often assume a primarily two dimensional flow, and losses at the trailing edge are often included into the profile loss category. Endwall losses are commonly referred to as secondary flow losses and arise due to secondary flows generated as the annulus boundary layers in the blade passage. Tip leakage losses arise from leakage type flows across the blade tip for a rotor or stator hub, and depend on whether the blades utilize shrouds or do not. Leakage flows as stated by [3] interact strongly with the secondary flow patterns in the passage, thus it is generally considered that there is large degree interplay between the various types of losses encountered in turbomachinery.

Denton [3] gave an overview of the effects of different flow mechanisms including the secondary flow on turbomachinery losses. The platform surface is characterized by a highly complex 3-D flow due to the viscous nature of the mainstream hot gases. A detailed model of the different types of vortices generated and the nature of the secondary flow on the platform surface has been put forth by several people in the past (Langston et al. [4], Goldstein and Spores [5], Sieverding et al. [6], and Wang et al. [7]). The measured flow pattern observed by Langston [4] is shown in Figure 1.

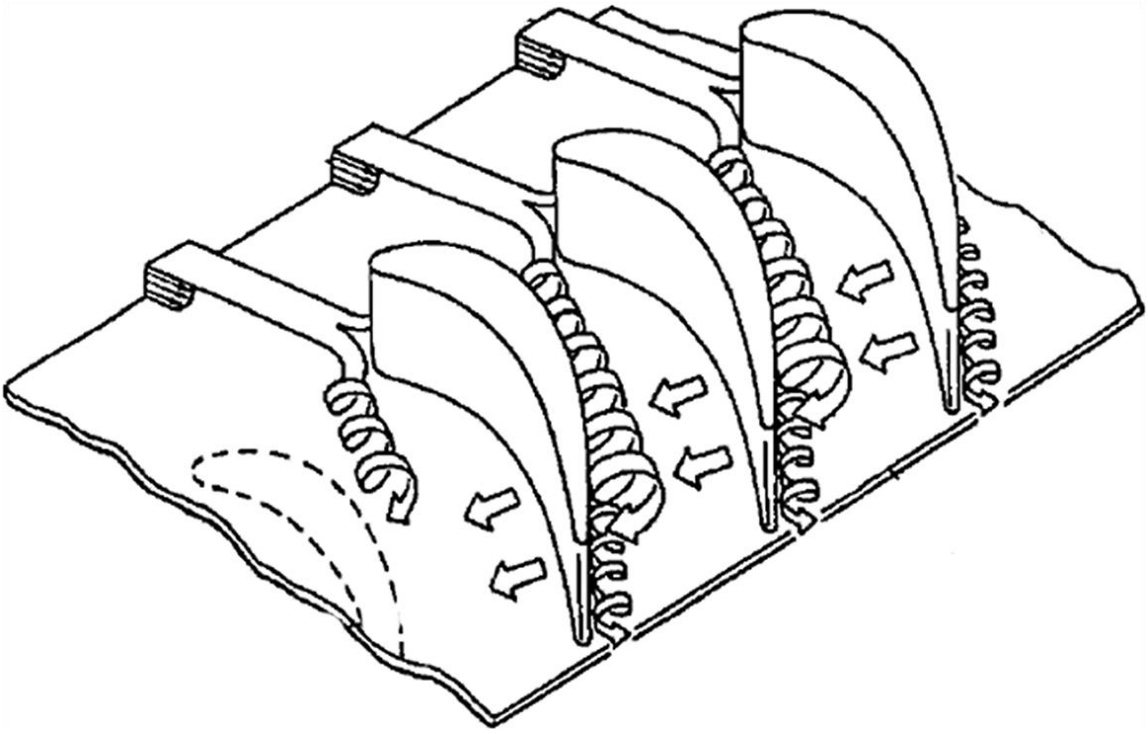

Figure 1: Turbine cascade vortex flow pattern by Langston [4]

The mechanism of formation of the tip leakage in the gap over unshrouded rotor blades and its further development in the blade-to-blade passage is illustrated in Figure 2. The driving force for this type of leakage is the pressure difference that is formed over the blade tip between the pressure and suction surface of the blade. Due to a usually significant pressure gradient, the leakage stream is largely accelerated in the tip gap. The cross-flow blocked by the development of the tip leakage vortex also separates from the endwall and rolls up into a passage vortex. The stream dividing line between the tip leakage and cross-passage flow lies at the pressure side of the blade tip.

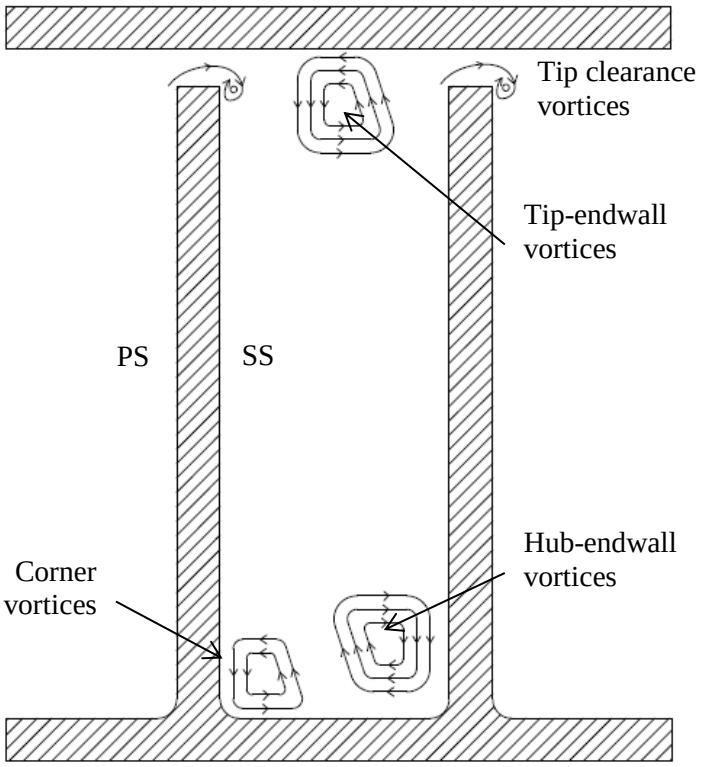

Figure 2: Tip leakage vortices at the tip and hub endwall in rotor blades [2]

1.2. Endwall Contouring Research

Focusing on the secondary flow loss mechanisms, the fluid particles within the endwall boundary layers are exposed to a pitchwise pressure gradient in the blade channel. The particles move from the pressure side to the suction side and generate a system of vortices. These vortices induce drag forces that are the cause of the secondary flow losses. In addition, their interaction with the main flow causes angle deviation inside and outside the blade channel, resulting in additional losses due to angle deviation [8].

The secondary flow loss is almost inversely proportional to the aspect ratio [2]. Thus, in HP-turbines with small aspect ratios, the secondary flow loss of almost 40-50% is the major loss contributor. It can be reduced by introducing the following measures:

1) Three-dimensional compound lean design [9]
2) Special design for turbines that are subjected to extreme off-design incidence change [10]
3) Modification of the blade leading edge using fillets [11]
4) Endwall contouring [12, 13]
5) Hub cooling mass flow injection to interact with the hub secondary flow
6) Blade tip cooling ejection to reduce the tip secondary flow losses

In recent years, numerous papers have been published that deal with the effect of endwall contouring and leading edge filleting. With a few exceptions of rotating rig investigations that deal with the endwall contouring of LP-turbines, most of the published studies are either numerically or experimentally performed in turbine cascades with steady inlet flow conditions. Numerical and experimental studies by [12], [13], [14] and [11] show a reduction of total pressure losses by as much as 50%.

Cascade Endwall: The papers discussed in this section represent a few among many that are dealing with the impact of endwall contouring on turbine endwall secondary flow.

Experimental and numerical cascade flow study by Ingram et al. [13] showed the influence of end-wall profiling. Streamline curvature method was used to reduce the

local static pressure. The best end-wall profile tested has shown a 24% reduction in the secondary loss. Further investigations by Ingram et al. [15] designed a new 'aggressive' profiling of the endwall to produce a large reduction in loss possible. However, the experimental results, showed an increase of secondary flow loss. Saha and Acharya [16] combined two curves, one that varies in the streamwise direction while the other varies in the pitchwise direction. They created several contoured end-walls by varying the streamwise variation keeping the pitchwise curve constant. The results show that the contoured end-wall can reduce the secondary flow by decreasing radial pressure gradient.

Praisner et al. [17] studied the application of non-axisymmetric endwall contouring to mitigate the endwall losses of front- and aft loaded turbine blades. With flat endwalls, the front-loaded design showed significantly higher secondary losses than the aft-loaded and the reference conventional blades. To contour the endwall they used two-dimensional cubic splines in both pitch- and stream-wise directions along the endwall. The predicted loss reduction for the front loaded airfoil design was at 12% while the measured loss reduction was twice as high at 25%. The predicted and measured loss reductions for the reference blade were 4% and 10% respectively while a 5% row-loss reduction was predicted for the aft-loaded blade. The comparison between the CFD and experiments reveals that, while the CFD calculations predict the trends of flow modifications with endwall contouring, they lack a significant level of accuracy for individual flow features such as the passage vortex. Harvey et al. [18] and Hartland, et

al. [19] modified the endwall for the large-scale, low-speed rotor profile in a linear cascade. The endwall surface was created by the product of two curves in axial and circumferential directions. The axial profile was defined by a B-spline curve through six control points. The first three terms in the Fourier series were used to produce the perturbations in the circumferential direction. They reported a measured net total loss reduction by 20% and the net secondary loss by 30%. The CFD losses show little change. The experimental data show mixed-out losses, where the reductions with the profiled endwall were 15% in net total loss and 34% in secondary loss.

Rotating Turbine: In contrast to the tremendous multitude of the cascade endwall papers, from which only a few have been discussed above, there are only a few investigations of the impact on endwall contouring in rotating turbines. Brennan et al. [20] redesigned the HP turbine of the Rolls-Royce Trent 500 engine with the application of non-axisymmetric endwalls. The profiled end-wall shape was determined by six control stations which were fixed at specified axial distances along the mean camber line of the airfoil. The addition of profiling to the end-walls of the HP Turbine is predicted to reduce secondary loss by 0.24% of the NGV and by 0.16% for the Rotor. The total improvement in stage efficiency for the HP Turbine is therefore +0.4%.

Harvey et al. [21] redesigned the IP-turbine stage by applying non-axisymmetric endwalls to both the vane and blade passages. They reported an improvement in the stage efficiency of 0.9 ± 0.4% at the design point. Germain et al. [22] studied the improvement of efficiency of a one-and-half stage high work axial flow turbine by non-

axisymmetric endwall contouring. The endwalls have been designed using automatic numerical optimization by means of a Sequential Quadratic Programming (SQP) algorithm. Both hub and tip endwalls of the first stator as well as the hub endwall of the rotor were modified. The experimental results confirm the improvement of turbine efficiency, showing a total-to-total stage efficiency benefit of 1%±0.4%, while the improvement is underestimated by CFD. Snedden et al. [23, 24] utilized 5-hole probe measurements in a 1.5 stage low speed, model turbine in conjunction with computational fluid dynamics to gain a more detailed understanding of the influence of a generic endwall design. Results indicated a 0.4% improvement in total-to-total rotor and stage efficiency as a result of the application of the generic non-axisymmetric endwall contouring. However, at higher loading the rotor efficiency was reduced by 0.5%.

1.3. Endwall Film Cooling Research

Over the past five decades, the thermal efficiency of gas turbine engines has been continuously rising as a result of an increased turbine inlet temperature. In pursuit of higher thermal efficiencies, gas turbines are operated at 1st stage inlet temperatures around 1500˚C resulting in excessive thermal stresses on the turbine components. Continuous operation under high turbine inlet temperatures enhances the possibility of thermal failure of the hot gas path components [25]. Also, the non-uniform temperature profile of the gas exiting the combustion chambers further exposes the rotor platform to higher temperatures requiring effective thermal protection [26]. Figure 3 shows the appearance of the failed blades.

Figure 3: Failure of the first stage blade of GE-F5 [25]

Film cooling is an external cooling technique commonly used in conjunction with internal cooling to protect the turbine components from the mainstream hot gas. In film cooling, a portion of the coolant used for internal cooling is ejected through slots or discrete holes over the surface of the components that need thermal protection. The coolant thus ejected displaces the mainstream boundary layer creating a protective film on the surface of the exposed component. This isolates the hot mainstream gas from the metal surface and considerably decreases the magnitude of the temperatures the hot gas path components encounter.

Film cooling as an external cooling technique is also used to protect the hub platform from the mainstream hot gas. In this case, a portion of the secondary air stream used for rotor disc cooling is ejected through a circumferential gap over the surface of

the hub platform that needs thermal protection. The ejected coolant creates a protective film on the surface of the exposed platform. This isolates the hot mainstream gas from the metal platform surface and considerably decreases the magnitude of the platform temperatures. Due to the complex nature of experimental setup and data acquisition from a rotating rig platform, studies of the effect of purge flow on the platform film cooling effectiveness has been very rare. Using a three-stage research turbine with two independent cooling loops, Suryanarayanan et al. [27, 28] investigated the rotational effects of the purge flow on the hub platform film cooling effectiveness. Using the PSP measurement technique, the investigation reported in [27, 28] details the effects of the purge flow under rotating condition on the platform cooling effectiveness. Increasing the rotational speed from 1500 rpm to 2550 rpm increased the magnitude of local film cooling effectiveness for upstream stator-rotor gap injection. Also it was concluded that, as the coolant to mass flow ratio (MFR) of upstream injection was increased from 0.5% to 2.00%, the effectiveness magnitude and distribution on the platform surface increased. The coolant, from the upstream slot affected by the inlet flow incidence and passage vortex, tended to concentrate close to the blade suction side of the platform. The purge flow alone, however, did not provide sufficient film protection on the downstream region and along the pressure surface on the rotor platform for the coolant to mass flow ratios tested. To shield the downstream region and understand the effects of rotation on downstream hole coolant injection, the report presented in [27] focuses on measuring film cooling effectiveness on the first stage rotor platform of the same three-stage

research turbine using nine discrete film cooling holes for three rotational speeds and several blowing ratios. In addition, film cooling tests were also conducted with simultaneous upstream stator-rotor gap. The experiments were conducted using the PSP measurement technique.

As reported in the above studies, the experiments were performed on non-contoured endwalls. In contrast to a variety of published papers dealing with steady cascade purge flow effects, there are only a few papers that deal with the purge flow effect in conjunction with endwall contouring. Schuepbach et al. [29] and Jenny et al. [30] presented studies that contain experimental and computational data of a 1.5-stage high work axial turbine. In [29], the authors investigate the influence of purge flow on the performance of two different non-axisymmetric endwall and the axisymmetric baseline case. They indicate that the experimental total-to-total efficiency assessment reveals that the non-axisymmetric endwalls lose some of their benefit relative to the baseline case when purge is increased. The first endwall design loses 50% of the efficiency improvement seen with low suction, while the second endwall design exhibits 34% deterioration. The subsequent paper [30] presents an experimental and computational study of non-axisymmetric rotor endwall profiling in a low pressure turbine. According to the authors, the measured efficiency revealed a strong sensitivity of the total-to-total efficiency to purge flow. The experiments showed that an efficiency deficit of 1.3% per injected percent of purge flow for the shrouded low-pressure turbine

configuration with profiled endwalls investigated. The experiments revealed an 18% reduction of sensitivity to purge flow due to the endwall profiling.

1.4. Blade Tip Film Cooling Research

Turbine blade tip and near tip regions are typically difficult to cool, and are subjected to potential damage due to high thermal loads. For the unshrouded blade, failure of the blade tip is caused mainly by hot tip leakage flow entrained in the tip clearance. The leakage flow accelerates due to a pressure difference between both the pressure and suction sides of the blade, causing thin boundary layers, high heat transfer rates, and low turbine efficiency. It has been recognized that the blade tip geometry and subsequent tip leakage flows have a significant effect on the aerodynamic efficiency of turbines. Hence, state-of-the-art cooling techniques must be developed and utilized on the blade tip to avoid blade failure due to the heavy thermal loads. Presence of film cooling on the tip further reduces heat transfer from the mainstream gas to the blade tip. A comprehensive compilation of the available cooling techniques used in the Gas Turbine industry has been encapsulated by Han et al. [26] in their book.

Film cooling is an external cooling technique commonly used in conjunction with internal cooling to protect the turbine components from the mainstream hot gas. In film cooling, a portion of the coolant used for internal cooling is ejected through slots or discrete holes over the surface of the components that need thermal protection. The coolant thus ejected displaces the mainstream boundary layer creating a protective film on the surface of the exposed component. This isolates the hot mainstream gas from the

metal surface and considerably decreases the magnitude of the temperatures the hot gas path components encounter.

Understanding the complex mechanism of heat transfer on the turbine blade tips is a prerequisite for effectively designing the blade tip cooling systems. Metzger et al. [31] used a narrow slot-type channel with one of the bounding walls containing a transverse rectangular cavity to model the grooved turbine blade tips. A general reduction of overall heat transfer on the cavity floor was observed as the cavity depth was increased.

Recently, more researchers have shown interest in the film cooling on turbine blade tips. Kim and Metzger [32] developed an experimental approach to model and measure the heat transfer on turbine blade tips with film cooling. Kim et al. [33] continued the experimental work presented in [32] to study the effects of film cooling on the turbine blade tip heat transfer. The results indicated that the blade tip geometry and injection locations significantly affect the film cooling performance. Bunker [34] provided a comprehensive review and summary of the blade tip heat transfer based on the early public fundamental studies. Azad et al. [35, 36] experimentally investigated the heat transfer coefficient and static pressure distributions on gas turbine blades with plane and squealer tips installed in a five-bladed linear cascade. All measurements were conducted with tip gap clearances of 1%, 1.5% and 2.5% of the blade span. The results showed that a larger tip gap leads to a stronger heat transfer process. Bunker and Ameri et al. [37, 38] performed comprehensive experimental and numerical studies to

investigate the heat transfer on the first-stage blade tip for a large power generation turbine. The detailed distribution of heat transfer coefficients was reported for different tip geometries at various inlet turbulence intensity levels.

Kwak and Han [39] measured the heat transfer coefficients and film effectiveness on a gas turbine blade plane tip with film cooling holes along the camber line and near the tip region of the pressure-side. They found that both the heat transfer coefficient and film effectiveness increased as the tip clearance increased. Meanwhile, increasing the blowing ratio would increase the film cooling effectiveness but decrease the heat transfer coefficient. Kwak and Han [40] also performed similar measurements on the squealer tip with a 4.22% recess of a gas turbine blade. Adiabatic effectiveness for turbine blades with cooling holes placed along the pressure side tip as well as dirt purge holes placed on the tip was measured by Christophel et al. [41]. Gao et al. [42] experimentally studied the effect of inlet flow angle on film cooling effectiveness for a cutback squealer blade tip under average blowing ratios of 0.5, 1.0, 1.5 and 2.0. The coolant jet direction and hence the cooling effectiveness was altered when the incidence angle was changed. However, the flow angles had no significant effect on the area-averaged film cooling effectiveness. Park et al. [43] measured the heat transfer coefficients and film cooling effectiveness on the tip and inner rim walls of a rotor blade with a squealer rim equipped in a three-blade linear cascade. The high heat transfer and film cooling effectiveness regions were obtained near the film-cooling holes.

Due to the difficulty of acquiring data on a rotating blade, literature studying the effect of rotation is very scarce. Dring et al. [44] reported film cooling effectiveness in a rotating configuration in a low speed tunnel. Takeishi et al. [45] also studied film cooling effectiveness on a stator-rotor stage, simulating a heavy duty gas turbine. Measured effectiveness values on the suction side for the rotating turbine blade seemed to match the data from the stationary cascade whereas the rotating effectiveness on the pressure side seemed to be significantly lower than the nonrotating case. Effects of rotation are attributed to the deflection of the film cooling jet due to centrifugal forces. Abhari and Epstein [46] reported film cooling heat transfer coefficients by the superposition method on the short-duration MIT blowdown turbine facility using heat flux gauges. Time resolved heat transfer coefficient data was obtained and the benefit of using film cooling on the blade surface is evident.

Acharya et al. [47] performed a numerical study to investigate the blade tip heat transfer and flows with both pressure side and tip coolant in the presence of relative motion between the blade and casing. It was confirmed that the relative motion between the tip and shroud had significant effects and thus the statement of pressure-driven leakage flows was not appropriate. Yang et al. [48] numerically simulated the effect of the blade rotation on the flow and heat transfer for turbine blades with plane and squealer tips. The prediction indicated that the rotation effect on the flow behaviors and heat transfer primarily came from the relative motion of the shroud, especially for the squealer tip. Lu et al. [49] numerically investigated the aerodynamics and film cooling

effectiveness of high pressure turbine blade tips. Two different rotor blade tip configurations have been studied: the plane tip and the squealer tip with tip hole cooling. Molter et al. [50] measured and predicted the heat transfer for blades with a flat tip and a squealer tip without cooling. It shows CFD is not capable of estimating unsteady heat load component and generally over predicts the overall heat flux.

Rotating turbine experiments performed by Ahn et al. [51, 52] showed that the turbine rotational speed is the most critical parameter in film cooling effectiveness distributions. The measurements were done using the pressure sensitive paints (PSP). Furthermore, their systematic experimental results show that during an off-design operation, the incidence angle changes, causing the coolant film direction to change.

2. RESEARCH OBJECTIVES

Very limited experimental data is available for aerodynamic and film cooling effectiveness under rotating condition in the literature. As a result, there is a strong need to study in detail and discover essential features of turbine platform and blade tip film cooling under engine representative flow and rotating conditions. The objective of the research was to provide the gas turbine engine designer with a set of quantitative aerodynamics and film cooling effectiveness data which are essential for understanding the basic physics of the complex secondary flow, its influence on the efficiency and performance of gas turbines, and the impact of film cooling ejection arrangements on suppressing the detrimental effect of secondary flows.

With a better understanding of the flow physics and film cooling distributions on the rotating blade tip and platform, designers may be able to reduce the amount of air extracted from the compressor for the purpose of turbine blade and platform cooling. This improvement would allow for increase in turbine inlet temperatures and furthermore enhancing the system thermal performance. In order to meet the above stated objectives, the following aerodynamics, and film cooling effectiveness experiments were performed:

2.1. Contoured Endwall Aerodynamics Performance

The present study focused on the impact of new endwall contouring design based on continuous diffusion on the turbine aerodynamic performance. The following cases were studied on the contoured rotor platform:

- Performance measurements were performed varying the mass flow with and without purge flow (MFR=0%, 0.5%, 1%, 1.5%, 2%).
- Performance measurements were performed varying the rotational speed at different purge flow (MFR=0%, 0.5%, 1%, 1.5%, 2%).
- Circumferential and radial interstage aerodynamic measurements were performed at stations 3, 4 and 5 at rotor speeds of 2400rpm, 2550 rpm and 3000 rpm.
- Temperature measurement using the thermocouples on the stator leading edge.

2.2. Endwall Film Cooling Effectiveness Measurement

The present study focused on the impact of the rotating purge flow on the film cooling effectiveness of the first stage rotor platform with non-axisymmetric endwall contouring. The following cases were studied on the contoured rotor platform and were compared with non-contoured platform:

- MFR = 0.5% (blowing ratio, M=0.372), 1.0% (blowing ratio, M=0.744), and 1.50% (blowing ratio, M=1.116).
- Rotational speeds = 2400rpm, 2550rpm and 3000rpm.

2.3. Turbine Blade Tip Film Cooling Effectiveness

The present study experimentally investigated the film cooling effectiveness on four different turbine blade configurations within a rotating HP turbine. Four different configurations are: (1) Plane tip with radial ejection holes, (2) Blade with Ejection Holes and Squealer, (3) plane tip with pressure-side-edge compound angle hole cooling, and (4) squealer tip with pressure-side-edge compound angle hole cooling. Eight 45˚

compound angle holes are used for pressure-side-edge cooling. Detailed blade tip film cooling effectiveness distributions on the rotating blade tip was measured using the PSP technique. The coolant is ejected through the cooling holes under blowing ratios. The following cases were studied for each blade tip configuration:

- Three blowing ratio of M=0.75, 1.25 and 1.75.
- Three rotational speeds of 2000 rpm, 2550 rpm and 3000 rpm.

3. EXPERIMENTAL FACILITY*

The research turbine facility used for the current experiments was designed by Schobeiri [53] to address aerodynamic performance and heat transfer issues of high pressure (HP), intermediate pressure (IP), and low pressure (LP) turbine components. Detailed aerodynamic, efficiency, loss and performance measurements were carried out to verify and document the efficiency and performance of several high efficiency turbine blades designed for major original turbine manufacturers. To compare the results of the investigations reported in [53] with those for 2-D cylindrical blades, aerodynamic measurements were conducted and summarized in the subsequent reports [54] and [9].

The overall layout of the test facility is shown in Figure 4. It consists of a 300HP (223.71 kW) electric motor connected to a frequency controller which drives a three-stage centrifugal compressor capable of supplying air with a maximum pressure difference of 55kPa and a volumetric flow rate of $4\frac{m^3}{s}$. The compressor operates in suction mode and its pressure and volume flow rate can be varied by the frequency controller operating between 0 to 66Hz. A pipe with a smooth transition piece connects the compressor to a Venturi mass flow meter used to measure the mass flow through the

* Part of the materials are reprinted with permission from "A Combined Experimental and Numerical Study of the Turbine Blade Tip Film Cooling Effectiveness under Rotation Condition" by Mohsen Rezasoltani, Kun Lu, Meinhard T. Schobeiri and Je-Chin Han, 2015. J. Turbomach, 137(5), Copyright © 2015 by ASME, and "Experimental Investigation of the Effect of Purge Flow on Film Cooling Effectiveness on a Rotating Turbine With Non-Axisymmetric Endwall Contouring," by M. Rezasoltani, M. T. Schobeiri and J. C. Han, J. Turbomach. 2014; 136(9), GT2013-94807, Copyright © 2014 by ASME.

Table 1: Turbine dimensions and operating conditions

Stage no., N	3	Mass flow	3.58 kg/s
Tip Diameter	685.8mm	Hub Diameter	558.8mm
Reference speed	3000 rpm	Current speed range	1800 to 3000 rpm
α_2	19^o	β_3	161^o
C_x	41.6 mm	Pressure ratio	1.41
Re	231400	Mach number	0.27

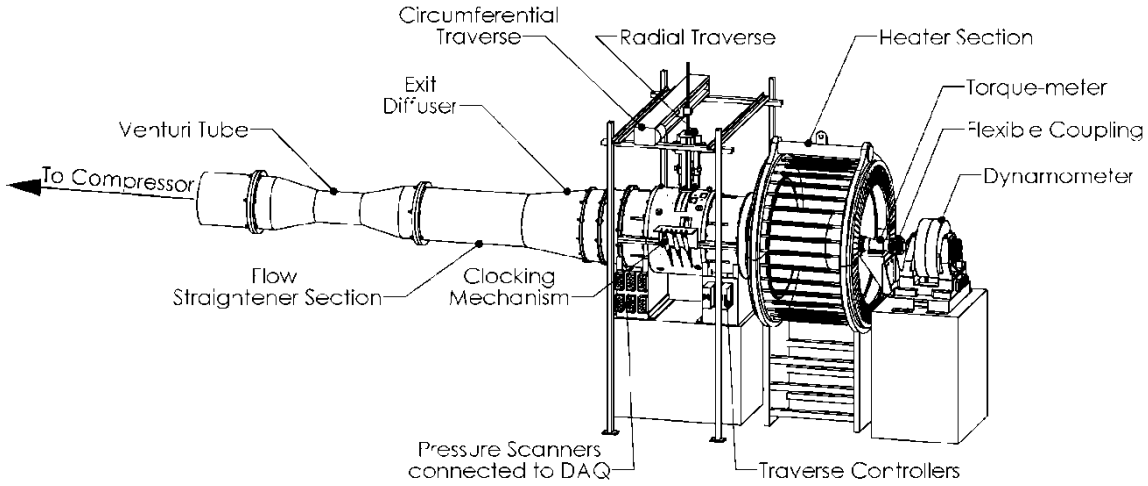

Figure 4: The overall layout of TPFL-research turbine facility

turbine component. The three-stage turbine has an automated data acquisition system for detailed flow measurement at each blade row location in the radial and circumferential direction. The turbine inlet has an integrated heater that prevents condensation of water from humid air during experiments.

3.1. Interstage Instrumentation

Figure 5 shows three stages research turbine with their components. Detailed operating condition with turbine dimensions is presented in Table 1. The three-stage air

turbine component has a casing that incorporates stator rings in order to achieve greater versatility. Three traversing systems have five-hole probes with decoders and encoders for accurate probe position mounted upon them. A controller with feedback connected to each system is able to move the probes at a precision of 1/400 mm (2.5 μm). These three systems are mounted on a base plate, connected with the three T-rings installed in the casing. To seal the three 90° circumferential traversing slots, three T-rings are used. These T-rings prevent leakage of mainstream mass flow through the traversing slots by moving circumferentially. Altogether, this constitutes a traversing unit; it moves the unit in a circumferential direction and is connected to a fourth traversing system which is placed on top of a frame.

The traversing unit can move radially from 1 mm above the hub diameter to 1 mm from the blade tip. Each traverse (radial or circumferential) has individual stepper motors, allowing for accurate probe alignment during data acquisition.

Combined total temperature and total pressure rakes are utilized both upstream of the first stator row and downstream of the last rotor row for performance instrumentation. These rakes each combine 4 total pressure probes of the Pitot tube type, and 3 total temperature probes which are calibrated J-type thermocouples, placed equidistantly along the radial direction. Rakes were placed radially at the inlet at 45°, 135°, 225°, and 315°.

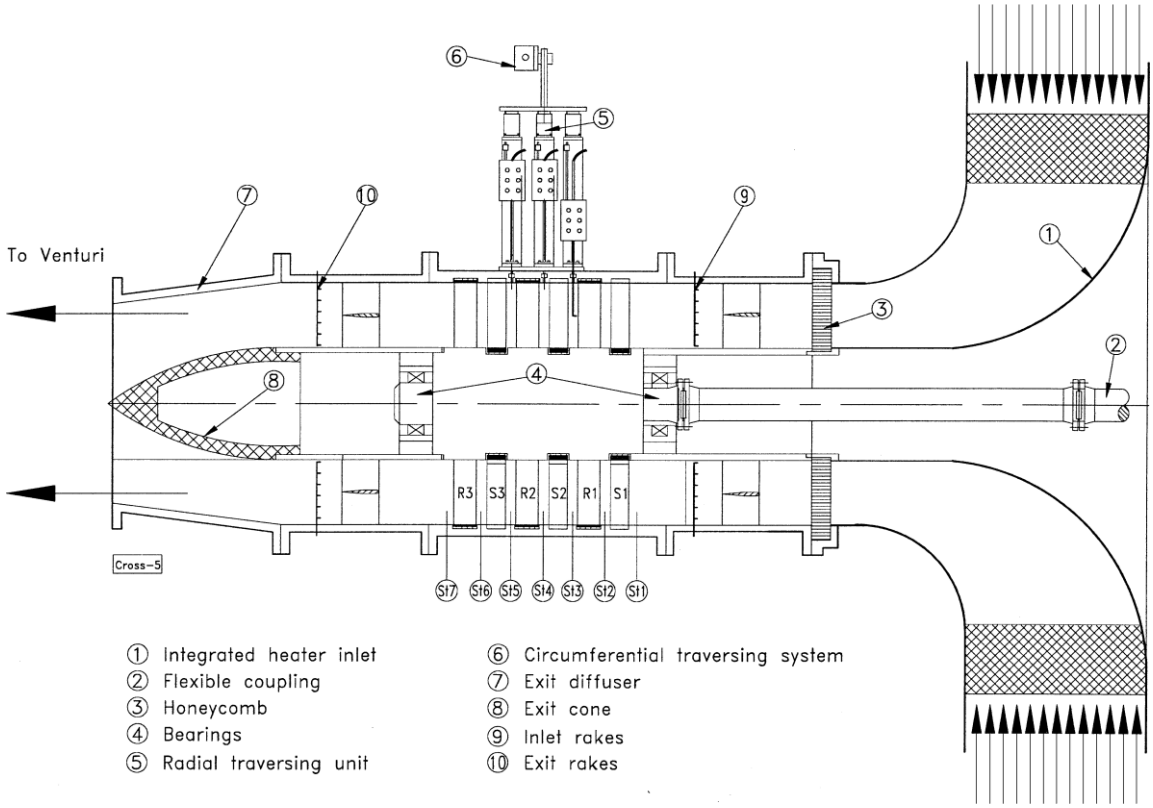

Figure 5: TPFL Turbine component and instrumentations [54]

Thermocouple calibration curves are introduced into the performance data reduction program. The rakes have a round leading edge and a sharp trailing edge; this aerodynamic shape reduces wake thickness originating from the trailing edge of the inlet rakes. Exit rakes have the same spacing as inlet rakes and are placed radially, and they are offset from the inlet rakes so that there is no interference with wakes from inlet rakes. Wall static pressure taps are placed on the T-rings and stator rings, as well as at the top and bottom halves of the main casing. Also, on two diametrically opposed stator blades of the second and third stator rows, total temperature and total pressure probes are placed on leading edge stagnation points. Total and static pressure contours, flow angles,

velocity components, flow angles as well as spanwise distribution of total pressure loss coefficients, and efficiency for each row are generated from the data derived from the transversing, using three L-shaped five-hole Pitot probes. Of these probes, the first and third are placed at stations 3 and 5, respectively, and calibrated at the low subsonic Mach number of M = 0.1. The second probe is installed at station 4 and takes into account any small compressibility effects in its calibration due to a moderate subsonic Mach number (M = 0.3). Figure 6 shows cross section view of three probes between stages.

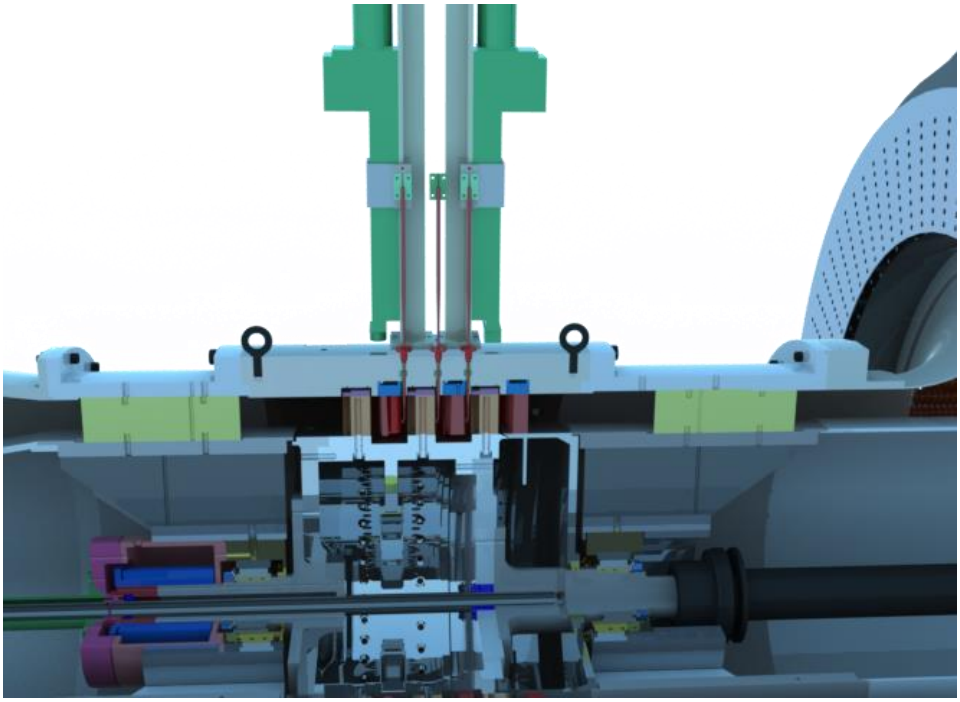

Figure 6: Turbine cross section view of interstage instrumentation

3.2. Five Hole Probe Calibration Facility

The accurate calibration of sensors is a prerequisite for measurement of any physical quantity. Concerning the fluid mechanics, these quantities are static and total

pressures and temperatures as well as the velocity vectors with their three components with the corresponding angles. Regardless of the nature of the data, understanding the experimental environment, eliminating parasitic effects and properly designing a calibration facility are the first steps towards acquiring accurate data. The facility described below is used for calibrating five-hole probes. The calibration facility is shown in Figure 7. This facility has been used to calibrate the hot wire and five-hole probes.

Compressed air is drawn from a reservoir which passes through a pressure regulator, filter and flow control valve before entering the calibration facility. It consists of a settling chamber followed by a pipe with three axisymmetric sections, each having a diameter of 152.9 mm. A nozzle with an exit diameter of 38.1 mm is attached to the end of the pipe. The inlet and outlet of the nozzle are parallel to the axis of the facility. The calibration nozzle is fed from a 120 psi pressure line, which creates a jet of air with stable, uniform and known properties.

Several thermocouples are placed in the first section of the calibration facility to measure the air temperature. Also, several pressure taps are placed in the last section of the pipe to measure the pressure difference between static pressure inside the pipe and the atmospheric pressure with a differential pressure transducer. Two micro lynx stepper motors with controllers are used to automatically vary the pitch and the yaw angles. The stepper motors are mounted on a traversing system with an arm at 90o. The system is designed to place the probe tip in the center of the exiting jet (Figure 8).

An automated calibration facility carries out independent calibration of the five-hole probes. In an angular indexing mechanism, each probe is pitched and yawed in 20 increments through angle ranges of -20.0 to 20.0 in pitch and yaw. An extremely fine angle resolution is achieved by the probe indexing mechanism using two computer-controlled stepper motors. TURBOPROBE, an in-house computer algorithm used by this facility, creates a grid of pitch and yaw angles that are specified by the user, and it controls these stepper motors. In addition, it records pressures from the PSI-9016 pressure scanner and stores in a data file pressures from the five-hole probe with corresponding pitch and yaw angles as well as calibration nozzle total pressure. Then, this data file is used for the creation of the calibration surfaces for probes that determine velocity components and vectors at turbine stations 3, 4, and 5. This is explained in the section devoted to experimental procedure.

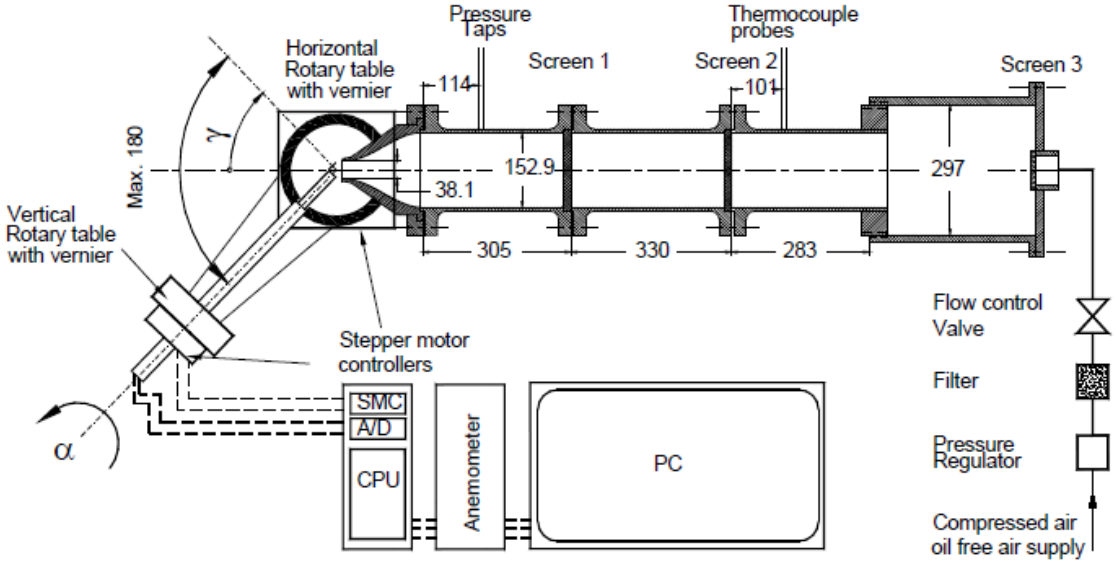

Figure 7: Facility for calibrating five-hole probes and hot-wire [2]

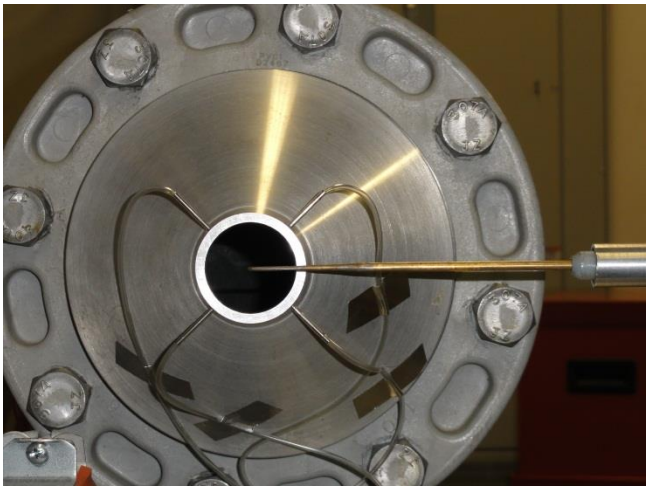

Figure 8: Place the probe tip in the center of the exiting jet

3.3. New Turbine Component Design

To study the effect of new endwall contouring method and blade tip cooling under rotating condition, new ring and 4 pairs of blade tip configuration were designed and added to the research turbine facility.

3.3.1. New Ring with Endwall Contouring

For the current investigation, the contouring method described in [8] was applied to the first rotor row and second rotor row. Extensive numerical simulations were performed to obtain an optimum geometry for contouring the rotor endwall. As it is shown in Figure 9 and Figure 10 the first rotor row is immediately exposed to the circumferential gap, so there is no axial space to extend the contouring upstream of the blades to achieve the same efficiency that we achieved for the second rotor row ([8], [55]). This configuration resulted in lower turbine efficiency as discussed earlier.

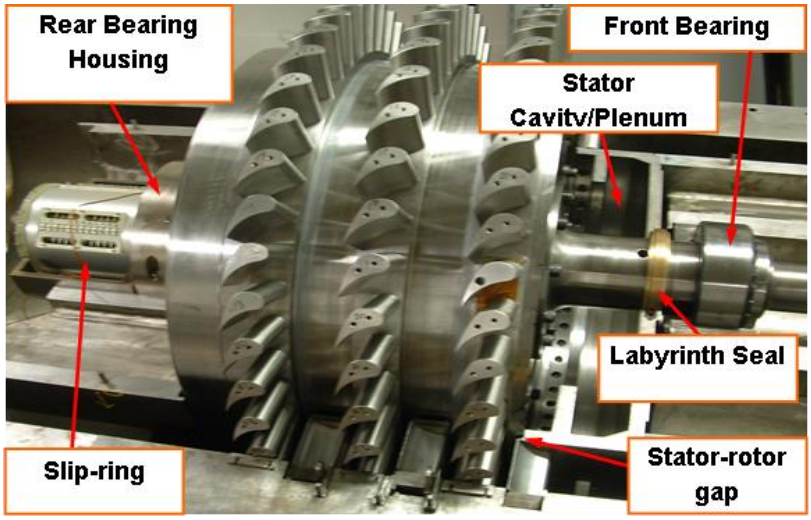

Figure 9: Turbine components with showing stator cavity and gap

Considering the geometry of turbine, efforts have been made to improve the efficiency by varying the endwall contouring of the first rotor row as shown in Figure 11. This Figure shows the variation of the contour depth along the suction surface. A strong deceleration rate characterized by a steep gradient of the contouring height, pertaining to R1, R1-1, R1-2 and R1-3-curves, caused flow separation within the contouring. This resulted in an efficiency that was just slightly above the reference case without contouring. It turned out that the contouring R1-4 that was originally generated by the continuous diffusion method yielded the best efficiency improvement [55].

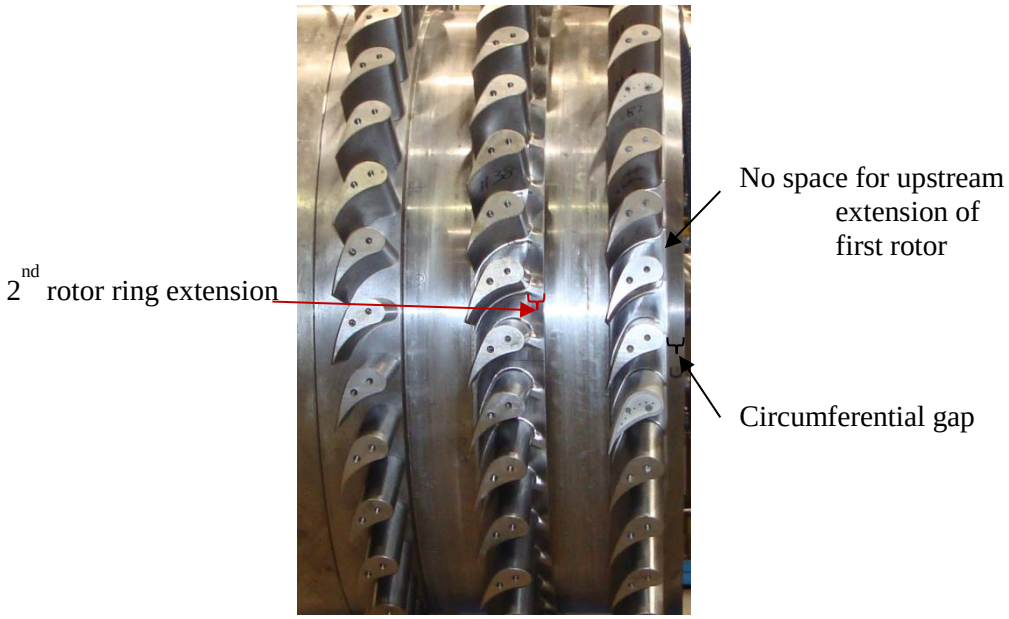

Figure 10: Position of the circumferential gap for ejection of purge flow and extension of the contouring upstream of second rotor

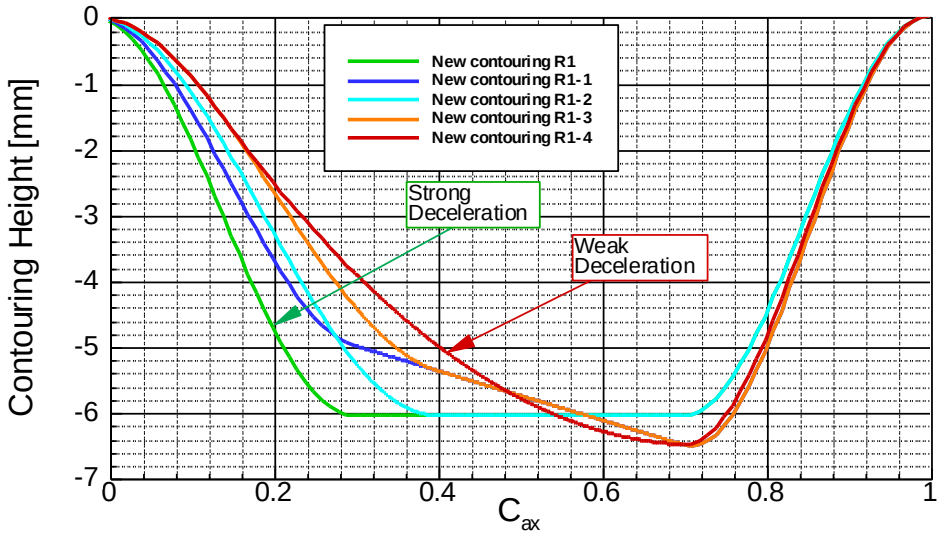

Figure 11: Variation of contour depth along the suction surface to obtain the best endwall contouring efficiency [55]

For each of the calculated cases, the entire flow field including total pressure loss and the turbine efficiency were obtained. Considering the spatial restrictions mentioned

above, particular attention was paid to accurately obtain the efficiency of the turbine with the first and second rotor endwall contoured. Based on this variation, results showed that Contouring R1-4 had the highest efficiency and was used for every endwall between the blades. Figure 12 shows the construction of the new endwall contours compared to the reference case. The reduction of the total pressure loss by 27.9% and accordingly enhance of the second rotor efficiency by 0.51% was obtained based on the CFD predictions.

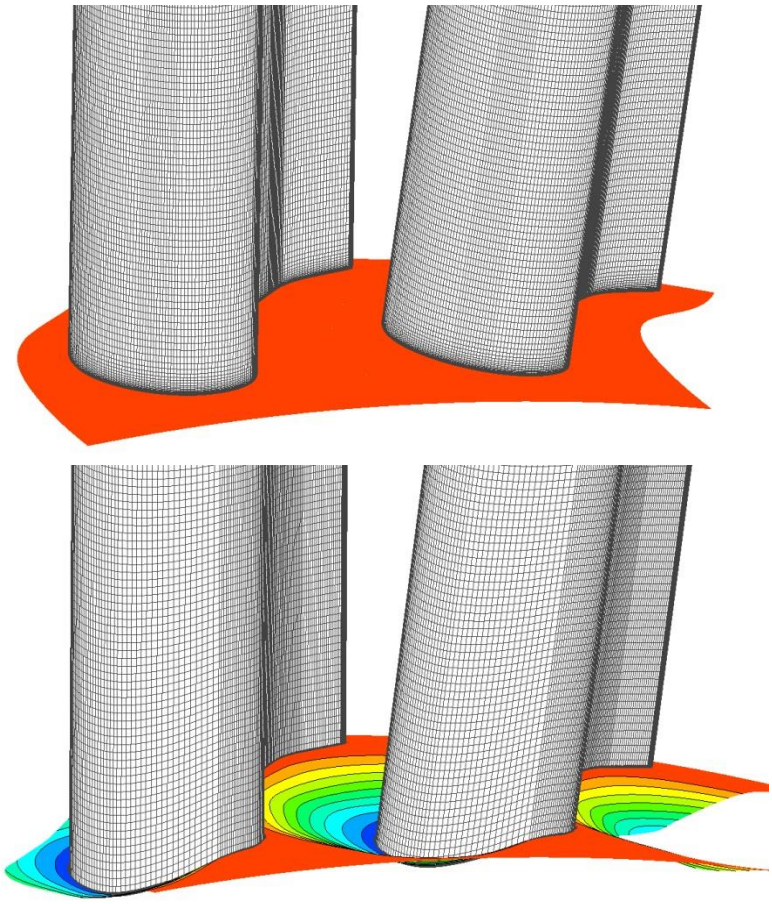

Figure 12: Non-contoured (top), new contouring method (bottom) [8, 55]

3.3.2. Blade Tip Geometry

To investigate the film cooling effectiveness on rotating blade tips within the three stage HP turbine, TPFL designed and manufactured four pairs of rotor blades with four different film cooling arrangements: plane tip with tip hole cooling (red), plane tip with pressure-side-edge compound angle hole cooling (green), squealer tip with tip hole cooling (yellow), and squealer tip with pressure-side-edge compound angle hole cooling (blue), as shown in Figure 13. Note that the blade consists of top and bottom pieces due to the manufacturing constraints.

In order to prevent any imbalance, the four pairs of rotor blades with film cooling holes were axis-symmetrically mounted at the first rotor row (Figure 13 top). The detailed geometry for each blade tip with cooling configuration is shown in Figure 14. Note that the blade height, axial chord length, and film cooling hole diameter (d) are 62.865 mm, 38.1 mm, and 1.27 mm, respectively. Seven perpendicular cylindrical holes evenly distributed along the camber line are used for the tip hole cooling, whereas eight 45° compound angle holes for pressure-side-edge cooling are located 4.564 mm below the blade tip edge. For the tips with tip hole cooling, the length of each cooling hole has a typical value of 4 d, which is 5.08 mm. Moreover, the squealer tip has a rim width of 2 mm and a recess of 4 mm. Due to the squealer cavity, the blade with squealer tip has a bit smaller plenum inside the body than that of the blade with plane tip. However, both plena have adequately enough space to form highly uniform pressure inside resulted

from the sudden expansion and fully mixing of coolant flow ejecting from the tiny holes on the bolt. In addition, each blade obtains a tip clearance as wide as 1% of blade span.

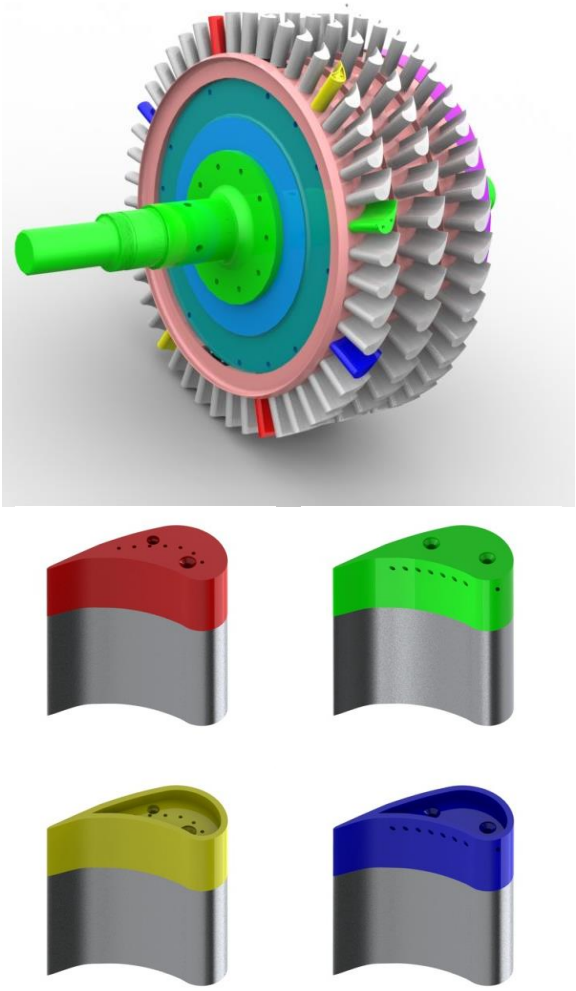

Figure 13: Four different rotor blade tip configurations: Plain tip with tip hole cooling (red), Plain tip with pressure-side-edge compound angle hole cooling (green), squealer tip with tip hole cooling (yellow) and squealer tip with pressure-side-edge compound angle hole cooling (blue) [49]

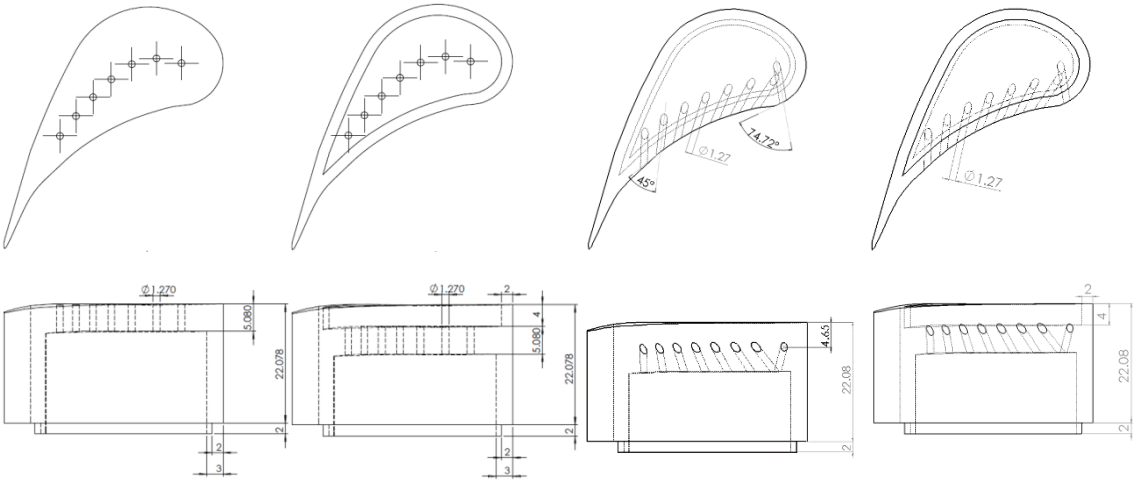

a) b) c) d)

Figure 14: Detailed geometry of blade tips: (a) plane tip with tip hole cooling; (b) squealer tip with tip hole cooling; (c) plane tip with pressure-side-edge compound angle hole cooling; (d) squealer tip with pressure-side-edge compound angle hole cooling [56]

3.3.3. Cooling Loops

To determine the film cooling effectiveness under rotating conditions for different kinds of film cooling (Ahn et al. [51, 52] and Suryanarayanan et al. [27, 28]), the existing turbine rotor described in [53] was modified to integrate the coolant loop through the downstream section of the hollow turbine shaft and into the cylindrical hub cavity. Two independently controlled, concentric coolant loops provide the necessary mass flow for film cooling experiments. The outer loop supplies coolant for film cooling experiments in the tip of the blade. The inner loop coolant jet ejecting from a circumferential gap between the 1st stator and rotor provides for hub platform cooling (Figure 15).

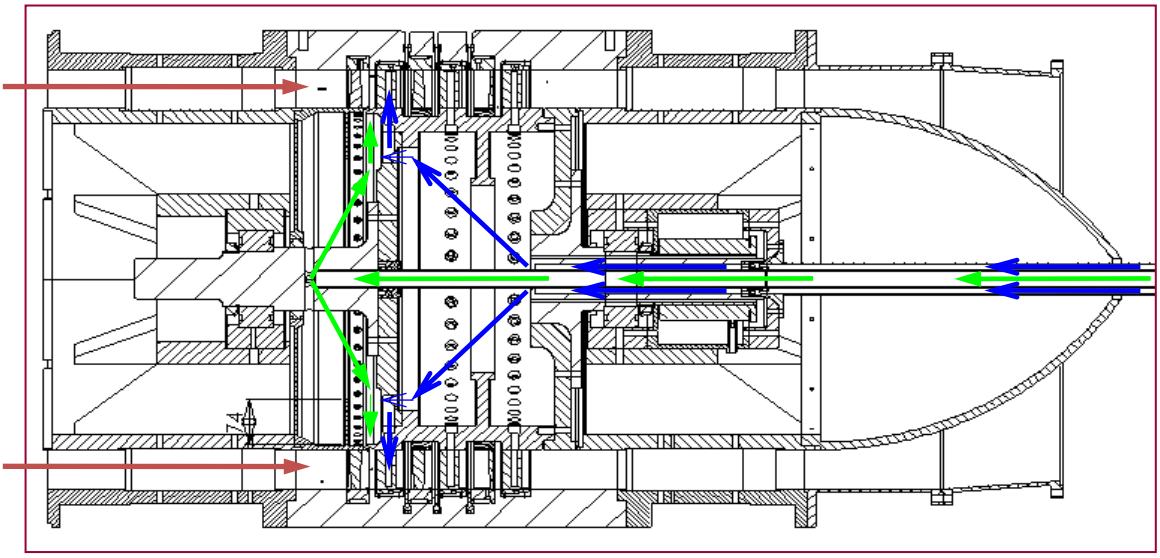

Figure 15: Section view of the modified stator-rotor turbine assembly for stator-rotor purge flow and platform film cooling [49, 57]

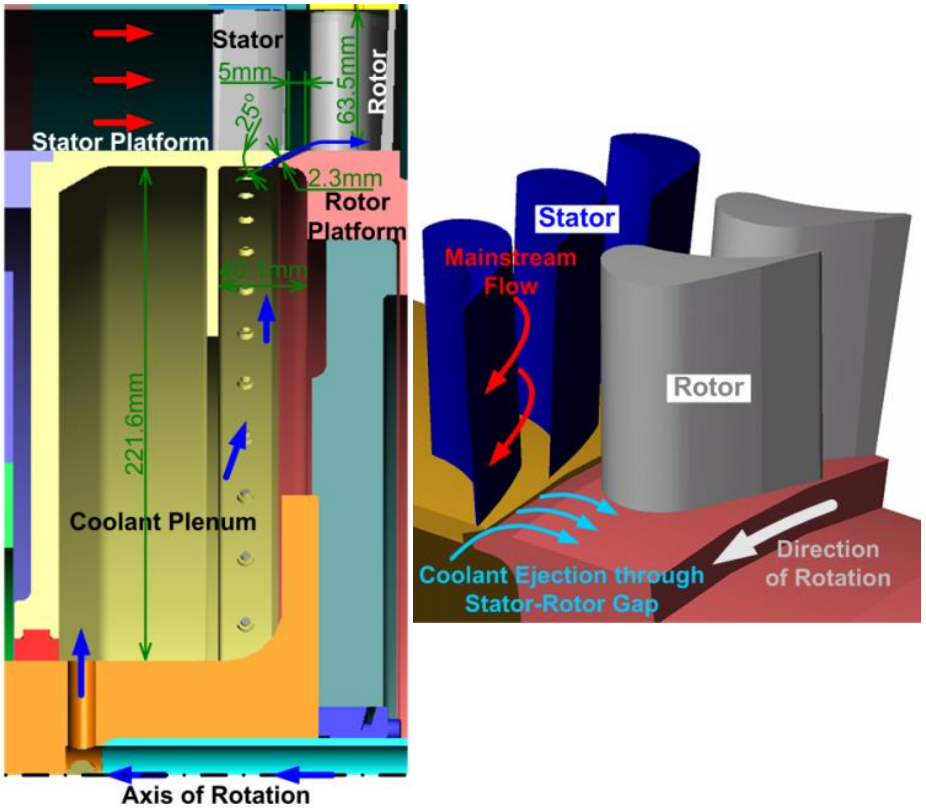

Figure 16: Detailed view of the stator-rotor gap design [27]

As mentioned above (Figure 16), the outer loop (marked by blue arrows) delivers coolant mass for film cooling experiments for the discrete film cooling holes on both blade tips in the first-stage rotor. The coolant flow is discharged through a long annular pipe and fills inside of the rotor internal cavity. A rotary seal was adapted to prevent any leakage. The coolant inside the rotor cavity is delivered to the blades and injected through the discrete film cooling holes on the blade tips.

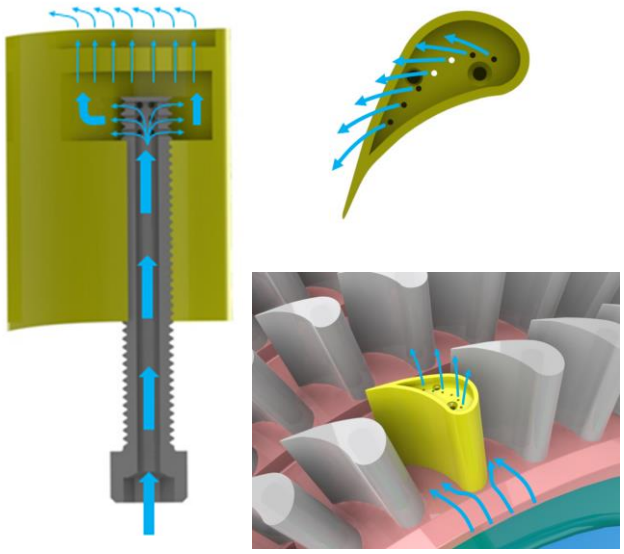

Figure 17: Schematic of the blade tip film cooling system [49]

Figure 17 shows the coolant path inside the blade. As seen, after passing through a cylindrical hole drilled at the center of the bolt that fastens the rotor blade, the coolant mass is ejected into a plenum through eighteen radially distributed tiny holes near the bolt tip. This relatively large plenum is applied to ensure a uniform coolant-discharge pressure distribution within the plenum for each film cooling holes. Eventually the coolant

flow is injected to the mainstream from seven discrete film cooling holes located either on the blade tip or at the pressure-side edge near tip region. Since the current study is focused on the rotor blade tip film cooling, only the outer loop is turned on. Based on these cooling configurations, TPFL HP turbine is capable to perform fundamental measurements of the blade tip film cooling under rotating condition.

3.3.3.1. Cooling Air Temperature Measurement

In order to measure the coolant temperature, eight thermocouples were placed in the cavity inside each cooling blade (Figure 17). Since rotor is rotating those thermocouples were connected to the slip ring (Figure 9) and then connected to the Fluke temperature measurement devices in the control room.

4. EXPERIMENTAL PROCEDURE*

4.1. Aerodynamic Measurement Theory and Analysis

Interstage aerodynamic measurements are performed along the first stage rotor exit, second stage stator exit and third stage rotor exit using miniature 5-hole probes. The circumferential and radial traverse facility enables comprehensive data acquisition at these locations. To reduce the error in measurements near the blade tip and hub where the flow is highly complex, additional stepper motor controls are provided to allow for accurate adjustment of the miniature 5-hole probes in line with the mainstream flow.

Five hole probes are calibrated in order to be able to correlate the measured pressures with flow velocity and direction. The calibration is highly dependent on flow velocity. As mentioned earlier, the probes are calibrated at Mach numbers of 0.1 and 0.3 in a calibration facility using a non-nulling technique. As shown in Figure 18, there are two methods of using five-hole probes for measuring static and total pressures as well as velocity components.

In nulling method the probe tip axis is adjusted to the flow angle such that the pressures of holes left-right and top-bottom are equalized. This requires changing

* Part of the materials are reprinted with permission from "A Combined Experimental and Numerical Study of the Turbine Blade Tip Film Cooling Effectiveness under Rotation Condition" by Mohsen Rezasoltani, Kun Lu, Meinhard T. Schobeiri and Je-Chin Han, 2015. J. Turbomach, 137(5), Copyright © 2015 by ASME, and "Experimental Investigation of the Effect of Purge Flow on Film Cooling Effectiveness on a Rotating Turbine With Non-Axisymmetric Endwall Contouring," by M. Rezasoltani, M. T. Schobeiri and J. C. Han, J. Turbomach. 2014; 136(9), GT2013-94807, Copyright © 2014 by ASME.

angular position of the probe. As a result, this method, requires a complex probe traversing mechanism for the rotation of the probe, which often causes difficulty to install the measurement unit into the given flow field. Therefore, measuring the flow field in this method is extremely time consuming and in most cases impractical.

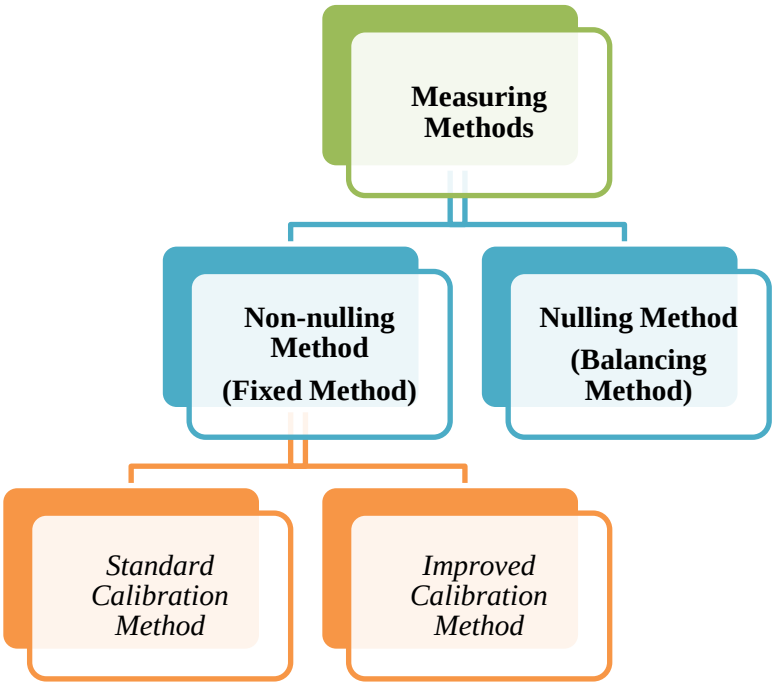

Figure 18: Measuring methods with five-hole probe

On the other hand, in a non-nulling method, the probe orientation remains fixed as long as the flow variation occurs within the calibration range. In case that the actual flow angle exceeds the calibration range, a partial adjustment of β-angle (also called yaw) is possible as long as the variation of α-angle (also called pitch) occurs within the calibration range. The non-nulling method requires the probe to be calibrated to account for flow pressure and direction variations before being placed in the flow-field at a fixed

position. This allows for performing extensive multi-point flow measurements where the probe is typically radially or axially traversed across the flow domain without the need to continuously adjust the probe body or tip angles. In Figure 19 example of traversing system inside a research turbine is shown.

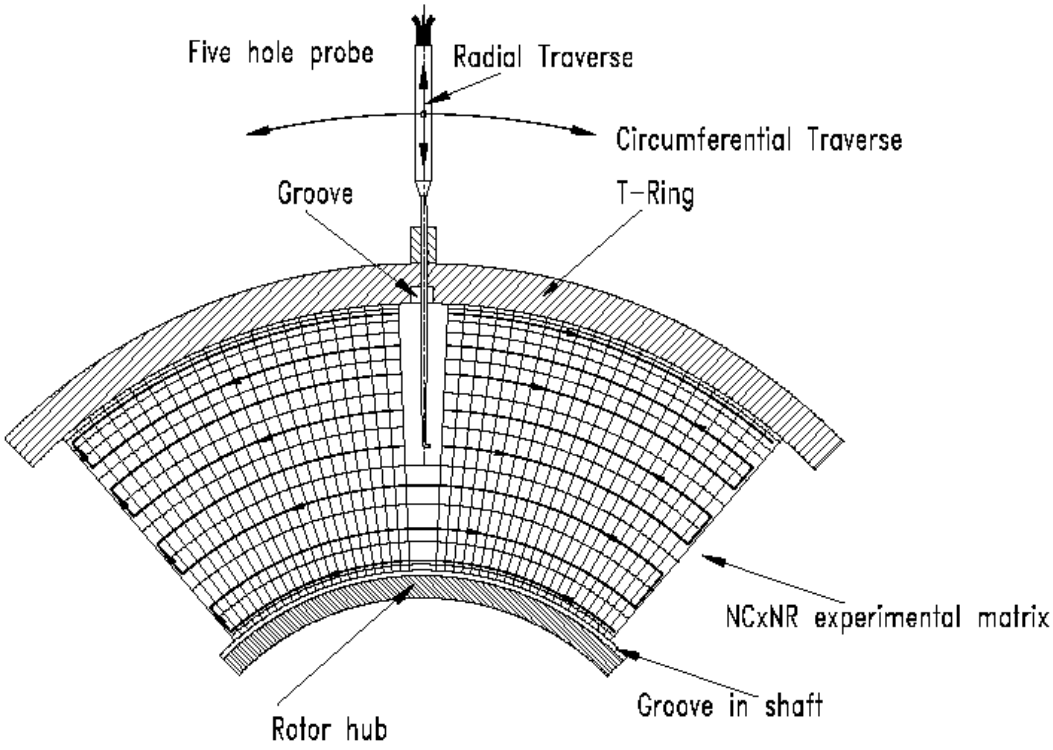

Figure 19: Example of traversing system for non-nulling method in a research turbine [2]

The measured data are represented as dimensionless pressure coefficients. A data reduction technique is then employed to correlate known flow field with the pressure coefficients. Various calibration algorithms for five-hole probes are proposed. These algorithms differ in the manner in which the pressure coefficients are defined and the

data reduction technique employed. Numerous non-nulling calibration methodologies have been developed over the last three decades. Differential pressure readings were reduced to non-dimensional numbers that are then compared to calibration maps. Dudzinsky and Krause [58] used graphical methods to obtain the angles and pressures from those calibration maps. Schobeiri and his co-workers [59] explained the calibration and data processing procedure using four non-dimensional parameters. Reichert and Wendt [60] performed a two-dimensional Taylor series decomposition of the calibration map. A recent paper by Town and Camci [61] discusses the calibration issues of existing methods.

The common feature of almost all existing calibration methods is the structure of calibration coefficients which include an algebraic average of the static pressures measured in the outer four holes. Implementing this average in calibration coefficient is admissible as long as the flow angle does not cause flow separation. For adverse flow angles, one or more outer holes measure pressure in a separated flow zone resulting in an erroneous average. To circumvent this deficiency, Rubner and Bohn [62] introduced a new calibration procedure which is deemed to be one of the most accurate and reliable procedures. In Figure 20 standard calibration method and improved one based on Bohn's technique is described. This Figure shows the process of how to find three dimensional velocity vectors by five-hole probe. After measuring pressure of five holes Pitch angle, yaw angle, static and total pressure are calculating by functions that calibration gives. These coefficients are

$$Q_1 = \frac{P_4 - P_5}{P_1 - P_s}, \quad Q_2 = \frac{P_3 - P_2}{P_1 - P_s}, \quad Q_3 = \frac{P_1 - P_s}{P_t - P_s}, \quad Q_4 = \frac{P_1 - P_4}{P_t - P_s}, \quad Q_5 = \frac{P_1 - P_5}{P_t - P_s} \qquad (1)$$

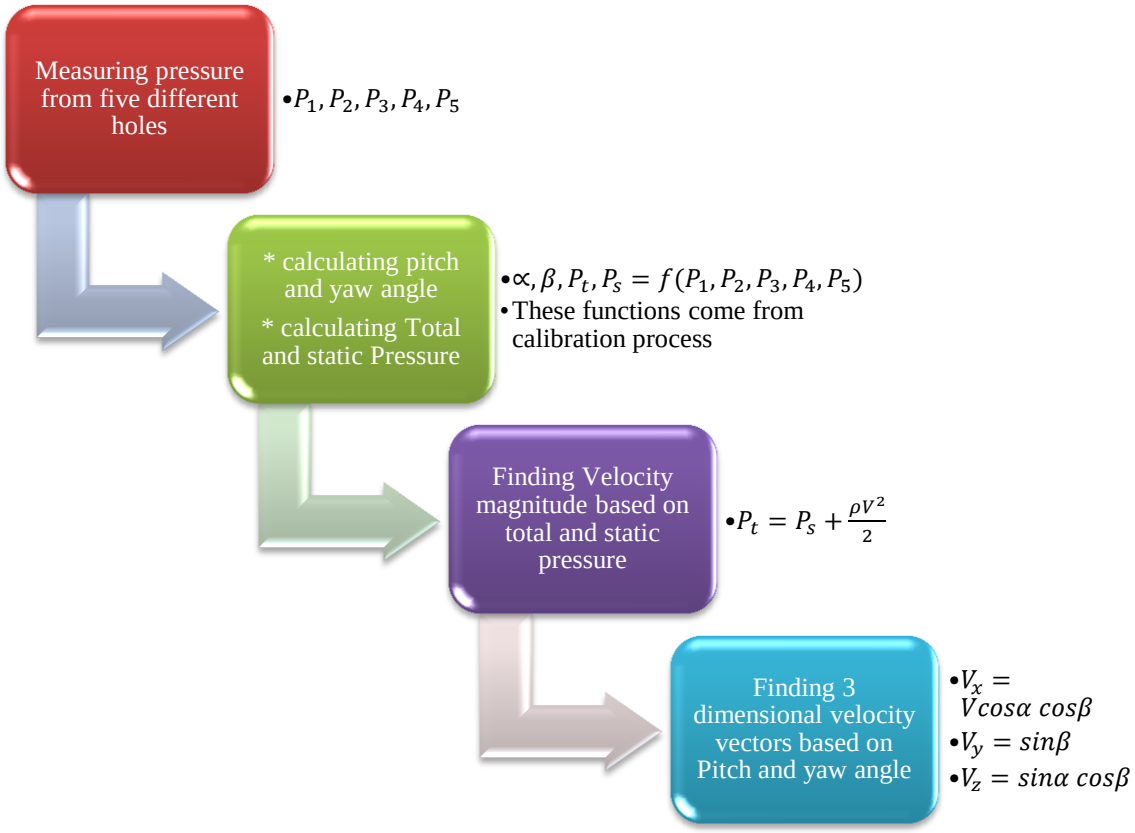

Figure 20: Process of finding 3 components of velocity vector

Using curve fit tools, three dimensional curves are computed that correlate the coefficients with the flow angles. These correlations are

$$\alpha = f_1(Q_1, Q_2)$$
$$\beta = f_2(Q_1, Q_2)$$
$$Q_3 = f_3(\alpha, \beta) \qquad (2)$$
$$Q_4 = f_4(\alpha, \beta)$$
$$Q_5 = f_5(\alpha, \beta)$$

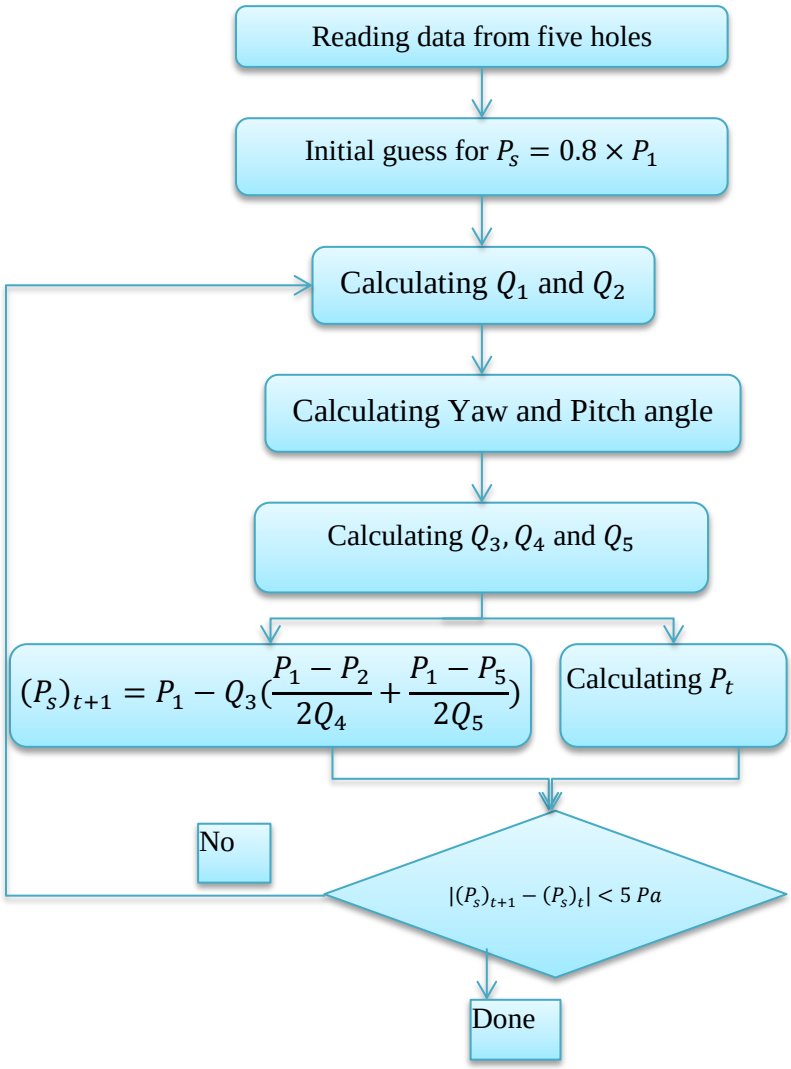

Figure 21: Process of calculating the flow angles and static and total pressure in improved calibration method

In Figure 21 iterative process of finding flow angles and static and total pressure is shown. Starting with Q_1 and Q_2, the static pressure P_s is obtained using an iterative process by setting $P_s = 0.8 \times P_1$. This step determines Q_1 and Q_2 and, thus $\alpha = f\left(Q_1, Q_2\right)$ and $\beta = f\left(Q_1, Q_2\right)$. With the calculated α and β, the remaining coefficients Q_3, Q_4, and Q_5 are calculated.

The iteration function given in [62] is:

$$\left(P_s\right)_{t+1} = P_1 - Q_3\left(\frac{P_1 - P_2}{2Q_4} + \frac{P_1 - P_5}{2Q_5}\right) \qquad (3)$$

which in conjunction with the following convergence criterion

$$\left|\left(P_s\right)_{t+1} - \left(P_s\right)_t\right| < 5pa \qquad (4)$$

After calculating the flow angles and static and total pressure, the three components of velocity can be calculated by correlation as is shown in Figure 22.

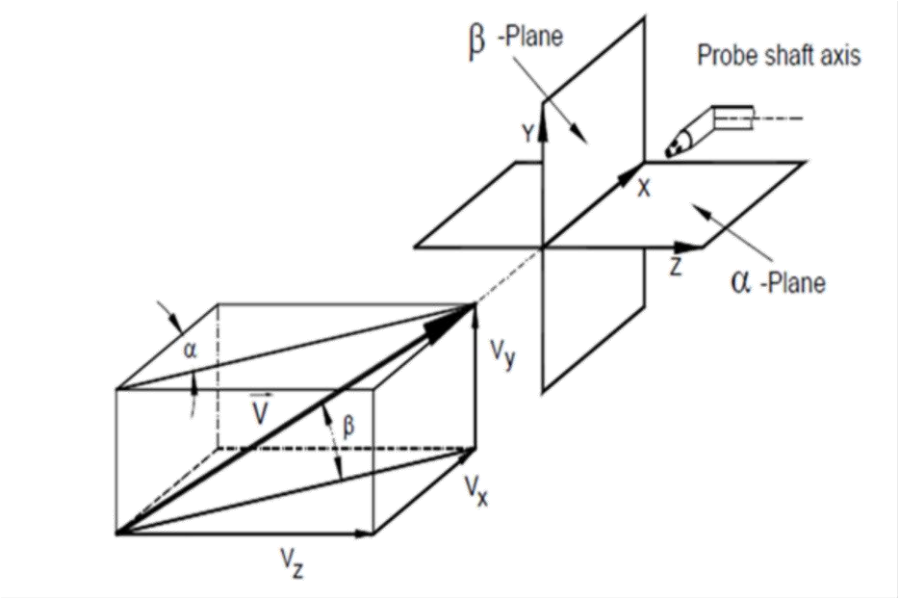

Figure 22: Three components of velocity vectors [2]

4.1.1. Five Hole Probe Calibration

Several calibrations were done to be sure about the quality of calibration curves. Bohn's method as described above was used to generate the calibration curves. Correlations mentioned in equation (2) are plotted and R^2 is shown for each plot.

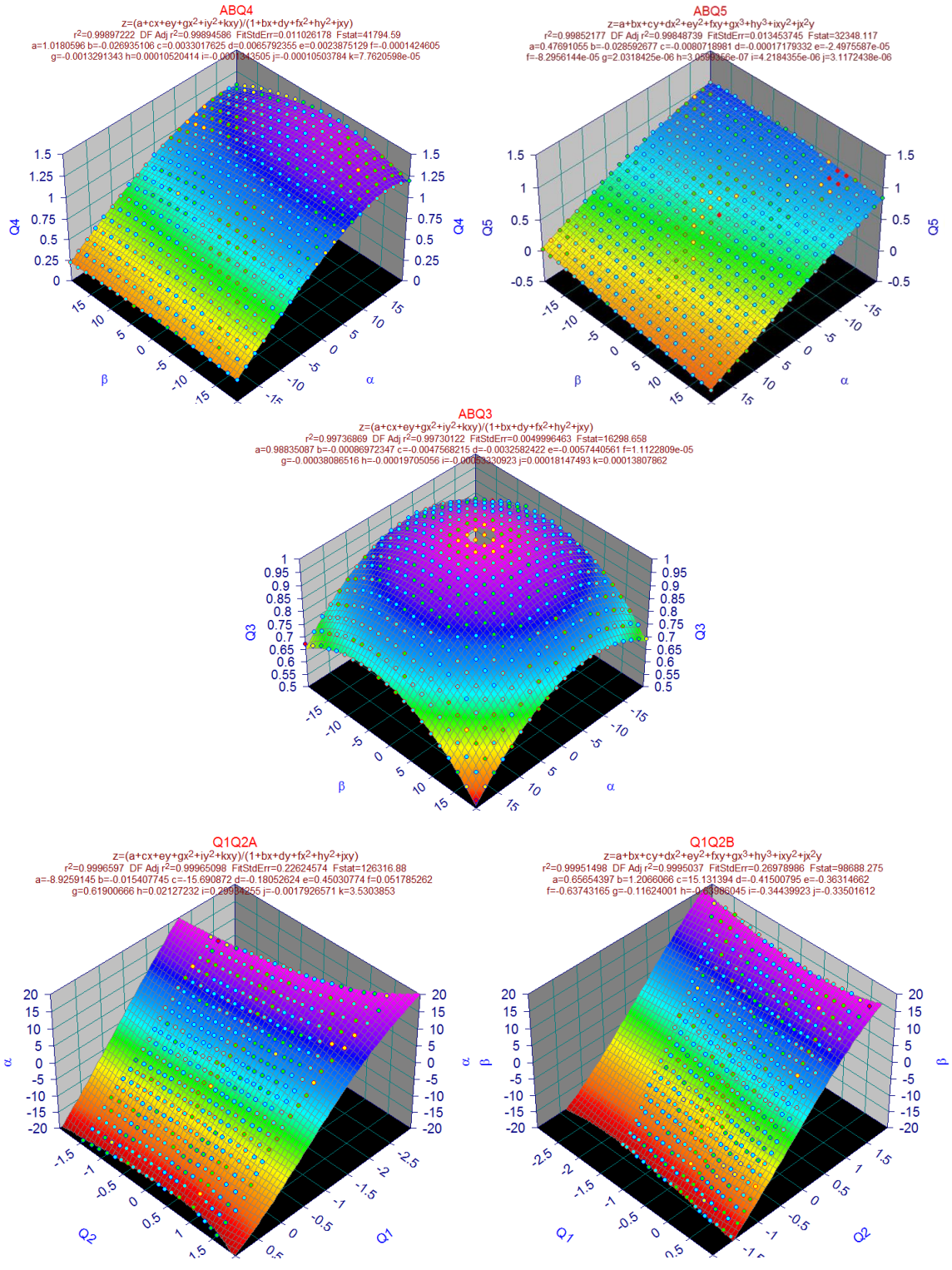

Figure 23: Calibration curves for probe installed at station 3

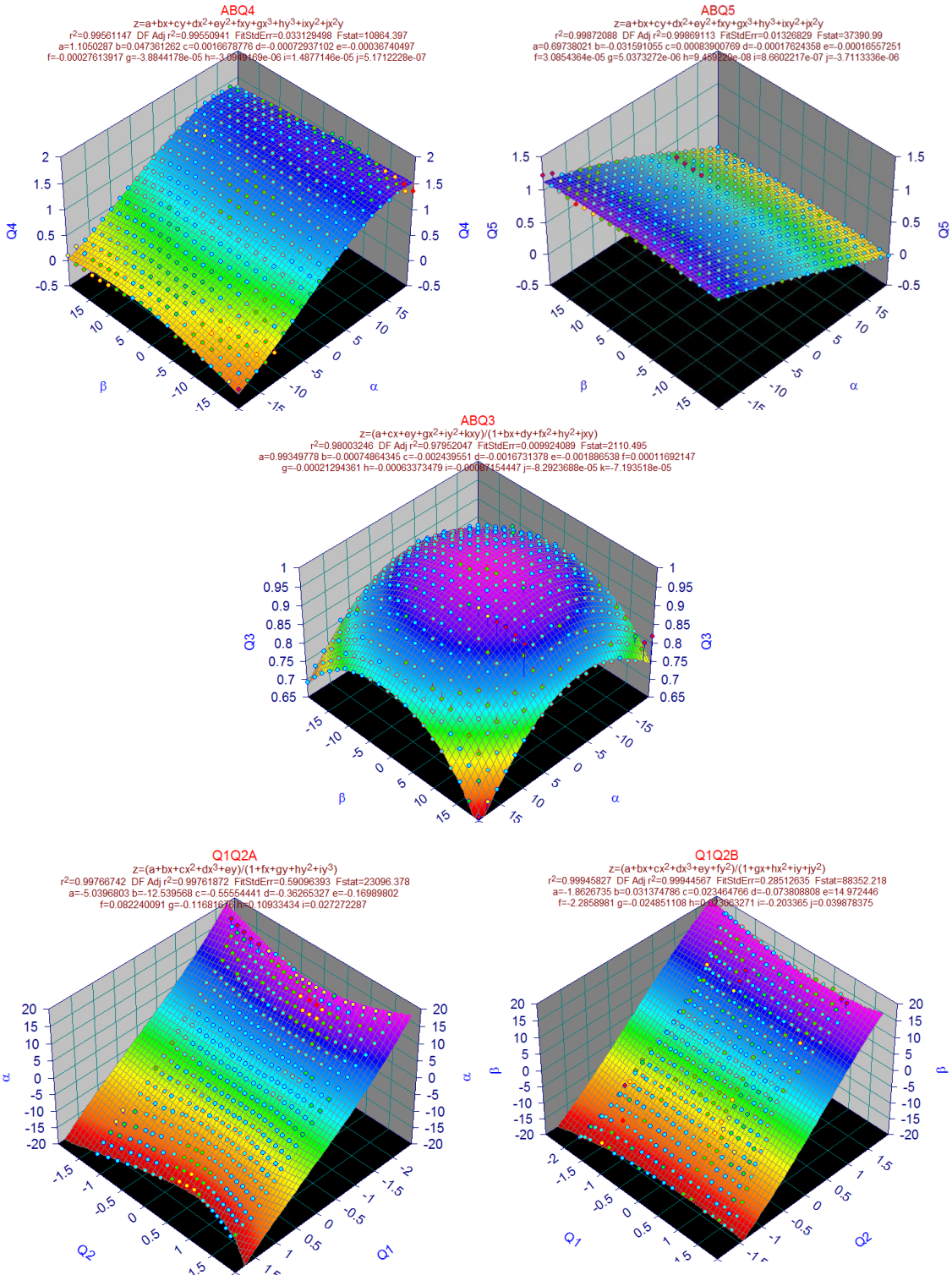

Figure 24: Calibration curves for probe installed at station 4

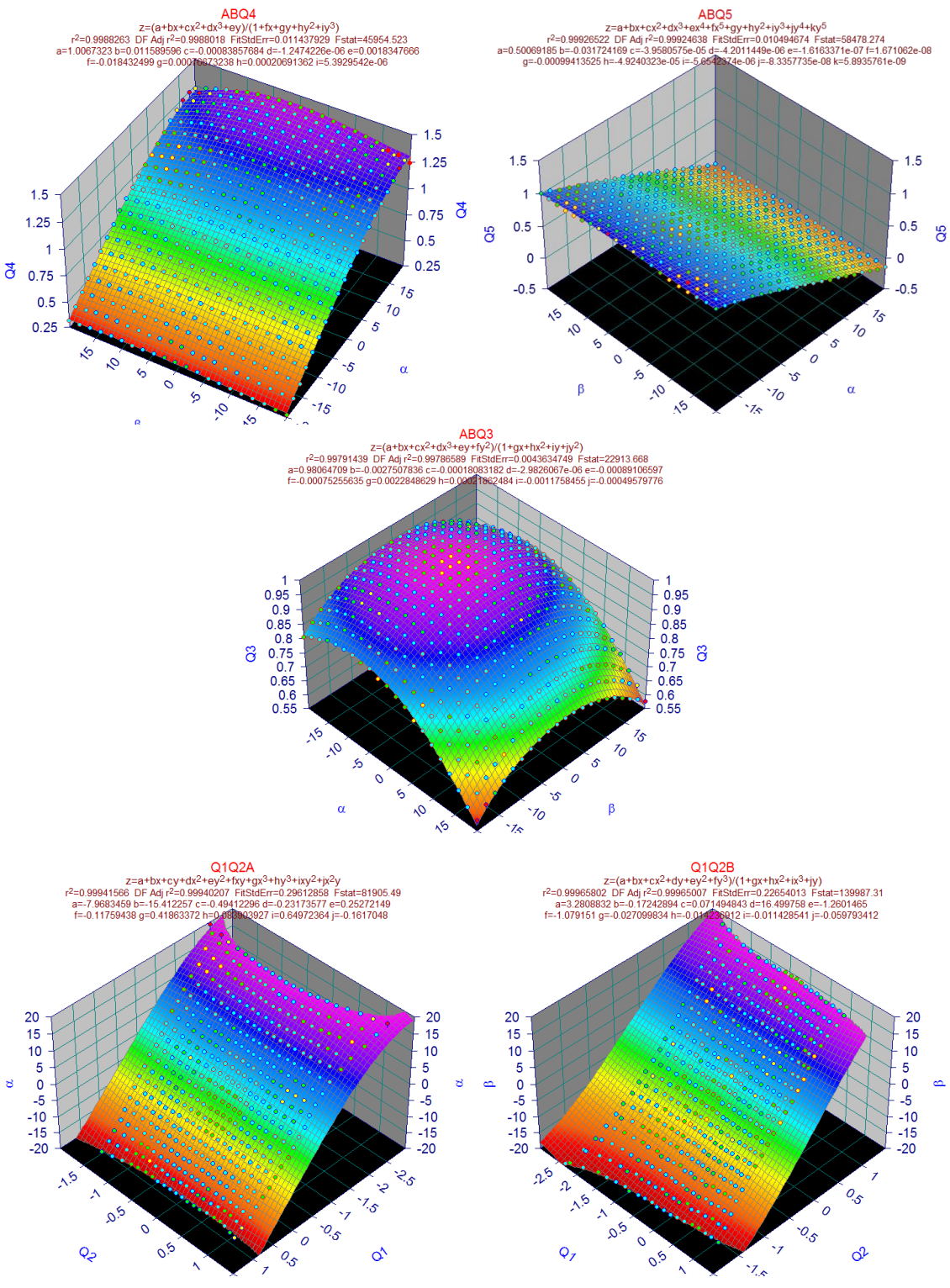

Figure 25: Calibration curves for probe installed at station 5

4.2. Film-Cooling Effectiveness Measurement Theory and Data Analysis

To record the effectiveness of film cooling, a temperature differential is created between the mainstream and the coolant in a lab setting. Since measurement surfaces such as blades, vanes, and flat plates are made of material with very low conductivity so that wall surface temperature is almost the same as film temperature, film cooling effectiveness can be estimated by measuring surface temperatures and having knowledge of mainstream and coolant temperatures.

Thermocouples placed at discrete locations are used to measure surface temperatures. IR cameras, Thermochromic Liquid Crystals, or Temperature Sensitive paint are used to map the temperature profile. Transient thermal method such as transient Liquid Crystal has been used for measuring film cooling effectiveness and the heat transfer coefficient.

To generate reliable data via thermal methods, measurement surface must be made with materials with low thermal conductivity. Dispersion of effectiveness data might happen in regions of high cooling effectiveness or in regions next to holes.

4.2.1. Mass Transfer Analogy Methods

In order to avoid the conduction related issues mass transfer analogy has been used in research centers. For example gas-chromatography was used by Nicoll and Whitelawi [63] to estimate film cooling effectiveness at various discrete locations.

Friedrichs et al. [64] utilized a diazo-coated polyester film to calculate film cooling effectiveness by using ammonia and water-vapor seeded in coolant air. Goldstein and Jin [65] saturated the coolant air with naphthalene and calculate adiabatic film cooling effectiveness by applying naphthalene sublimation.

Zhang and Jaiswal [66] proposed using Pressure Sensitive Paint (PSP). This method categorized as a non-contact mass transfer analogy and deliveres detailed film cooling effectiveness contours.

Figure 26 shows the comparison between heat transfer and mass transfer analogy for measuring film cooling effectiveness. In this figure, the y is the boundary layer direction and x is the streamwise direction. The film temperature/concentration is a function of x, y, while wall temperatures/concentrations are functions of x only. Considering a coolant temperature (T_c) injected into a mainstream flow (at T_∞), heat transfer equations are governed as below [67]:

$$G_x \frac{\partial T}{\partial x} + G_y \frac{\partial T}{\partial y} = \rho(\epsilon_T + \alpha_D) \frac{\partial^2 T}{\partial y^2} \quad (5)$$

where, ϵ_T is the turbulent thermal diffusivity. Boundary conditions are:

$$y = 0: \frac{\partial T}{\partial y} = 0, T = T_{aw} \quad (6)$$

$$y > \delta_f : T = T_\infty \quad (7)$$

$$x = 0 : T = T_C \quad (8)$$

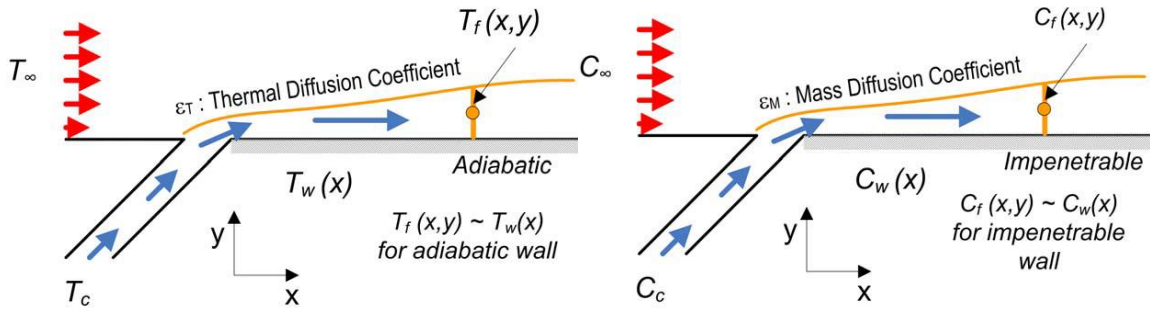

a) Thermal boundary conditions b) Mass transfer boundary conditions

Figure 26: Measurement of film cooling effectiveness using the heat/mass transfer analogy [68]

Now Consider the case, where coolant gas injected into mainstream has a tracer concentration of C_C and mainstream flow has a tracer concentration of C_{∞}. Mass transfer equation based on considering C being the mass fraction either a tracer element or a component gas are:

$$G_x \frac{\partial C}{\partial x} + G_y \frac{\partial C}{\partial y} = \rho(\epsilon_M + D) \frac{\partial^2 C}{\partial y^2} \quad (9)$$

where, ϵ_M is the turbulent mass diffusivity. Boundary conditions are:

$$y = 0: \frac{\partial C}{\partial y} = 0, C = C_w \quad (10)$$

$$y > \delta_f : C = C_\infty \quad (11)$$

$$x = 0 : C = C_C \quad (12)$$

Han and Rallabandi [68] explained "Equations (6) and (10) reflect the analogous adiabatic wall and impenetrable wall conditions respectively. It can be noticed

that Equations (5) and (9) and their boundary conditions have a similar structure. In the event that the turbulent Lewis number, $Le_T = \frac{\epsilon_T + \alpha}{\epsilon_M + D} = 1$, it is evident from the governing equations and boundary conditions that appropriately non dimensionalized solutions (temperatures or mass concentrations) will be identical.

Based on the work of Jones [69] and Kays et al. [67], the stipulation $Le_T \approx 1$ holds for turbulent gaseous flow fields, such as those encountered in gas turbine engines. And therefore:

$$\eta = \frac{T_f - T_\infty}{T_c - T_\infty} \approx \frac{T_{aw} - T_\infty}{T_C - T_\infty} \approx \frac{C_w - C_\infty}{C_C - C_\infty} \qquad (13)$$

The underlying assumption governing the heat/mass transfer analogy ($Le_T \approx 1$) requires that the flow-field be highly turbulent. This assumption is usually valid over the surface of the gas turbine vane/blade/end-wall due to the high Reynolds numbers involved as well as various secondary mechanisms further inducing turbulence in the flow-field (such as leakage vortices, horse-shoe vortices, film cooling jets and periodic rotor/stator wakes)."

Next section will focus on the determination of film cooling effectiveness using the PSP method. More detailed information is available in [68].

4.2.2. PSP Technique

PSP consists of photo-luminescent molecules held together by a binding compound. The luminous particles in the PSP emit light when excited, with the emitted

light intensity being inversely proportional to the partial pressure of oxygen in the surroundings. The emitted light intensity can be recorded using a CCD camera and corresponding oxygen partial pressures can be obtained by calibrating emitted intensity against the partial pressure of oxygen.

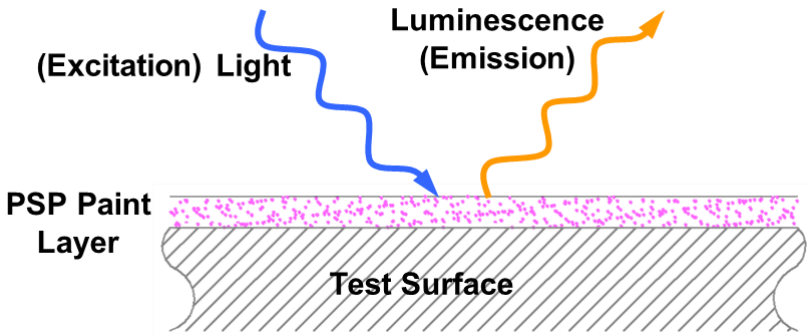

Figure 27: Principle of operation of PSP

4.2.2.1. History

Photoluminescence and oxygen quenching were first proposed as a flow visualization tool by Peterson and Fitzgerald [70] in 1980. In their experiment they covered a surface with fluorescent dye and excited it with a blue light. They then turned on the flow, and using a static pressure tap on the surface they injected nitrogen or oxygen into it. Nitrogen caused a bright luminescent streak to appear downstream due to oxygen quenching being lessened, while the injection of oxygen resulted in a dark streak downstream.

The dye used in this early experiment had low sensitivity to oxygen, and the binder's oxygen permeability was low as well. The rough and thick PSP layer wasn't

able to adhere well to the surface. For these reasons, the PSP in this experiment was not usable for accurate and practical scientific measures; however, it opened up the possibility for oxygen quenching sensors to be used to measure surface pressure.

In the early to mid-1980s, groundbreaking research at TsAGI/Moscow in tandem with Moscow University tested the potential for PSP to be used to take practical surface pressure measurements. While for a few years this research was virtually unknown to the west, in 1990 an advertisement in Aviation Week & Space Technology magazine revealed it to a larger community.

Russia's Central Aero-Hydrodynamic Institute (TsAGI) worked with INTECO (Ardasheva et al. [71], Volan and Alati [72]), an Italian firm, to develop a PSP system for aerodynamic testing that was demonstrated in the early 1990s by wind tunnel tests conducted in the United States and Germany.

In 1989, with a coating developed at the University of Washington (Kavandi et al. [73]), surface pressure field measurement using PSP was demonstrated at NASA's Ames Research Center (McLachlan et al. [74, 75]). Research continues until this day at Ames, and Boeing and McDonnell-Douglas Aerospace (Morris et al. [76], Dowgwillo, et al. [77]) also use PSP measurement for aircraft development. In addition, NASA's Langley Research Center and the United States Air Force Arnold Engineering and Development Center (AEDC) carry out PSP research. The PSP technique's high spatial resolution and low cost make it an option that is being widely adopted internationally (Engler et al. [78]).

4.2.2.2. Physics

The sensitivity of some luminescent dyes to oxygen makes the PSP technique possible. A luminescent molecule is excited by absorbing a photon, and then the molecule emits the photon at a longer wavelength to return to its ground state. Figure 28 shows the emission spectra of UniFIB PSP which was used in this study.

Oxygen quenching enables some luminescent molecules to return to the ground state without emitting a photon. Therefore, the intensity of light emitted from luminescent molecules inversely varies with local oxygen partial pressure for a given excitation level. Oxygen partial pressure can be converted to air pressure because the mole fraction of oxygen in air is fixed.

The Stern Volmer relation describes the oxygen quenching process for PSP:

$$\frac{I_{max}}{I} = 1 + Kc \qquad (14)$$

where I is luminescence intensity, I_{max} is maximum intensity without oxygen, K is the Stern-Volmer quenching constant, and c is O_2 concentration. I_{max} and K are temperature-dependent.

Henry's law relates binder oxygen concentration to PSP surface oxygen concentration:

$$c = SXP \qquad (15)$$

where S is the temperature-dependent Henry's law coefficient, X is the mole fraction of oxygen in air, and P is air pressure. Thus, the Stern-Volmer relation is rewritten as:

$$\frac{I_{max}}{I} = 1 + KSXP \qquad (16)$$

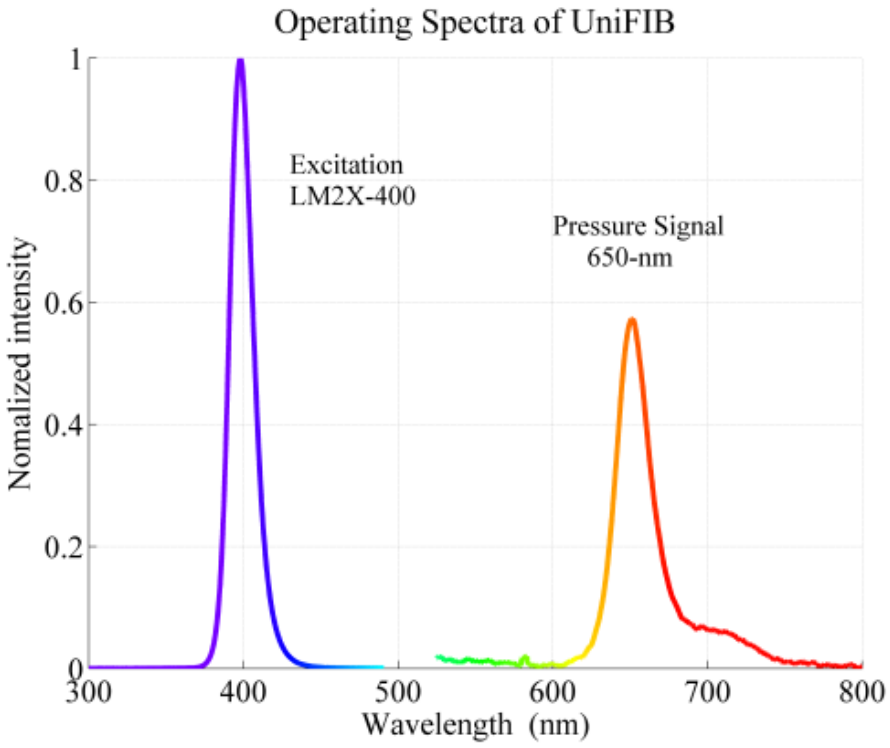

Figure 28: Emission spectra of UniFIB PSP (www.psp-tsp.com)

Now one can see the relationship between air pressure and luminescence intensity; as air pressure increases, luminescence intensity decreases. However, due to the impracticability of obtaining maximum luminescence intensity without oxygen, this form of Stern-Volmer is useless for experimental setup. Finding the ratio of intensities for two different flow conditions can enable a more useable form of this equation:

$$\frac{I_0}{I} = A(T) + B(T)\frac{P_0}{P} \quad (17)$$

where the zero subscript denotes “no-flow” condition where pressure is constant across the surface, and coefficients *A* and *B* are temperature-dependent coating sensitivities that are derived from experimental calibration.

Intensity measurements for flow on and flow off conditions must be obtained in order to utilize these equations. P_0 (pressure in flow off condition) is a known value, and *I* and I_0 are measured, so *P* can be found using the equation.

Taking the ration of these intensities also effectively factors out the effects of non-uniform illumination and PSP distribution, assuming that the geometry of the experimental setup and illumination source remains constant between measurements of *I* and I_0.

In addition, one must assume that the excitation illumination intensity is sufficiently low that most luminescent models are in ground state. If intensity is too high, most of the molecules will be excited, causing *A* and *B* to also become functions of illumination intensity.

4.2.3. Film Cooling Effectiveness Measurement Using PSP

The image intensity obtained from PSP by the camera during data acquisition is normalized with a reference image intensity taken under no-flow conditions. Background noise in the optical setup is removed by subtracting the image intensities

with the image intensity obtained under no-flow conditions without excitation. The resulting intensity ratio can be converted to pressure ratio using the previously determined calibration curve and can be expressed as

$$\frac{I_{ref} - I_{blk}}{I - I_{blk}} = f\left(\frac{\left(P_{O_2}\right)_{air}}{\left(P_{O_2}\right)_{ref}}\right) = f\left(P_{ratio}\right) \qquad (18)$$

Where I denotes the intensity obtained for each pixel and $f(P_{ratio})$ is the relation between intensity ratio and pressure ratio obtained after calibrating the PSP. Further details in using PSP for pressure measurements are given in McLachlan and Bell [75].

Calibration for PSP was performed using a vacuum chamber at several known pressures varying from 0 to 2*atm* with corresponding emitted intensity recorded for each pressure setting. Calibration setup and a sample calibration curve are shown in Figure 29 and Figure 30 respectively.

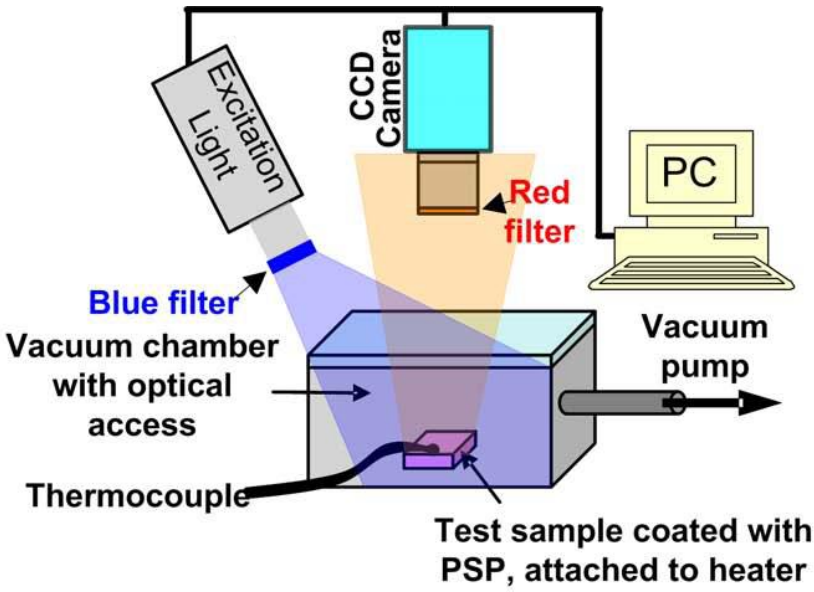

Figure 29: PSP calibration setup

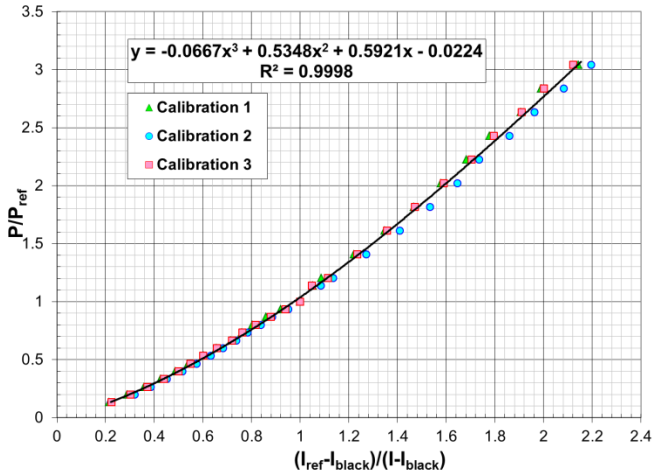

Figure 30: PSP calibration curve

PSP is sensitive to temperature with higher temperatures resulting in lower emitted light intensities. Hence, the paint was also calibrated for temperature. It was observed that if the emitted light intensity at a certain temperature was normalized with

the reference image intensity taken at the same temperature, the temperature sensitivity can be eliminated. Hence, during data acquisition, the reference image was acquired immediately after the experiment was completed to avoid errors related to temperature variation. Reference images were acquired after the rotor came to a halt and the temperature change from rotating to stationary condition was small enough to disregard its effect on PSP measurement. Coolant flow and platform surface temperatures were monitored using thermocouples placed along the individual coolant loops and on the platform surface close to the suction side respectively. The thermocouples were wired through the slip-ring and connected to a microprocessor thermometer with a digital readout.

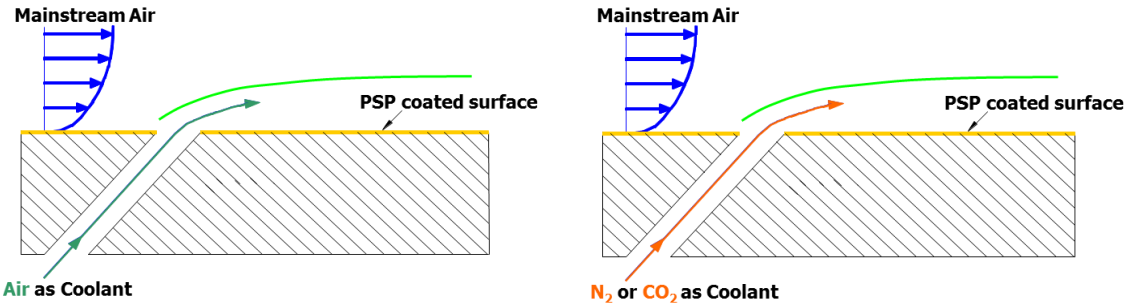

(a) Test with air as a coolant

(b) Test with foreign gas (N_2 or CO_2) as a coolant

Figure 31: calculating film cooling effectiveness by using two coolants alternatively

To obtain film cooling effectiveness, air and nitrogen were used alternately as coolant (Figure 31). Nitrogen which has approximately the same molecular weight as the air displaces the oxygen molecules on the surface causing a change in the emitted light intensity from PSP. By noting the difference in emitted light intensity and subsequently

the partial pressures between the air and nitrogen injection cases, the film cooling effectiveness can be determined using the following equation:

$$\eta = \frac{C_{mix} - C_{air}}{C_{N_2} - C_{air}} = \frac{C_{air} - C_{mix}}{C_{air}} = \frac{\left(P_{O_2}\right)_{air} - \left(P_{O_2}\right)_{mix}}{\left(P_{O_2}\right)_{air}} \quad (19)$$

Where C_{air}, C_{mix} and C_{N2} are the oxygen concentrations of mainstream air, air/nitrogen mixture and nitrogen on the test surface respectively and are directly proportional to the partial pressure of oxygen.

The accuracy of the PSP technique for measuring film-cooling effectiveness has been compared by Wright et al. [79] on a flat plate with compound angled ejection holes against several measurement techniques such as steady and transient liquid crystal, IR camera and using a foil heater with thermocouples. Results were obtained for a range of blowing ratios and show consistency with each other. Study by Wright et al. [79] for flat-plate film cooling shows the superiority of using PSP compared to conventional IR measurement. From their study, the accuracy analysis shows the difference of effectiveness result of 15%. In addition, Rallabandi et al. [80] reports a good comparison between PSP and other methods such as naphthalene mass-transfer method and traditional thermocouples measurement technique, for basic flat-plate film cooling with one row of compound angle holes.

4.2.4. Experimental Procedure for Endwall Film Cooling

This study examines a platform passage that was layered with an air brush with 7 to 9 coats of PSP. A green strobe light fitted with narrow bandpass interference filter with a 520 nm optical wavelength was then used to excite the PSP coated surface, which caused the surface to emit greater than 600 nm wavelength red light. To record intensity images, a scientific grade 12-bit high speed SensiCam (with CCD temperature maintained at -15° C using a 2-stage Peltier cooler) that used a 35 mm lense and a 600 nm longpass filter was utilized. The specific filters chosen enabled the camera to only capture data, blocking light reflected from the surface of the target. An optical sensor triggered by the rotor shaft simultaneously triggered the camera, strobe light and data acquisition system (Figure 32).

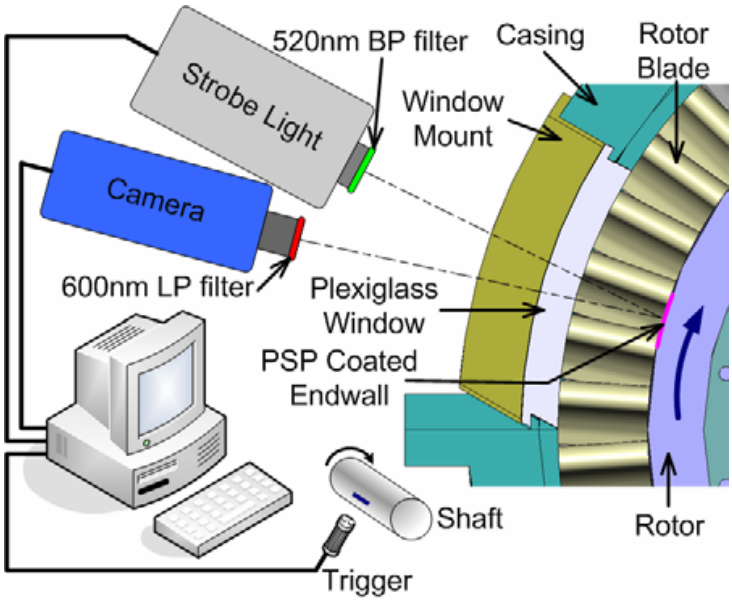

Figure 32: Optical set-up for endwall film cooling using PSP [27]

The camera was able to detect the angular position in able to capture the same region of interest in every rotation, so that the image intensities could be averaged without blurring information. 17 μs was the minimum exposure time used to capture images. At 2550 rpm, estimated rotor movement during this exposure time was 1.1 mm. With air and nitrogen injection, 200 images were captured for each experiment, and pixel intensity was averaged for all of the images. Pixel intensities were converted into pressure via a computer program using the calibration curve, and this was used to find film cooling effectiveness. Desired blowing and mass flow ratio had been previously calculated, and a rotameter used these values to set the coolant flow rate. To eliminate the effects on temperature of PSP, coolant was heated to 45° (the temperature of mainstream air) before injection through the gap.

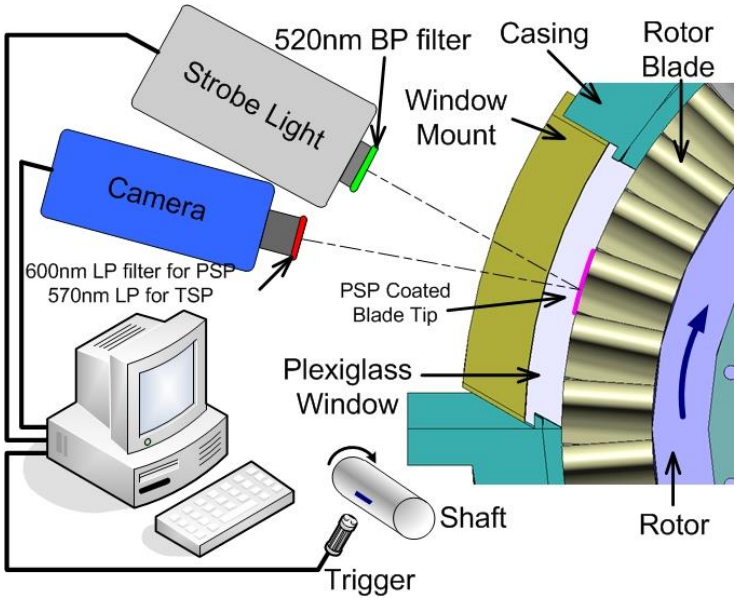

Figure 33: Optical set-up for blade tip film cooling using PSP

4.2.5. Experimental Procedure for Blade Tip Film Cooling

The optical setup for blade tip film cooling experiment is shown in Figure 33. The tip of the blades under investigation was layered with 7 to 9 coats of PSP using an air brush. The procedure is same as endwall film cooling data acquisition, except the camera and strobe light point at blade tip. A total of 200 images were captured for each experiment with air and nitrogen injection and the pixel intensity for all images was averaged. A computer program was used to convert these pixel intensities into pressure using the calibration curve and then into film cooling effectiveness. The coolant flow rate was set using a rotameter based on prior calculation for the desired blowing ratio. The coolant was heated to the same temperature as mainstream air (45°C) before injection through the gap to eliminate the temperature effects of PSP.

4.2.6. Uncertainty Calculations

Uncertainty calculations were performed based on a confidence level of 95% and are based on the uncertainty analysis method of Coleman and Steele [81]. Detailed uncertainties calculations are explained in Appendix B. Lower effectiveness magnitudes have higher uncertainties. For an effectiveness magnitude of 0.8, uncertainty was around ±1% while for effectiveness magnitude of 0.07, uncertainty was as high as ±10.3%. This uncertainty is the cumulative result of uncertainties in calibration (4%) and image capture (1%). The absolute uncertainty for effectiveness varied from 0.01 to 0.02 units. Thus, relative uncertainties for very low effectiveness magnitudes can be very high (>100% at effectiveness magnitude of 0.01). However, it must be noted that very few

data points exist with such high relative uncertainty magnitudes. Uncertainties for the average blowing ratio calculations are estimated to be approximately 3.5% using Kline-McClintock analysis and are discussed in detail by Holman [82].

5. ENDWALL FILM-COOLING RESULTS*

Film cooling effectiveness measurements were performed for three coolant-to-mainstream mass flow ratios (MFR) of 0.5%, 1.0% and 1.5%. Film cooling data was also obtained for three rotational speeds; 3000 rpm (reference condition), 2550 rpm and 2400 rpm, and they were compared with non-contoured endwall data. For 3000 rpm two more MFRs of 0.75% and 1.25% were performed to give a better view of how film cooling effectiveness is changing.

Total mass flow in the engine was 3.58 kg/s and was ensured to be the same for all three rpms by adjusting the blower frequency through the frequency controller. The three MFRs corresponded to blowing ratios (M) of approximately 0.372, 0.744 and 1.116 respectively after assuming that the coolant exits the gap axially. Blowing ratios for each rotating speed differed slightly as the relative mainstream velocity at the rotor inlet changes with the rotating speed.

5.1. Mass Flow Ratio Effect

The film cooling effectiveness resulting from using PSP for the reference rotating condition of 3000 rpm are plotted in Figure 34. The figure shows the contour plots for all five mass flow ratios tested. The contour plots also show the location of the stator-rotor gap upstream of the passage and the path of the mainstream and coolant flow. The

* Reprinted with permission from "Experimental Investigation of the Effect of Purge Flow on Film Cooling Effectiveness on a Rotating Turbine with Non-Axisymmetric Endwall Contouring," by M. Rezasoltani, M. T. Schobeiri and J. C. Han, J. Turbomach. 2014; 136(9), GT2013-94807, Copyright © 2014 by ASME.

effectiveness in the gap as the coolant escapes through it could not be recorded, as the plexiglass window through which the rotor platform was viewed was not wide enough.

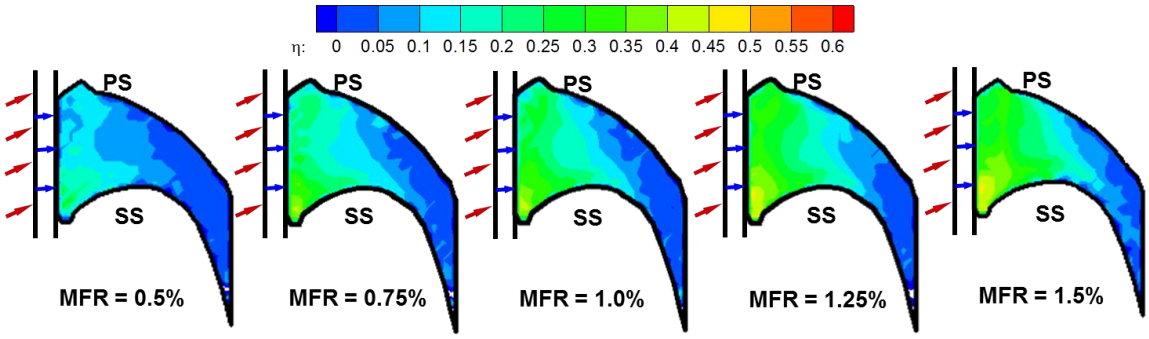

Figure 34: Film cooling effectiveness distribution on the contoured rotating platform for 3000 rpm

Results show that Film cooling effectiveness increases with purge mass flow rate from 0.5% to 1.5%. At lower blowing ratios, the low momentum coolant is not capable of penetrating into the highly vortical secondary flow region on the hub platform. It mixes with the main flow where its kinetic energy dissipates, making only a marginal contribution to effectiveness improvement. For the lowest mass flow ratio (MFR = 0.5%), the maximum effectiveness magnitude is less than 0.2. As the mass flow ratio increases, the coolant injection velocity increases because the coolant can penetrate the complex secondary flows in the passage, resulting in higher effectiveness on the platform.

5.2. Contouring Effect

Figure 35 shows Comparison of film cooling effectiveness distribution on the contoured and non-contoured rotating platform for 3000 rpm. For both contoured and

non-contoured endwalls, higher mass flow ratios resulted in coolant injection with higher momentum. As this momentum increases, it can be observed that the spread of the coolant as well as the effectiveness magnitudes are increased. The injected coolant is at the same density as the mainstream i.e. the coolant to mainstream density ratio is 1. Hence, the injected coolant velocity is higher for higher mass flow ratios. This affects the secondary flow structure in the passage.

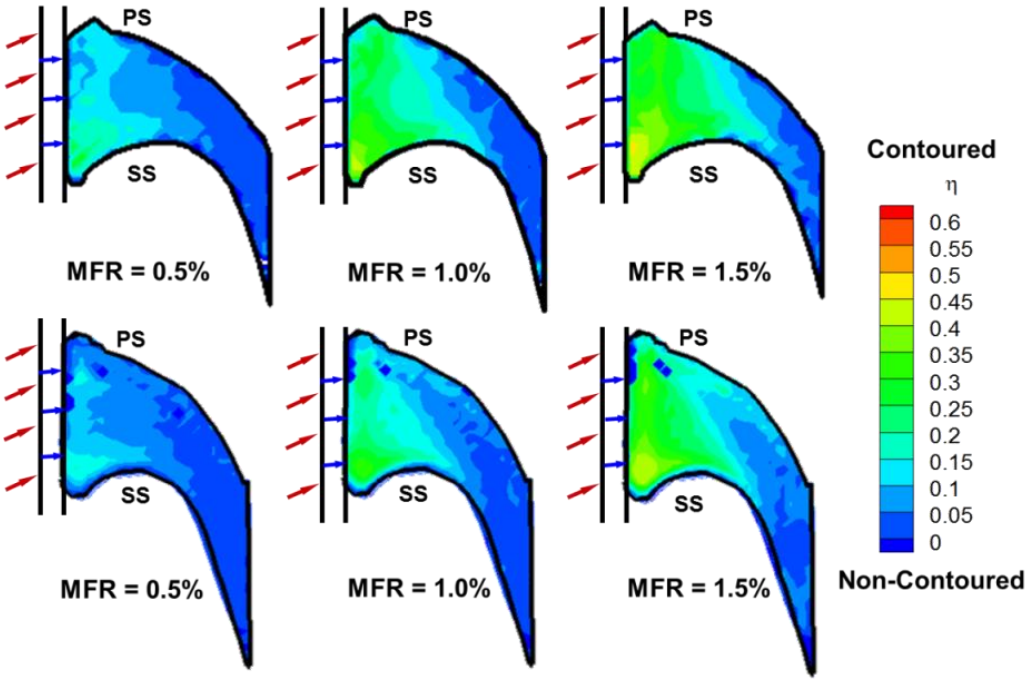

Figure 35: Comparison of film cooling effectiveness distribution on the contoured and non-contoured rotating platform for 3000 rpm

In non-contoured platform a strong pressure gradient exists within the passage from the pressure to the suction side, with the static pressure near the pressure side being much higher due to lower mainstream velocities and blade curvature. The coolant traces

show slightly higher effectiveness magnitudes towards the suction side near the leading edge. More coolant gets diverted away from the higher pressure stagnation region on the leading edge of the blade and finds its way towards the suction side. Effectiveness magnitudes on the pressure side begin to fade away rapidly as the coolant travels along the axial chord. As the passage vortex moves towards the suction side while gaining strength, it entrains the mainstream on the platform surface damaging the coolant film and resulting in a sharp drop in effectiveness magnitudes. This sudden drop gives a good indication of the path traced by the passage vortex.

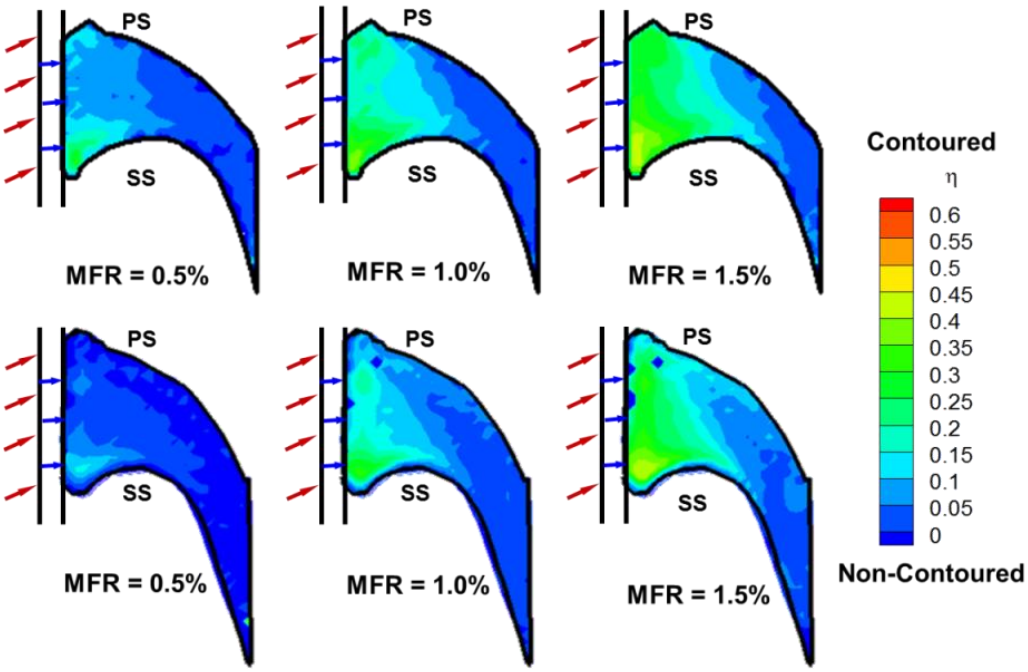

Figure 36: Film cooling effectiveness distribution on the contoured and non-contoured rotating platform for 2550 rpm

On the other hand, in the contoured platform, effectiveness magnitude spreads uniformly from leading edge to trailing edge as shown in Figure 35, Figure 36 and Figure 37. This is the consequence of the endwall contouring that has reduced the pressure difference between the pressure and suction surface leading to lower secondary flow velocities.

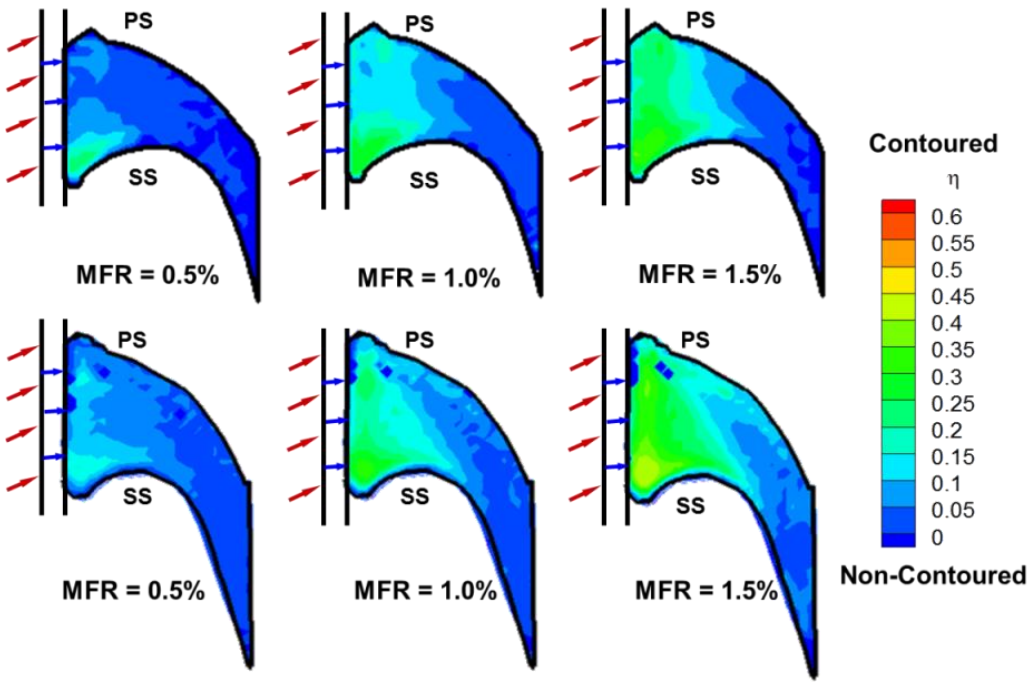

Figure 37: Film cooling effectiveness distribution on the contoured and non-contoured rotating platform for 2400 rpm

5.3. Variation of Rotating Conditions

At rotational speeds lower than the design speed, the blade flow deflection becomes larger leading to higher specific stage load coefficient, and the stagnation region moves towards the pressure side as the flow incidence angle increases, as

sketched in Figure 38. At lower rotating speeds, the stagnation point will further move towards the blade pressure side resulting in a higher pressure zone close to the pressure surface. The concentration of higher pressure on the pressure side causes a significant movement of the coolant film on the platform surface when it exits from the stator-rotor gap. The local coolant mass flow is pushed toward the suction surface causing the film to cover only smaller portions of the suction surface leading edge. This phenomenon can be clearly observed from data taken for 2550 rpm and 2400 rpm as shown in Figure 36 and Figure 37. Both figures include contour plots for 3 different mass flow ratios. More coolant appears to come out from near the suction side of the platform where the pressure difference across the gap is larger with the lower rotational speed.

By comparing Figure 36 and Figure 37 for lower rotating speeds with Figure 34 at 3000 rpm (reference speed), it can be observed that the effectiveness magnitudes decrease with lower rpm for the same mass flow ratio. This may be a result of stronger horseshoe vortices close to the suction side due to the shift in the flow incidence angle at lower rpm. For both reference and lower rotating speeds, the region downstream of the throat remains uncooled. The secondary flow vortices in the passage erode the coolant film before it reaches the throat.

In addition to the effect on static pressure distribution and film cooling due to the change in incidence angle of the inlet flow along with rotational speed, rotation also affects the coolant flow as it exits the stator-rotor gap. The gap and the disk cavity are bounded by two walls, the stator endwall and the rotor platform. The enclosed coolant

mass in the disk cavity will rotate with a certain frequency due to the cavity wall shear stress. High shear stresses, caused by relative motion in the circumferential gap, introduce some swirl in the coolant flow as it exits. Hence, a tangential component exists in the coolant flow as it exits the stator-rotor gap. This causes some additional spreading of the coolant which cannot be achieved for film cooling studies in stationary cascades.

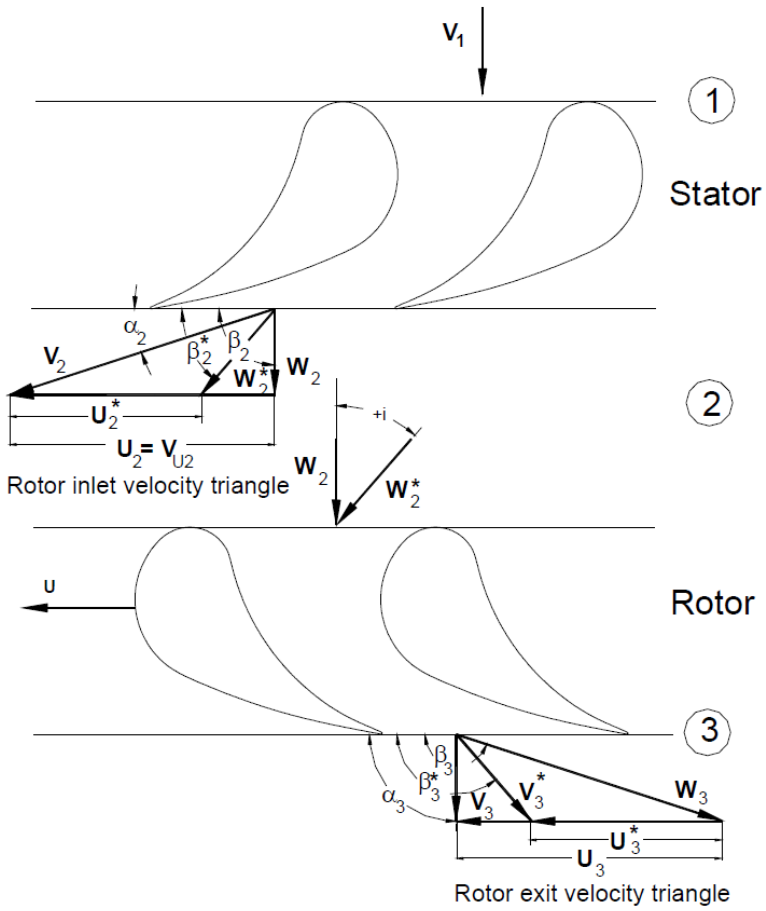

Figure 38: Velocity triangles and relative inlet and exit flow angles for design speed and off-design rotating speeds [27]

This might also explain the larger coolant spread with increasing rotational speeds due to a larger tangential velocity component in the coolant as it exits the gap. The determination of the swirl angle as well as the measurement of this tangential velocity component was not the subject of the current paper. However, these are items of high importance along with the inter-stage measurements.

5.4. Pitch-wise Average Film Cooling Effectiveness

The film cooling effectiveness results were averaged along the pitch-wise direction and the averaged data for all coolant-to- mainstream mass flow ratios and rotational speeds are presented in Figure 39 along the axial chord. The increase in effectiveness magnitudes with increasing mass flow ratio can be clearly observed from these figures. The averaged plots show a sharp decrease in effectiveness magnitude along the axial chord as indicated earlier with the region beyond x/C_x = 0.6 remaining mostly uncovered with average effectiveness magnitudes below 0.1. The decrease in effectiveness with lower rotational speeds can also be discerned.

Figure 39 depicts the averaged effectiveness distribution in axial direction with mass flow ratio as a parameter for contoured and non-contoured reference cases for given rotational speeds of 3000 rpm, 2550 rpm and 2400 rpm. As seen, for the given MFRs close to the leading edge, the patterns of the contoured cases differ substantially from the non-contoured ones. While the effectiveness distributions of non-contoured cases at the leading edge start at much lower effectiveness, the contoured cases systematically reveal higher effectiveness distributions from the leading edge to the

trailing edge. These systematic distributions of the film effectiveness with higher starting values are the consequence of the endwall contouring that made possible a continuous reduction of the secondary flow velocity from the pressure to suction surface. This systematic pattern is observed for all three rotational speeds even for the 2400 rpm, which is an extreme off-design condition.

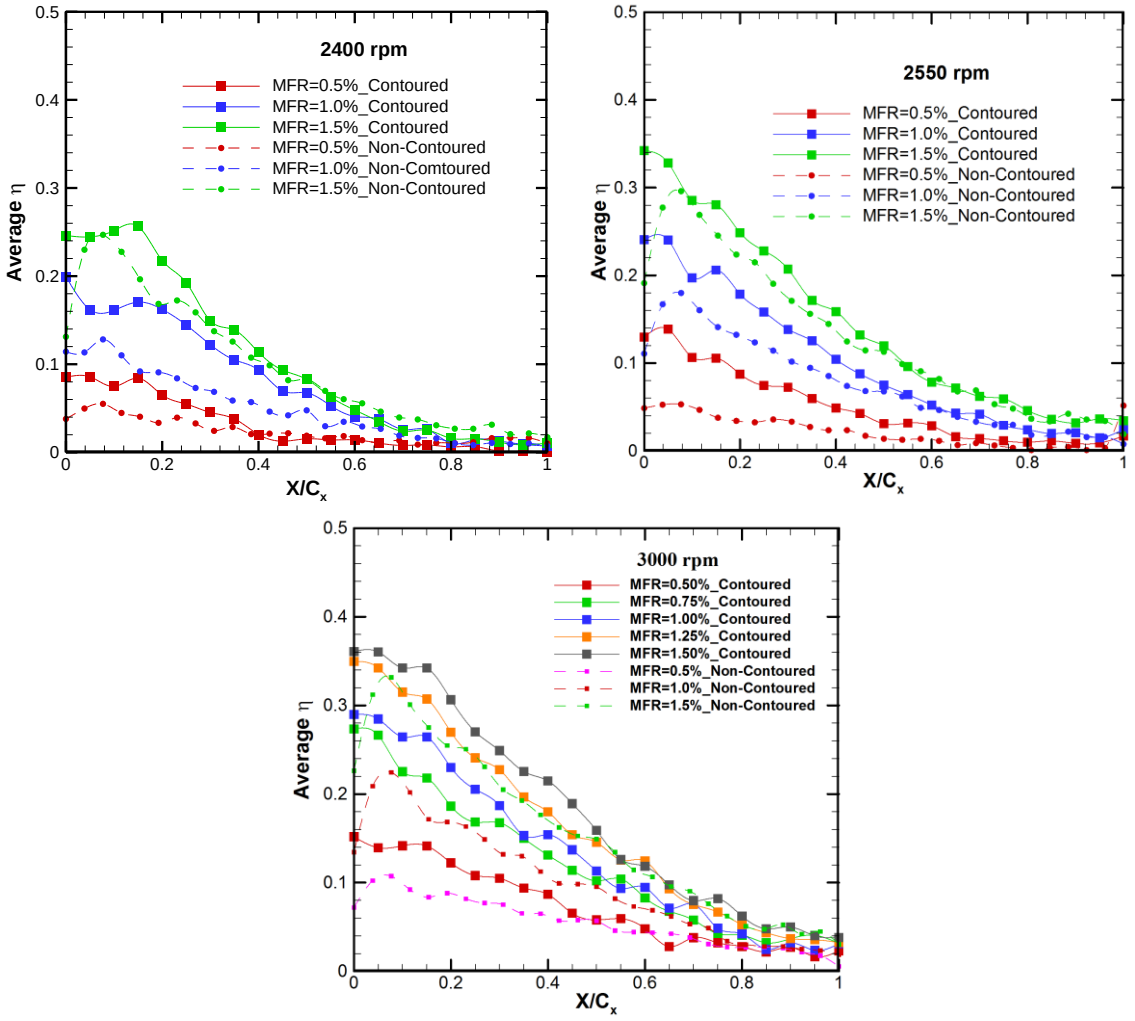

Figure 39: Pitch-wise average film cooling effectiveness distribution along axial chord for different rpms (Blowing ratio for MFR=0.5%, 1.0% and 1.5% are M=0.372, 0.744, and 1.116 respectively)

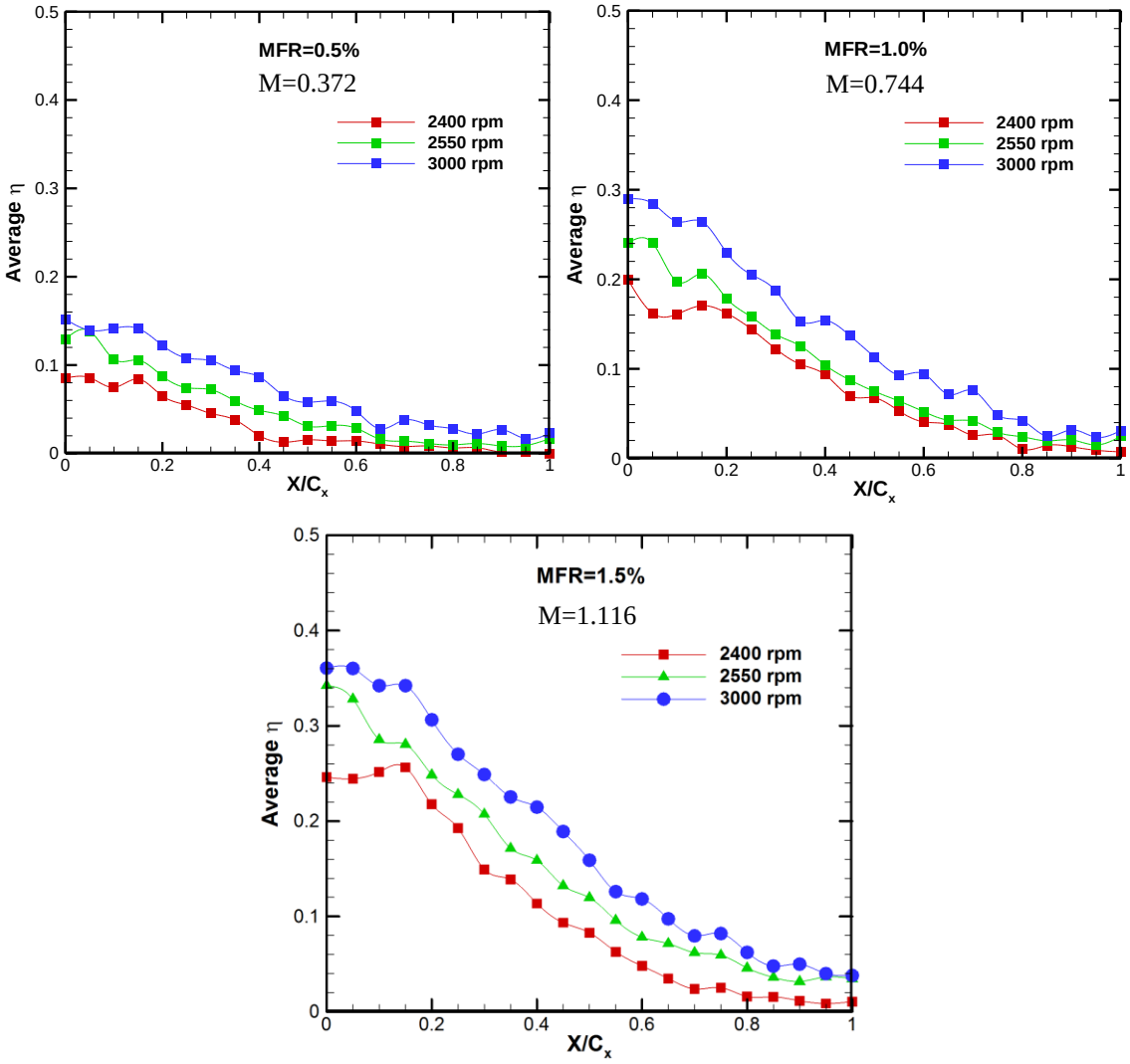

Figure 40: Pitch-wise average film cooling effectiveness distribution along axial chord for different MFRs

By comparing the contoured and non-contoured plots, it is concluded that the pressure difference between pressure side and suction side is lower than non-contoured which causes uniform distribution of film cooling effectiveness in the contoured platform. Moreover, the lower pressure difference between the pressure side and suction side reduces the strength of horseshoe vortices and therefore less mixing occurs between

the coolant and the mainstream flow and as a result there is higher film cooling effectiveness in contoured platform.

Impact of the rotational speed on the film cooling effectiveness is illustrated in three diagrams of Figure 40. It shows the pitch-wise averaged film cooling effectiveness results plotted for the three different MFRs. The impact of turbine rotational speeds on film cooling effectiveness can be clearly perceived from these plots. As rpm increases, the effectiveness magnitudes increase for the same mass flow ratio.

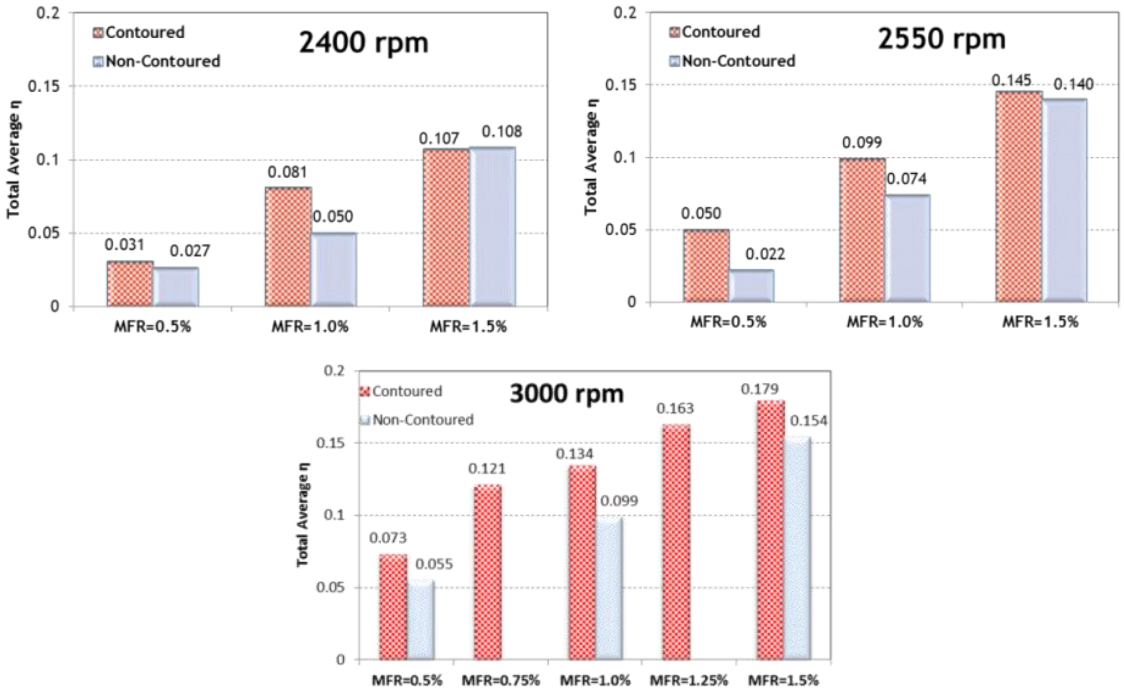

Figure 41: Total average film cooling effectiveness for different rpms

As seen in Figure 39 and Figure 40, for the contouring endwall, the first 30% of the endwall is sufficiently covered. In non-contoured cases, the coverage of the first 10%

is not satisfactory. This reduces the non-contoured coverage to 20% only. Regarding the remaining 70%, different cooling schemes such as installing film cooling holes must be applied as detailed in [27].

Further information regarding the impact of contouring on total averaged effectiveness is provided by Figure 41 to evaluate the overall impact of contouring on effectiveness. For all rotational speeds, the contoured endwall shows higher values. As shown in this figure, by increasing the MFR to 1.5% the difference between total average film cooling effectiveness in contoured and non-contoured cases becomes lower.

5.5. Influence of Coolant Density on Contoured Endwall Film-cooling

The Majority of the work on film-cooling has been implemented with coolant-to-mainstream density ratios close to 1.0. This is far from the actual density ratio in real turbines due to the temperature difference between the coolant and the hot mainstream. According to different gas turbine designs for platform film cooling, the density ratio changes from 1.5 to 2.0. In this investigation two PSP tests at density ratios of DR=1.0 (using N2 as coolant) and 1.5 (using CO2 as coolant) were performed on the same platform geometry at 3000 rpm and MFR=1%.

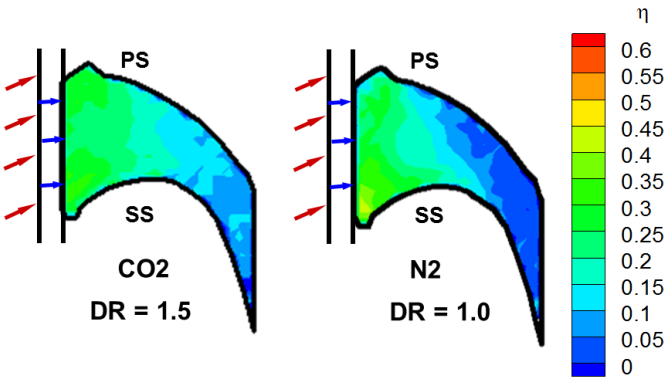

Figure 42: Film cooling effectiveness distribution at two different density ratios at 3000 rpm and MFR=1%

According to Narzary et al. [83], for coolant-to-mainstream density ratio greater than 1.0, Equation (15) could be modified to

$$\eta = 1 - \frac{1}{\left\{\left(\frac{p_{O_2,m}}{p_{O_2,c}} - 1\right)\frac{MW_c}{MW_m} + 1\right\}} \qquad (20)$$

As shown in Figure 42 and Figure 43, film-cooling effectiveness improved with increasing density ratio. In DR=1.5 the passage platform is almost covered with film cooling. Due to conservation of mass, since the density is increasing, the velocity must decrease which causes the momentum to decrease, and provides higher effectiveness downstream along the endwall passage (compared to lower density coolant like N_2).

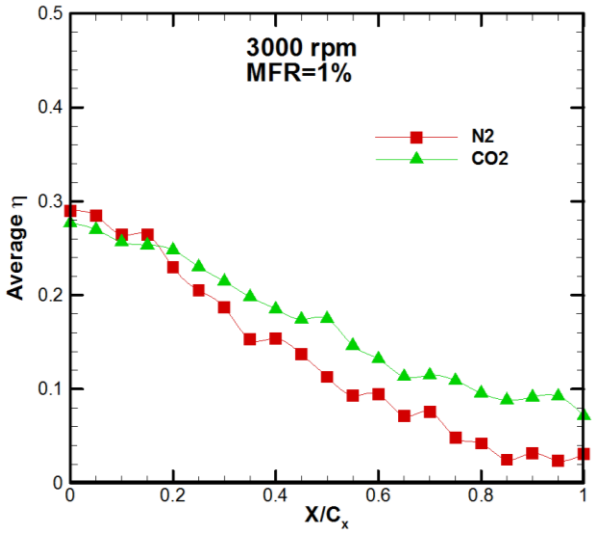

Figure 43: Pitch-wise average film cooling effectiveness distribution for two different coolant at 3000 rpm, MFR=1%

6. BLADE TIP COOLING MEASUREMENTS*

In this section blowing ratio effect and rotation effect will be discussed for each configuration. Film cooling effectiveness measurements were performed for three blowing ratios (M) of 0.75, 1.25 and 1.75. Film cooling data was also obtained for three rotational speeds; 3000 rpm (reference condition), 2550 rpm and 2000 rpm. Experimental measurement have been done for four different tip configurations: plane tip with tip hole cooling, squealer tip with tip hole cooling, plane tip with pressure-side-edge compound angle hole cooling and squealer tip with pressure-side-edge compound angle hole cooling. In order to show the flow behavior at the tip of the blade some CFD results are used. The CFD part was performed by Kun Lu [56].

6.1. Blowing Ratio Effect

For all cases higher blowing ratios resulted in coolant injection with higher momentum. The injected coolant is at the same density as the mainstream i.e. the coolant to mainstream density ratio is 1. Hence, the injected coolant velocity is higher for higher blowing ratios. This affects the secondary flow structure in the passage for each configuration.

6.1.1. Plane Tip with Tip Hole Cooling

The film cooling effectiveness resulting from using PSP for the reference rotating condition of 3000 rpm are plotted in Figure 44. The figure shows the contour plots for all three blowing ratios tested on the plane tip. The contour plots also show the location of the seven tip cooling holes.

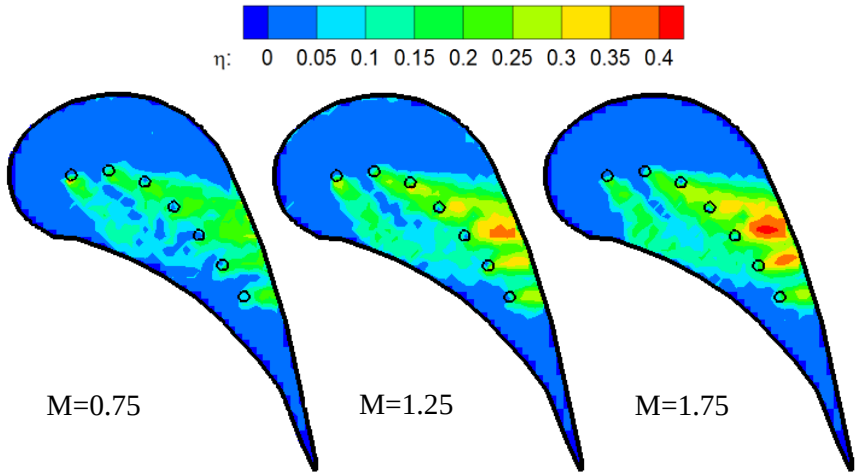

Figure 44: Film cooling effectiveness measured for plane tip with tip hole cooling at 3000 rpm

At M=0.75 the trajectory of each hole appears as a narrow streak and can be approximately differentiated from each other due to the relatively small blowing ratio. The cooling effectiveness is around 0.2 within the coolant trajectories. The highest value of nearly 0.3 is obtained right at the downstream of the cooling-hole exits. The downstream cooling effectiveness is gradually decreased due to the diffusion of cooling jets and the mixing between the coolants and the leakage flow. As the blowing ratio increases to M=1.25 each coolant trajectory tends to diffuse more and thus covers more

area. The trajectories of the cooling jets exiting from the first, the sixth and the seventh holes are easily identified, whereas a large area with high effectiveness appears in the vicinity of the rest of the cooling holes due to the coolant accumulation. It is noticeable that the highest film cooling effectiveness (above 0.35) is observed in the vicinity of the last four cooling holes. In the case of M=1.75, the trajectory tends to be thicker and thus the film cooling performance is even better as expected. Higher film cooling effectiveness is achieved especially when it comes to the last four cooling holes due to the coolant accumulation. Around 50% of the blade tip surface is covered by the film coolant.

Looking at the shape of the high effectiveness area, the shape has high coincidence with the trajectories of cooling jets. Hence the adiabatic film cooling effectiveness largely reflects the consequence of the flow behaviors. Figure 45 depicts the corresponding streamline patterns at the blade tip region. Since the object of the current study is a rotor blade rotating at 3000 rpm with the tip speed of 215.34 m/s, the streamlines are plotted based on the relative velocity in the rotating coordinates.

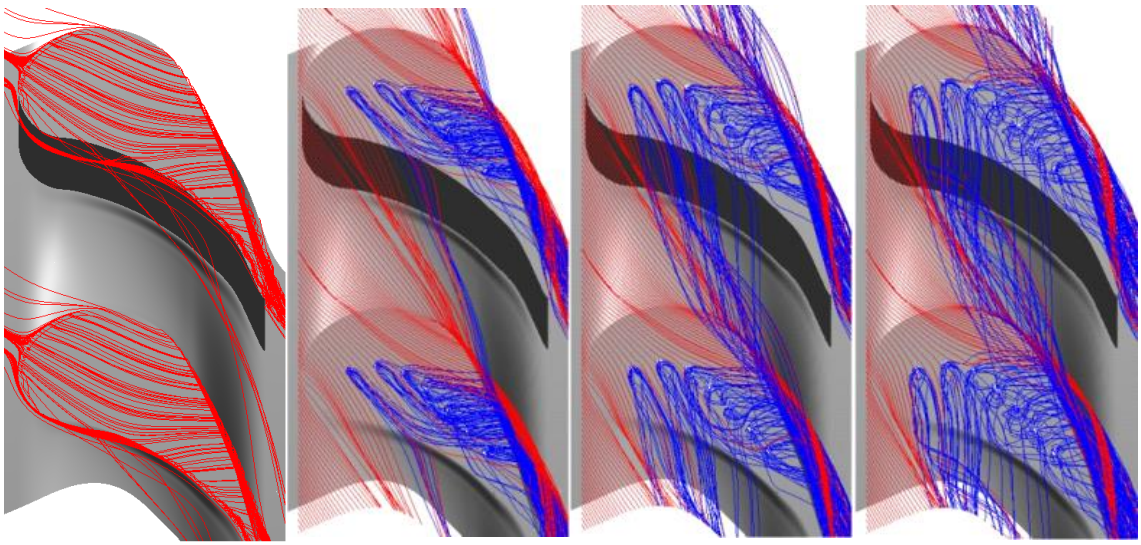

Without film cooling M=0.75 M=1.25 M=1.75

Figure 45: Streamlines based on the relative velocity (CFD results) at 3000 rpm (blue indicates cooling air, red is freestream air) for plane tip with tip hole cooling [56, 57]

Many factors can affect the film cooling effectiveness. One of the critical parameters is the blowing ratio. Another one is the blade tip geometry. Due to the blunt and round leading edge of the blade, the pressure difference at the leading edge is not as high as that between the pressure side and suction side. Consequently, the mainstream particles entering the tip gap are not deflected immediately. Nevertheless, they keep traveling a distance along the initial direction until the pressure difference becomes high enough to push them to the suction side at about 30% of C_{ax}. As a result, a small amount of flow leaks from the pressure side of the leading edge, whereas the majority moves towards the suction side forming a system of tip vortices.

Figure 46 depicts the static pressure distribution at the blade tip region for blowing ratios of M=1.25 at 3000 rpm. For the plane tip without film cooling holes, the

typical pressure distribution is obtained. The pressure side (PS) has the highest pressure and the pressure is gradually decreased towards the suction side (SS). The resulted pressure difference pointing from PS to SS is the primary driving force of the tip-gap leakage flow.

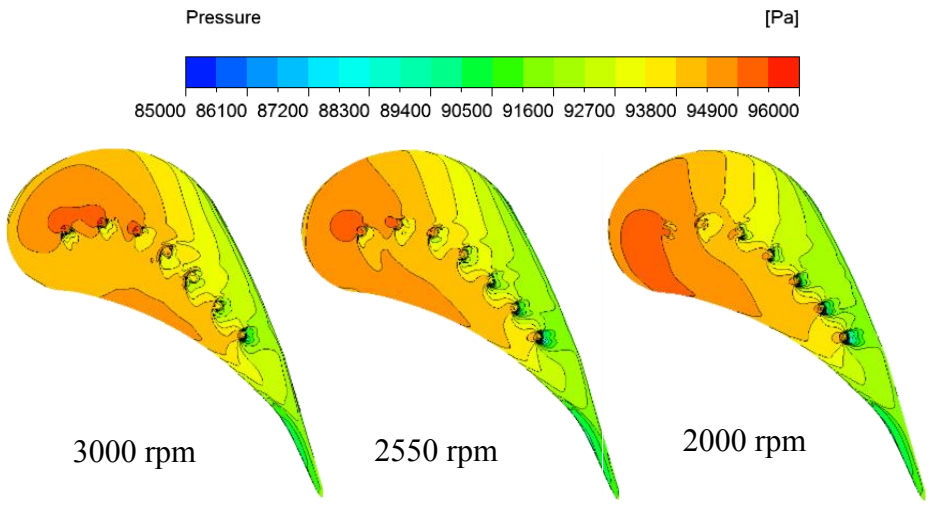

Figure 46: Distribution of the static pressure (CFD results) at plane tip with tip hole cooling [56, 57]

Based on the Figure 44 and Figure 45 all the coolant particles exiting from the first and second cooling holes travels across the pressure side and form a passage flow by mixing with the mainstream. Meanwhile, the rest of the majority appears to accumulate in the vicinity of cooling-hole exits. The coolant spreads more widely and covers more of the tip, which is virtually the result of the impact of both the pressure difference and the relative motion between the tip and shroud.

It is shown that the coolant particles tend to travel in the opposite direction of rotation, especially for the cooling jets exiting from the first two cooling holes. This

phenomenon is due to the rotation and does not exist in a stationary cascade. While in this specific hole configuration, the jets tend to exit radially, and the circumferential motion of the rotor causes the blade tip to move away from the jets. As a result the particle moving along a relative streamline with a relative velocity tangent to the streamline.

6.1.2. Squealer Tip with Tip Hole Cooling

Different effectiveness contours were obtained when it comes to the squealer tip. As shown in Figure 47, more area of the squealer tip is protected by the film cooling when compared with the plane tip. However, the local cooling effectiveness on the squealer tip tends to be lower. The impact of the blowing ratio on the cooling effectiveness might be less important for the squealer tip.

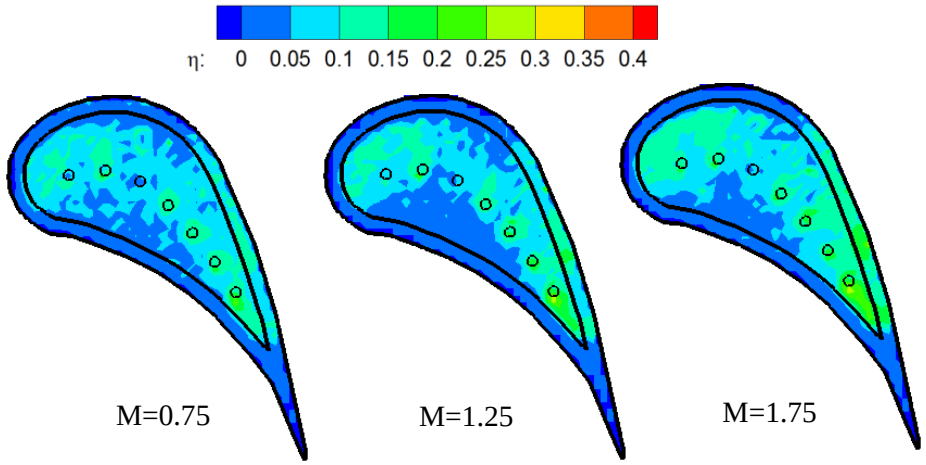

Figure 47: Film cooling effectiveness measured for plane tip with tip hole cooling at 3000 rpm

At all blowing ratios, nearly the entire cavity floor is to some extent protected by the cooling film. Apparently the area of the cavity close to the pressure side is not cooled, whereas cooling effectiveness on the rest of the cavity floor is almost above 0.1. Maximum effectiveness is found in the vicinity of the cavity trailing end due to the accumulation of coolant coming from the upstream. More coolant leaking from the suction side causes higher cooling effectiveness.

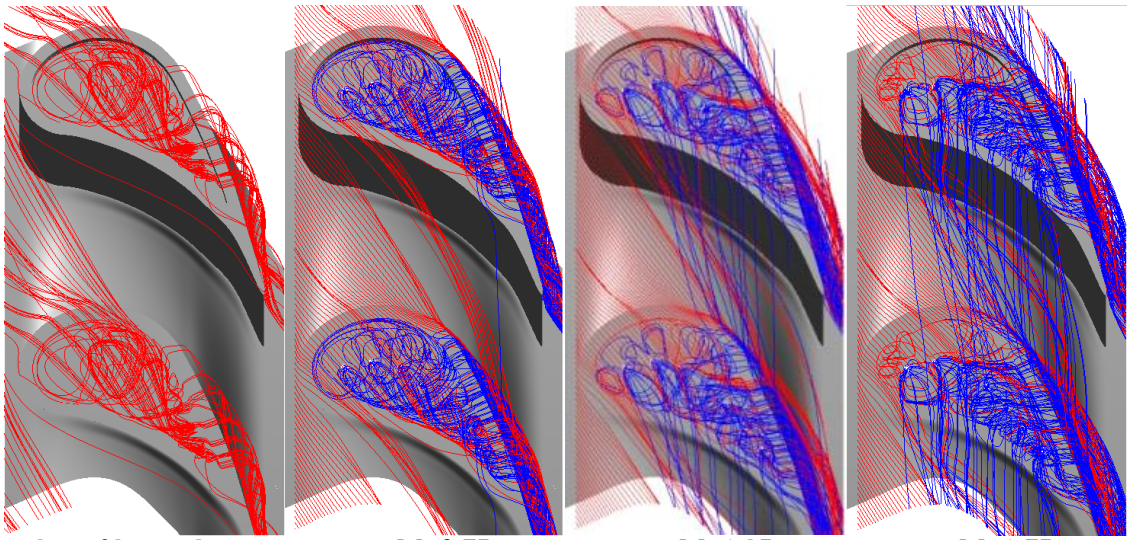

Figure 48: Streamlines based on the relative velocity (CFD results) at 3000 rpm (blue indicates cooling air, red is freestream air) for squealer tip with tip hole cooling [56, 57]

As seen in Figure 48, after crossing over the narrow gap between the casing and the squealer rim, the freestream flow is squeezed in the squealer cavity. Sudden expansion induces flow circulations within the cavity which entraps the freestream particles. Meanwhile, strong interactions between the leakage flow and the cooling jets

intensify the mixing which forms three-dimensional complex vortex systems. Major portion of the mixture of the leakage flow and the coolant continues to roll and travels downstream along the cavity. Eventually, the flow particles accumulate at the trailing end of the cavity and afterward escape from the cavity by crossing over the suction side rim, which generates the suction-side tip vortex. Unlike the case for plane tips, some coolant particles are transported to the leading edge portion by complicated vortices circulating at the surrounding area. Such transportation is able to partially relieve the heat loads and thus provide certain cooling protection to the cavity walls near the leading edge. However, the leading edge of the plane tip is directly exposed to the hot freestream and at risk of overheating. This is an advantage of the squealer tip.

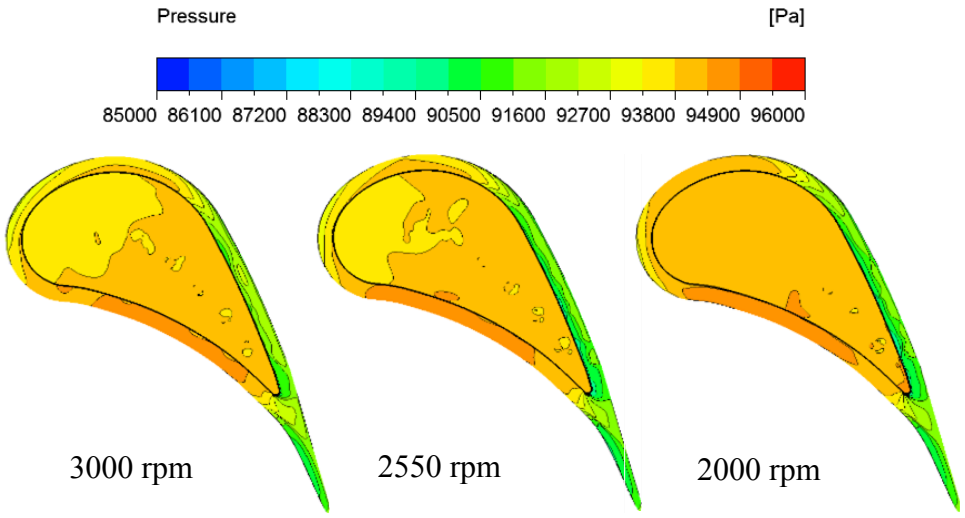

Figure 49: Distribution of the static pressure (CFD results) at squealer tip with tip hole cooling [56, 57]

The pressure on the squealer tip shows dramatically different distributions compared with that on the plane tip. As shown in Figure 49, the most noticeable

characteristic is that the pressure distribution on the cavity floor tends to be uniform and thus the pressure gradient on the cavity floor is significantly decreased. This is resulted from the presence of the large cavity on the tip.

6.1.3. Plane Tip with Pressure-side-edge Compound Angle Hole Cooling

The film cooling effectiveness contour plots for three blowing ratios at the reference rotating condition of 3000 rpm are plotted in Figure 50. The maximum film cooling effectiveness among three cases is about 0.25 with maximum value occurring at pressure side near trailing edge. As blowing ratio increases from M=0.75 to M=1.75, overall film cooling effectiveness increases. This is due to higher mass flow rate of the coolant injected through the holes resulting in a larger film covered area. The film-covered area extends further downstream with a higher maximum value for film-cooling effectiveness as blowing ratio increases.

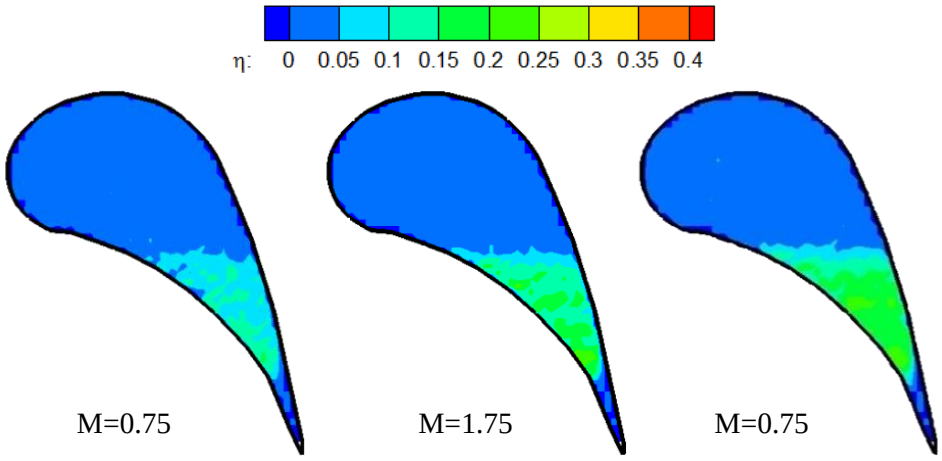

Figure 50: Film cooling effectiveness measured for plane tip with pressure side hole cooling at 3000 rpm

Figure 51 shows streamlines based on the relative velocities near the blade tip. As it is shown, due to high mainstream velocities on pressure side, coolant injected through these pressure side holes can get diverted towards the trailing edge. Thus, effectiveness for the first three holes is almost negligible. Due to the blade geometry and round leading edge, the pressure gradient at the leading edge is not as big as pressure gradient between the pressure side and suction side near trailing edge. Therefore, almost the first 50% of chord length is not covered. As it is shown in Figure 45 (Tip streamlines without cooling) leakage flow almost starts at 50% of chord length. So cooling flow follows the leakage flow in that region and covers that area.

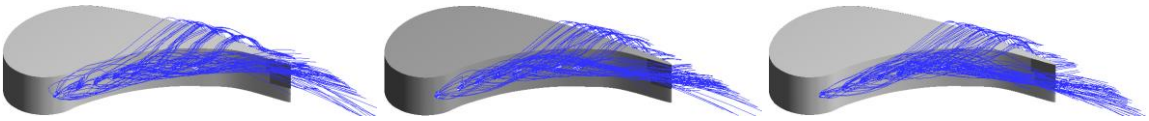

M=0.75, 3000 rpm M=1.25, 3000 rpm M=1.75, 3000 rpm

Figure 51: Streamlines based on the relative velocity (CFD results) at 3000 rpm (blue indicates cooling air) for plane tip with pressure side hole cooling [56, 57]

The relative flow velocity through the gap is dictated by the blade tip rotational speed. Since the dynamic pressure of the relative velocity is much larger than the static pressure difference along the first 50% on the blade tip, the fluid particle within the gap are pushed in the opposite direction of the rotation, thus the major portion of the surface close to the suction side is not covered.

6.1.4. Squealer Tip with Pressure-side-edge Compound Angle Hole Cooling

Figure 52 shows film cooling effectiveness distribution for squealer blade tip with pressure side-edge compound angle hole cooling. The film-covered area for squealer tip is smaller as compared to plane tip. The highest film cooling value among three cases is around 0.25 that occurs at pressure side near trailing edge. Film-cooling effectiveness increases with increasing blowing ratio. Similar to the plane tip with PS cooling, by increasing the coolant mass flow rate, more cooling flow covered the area. For the region from the mid-chord of the blade to the trailing edge on the pressure side rim, the effectiveness is higher. A noticeable trace can be detected on the trailing edge, which is probably due to some carrying over of the coolant over the rim from the pressure side.

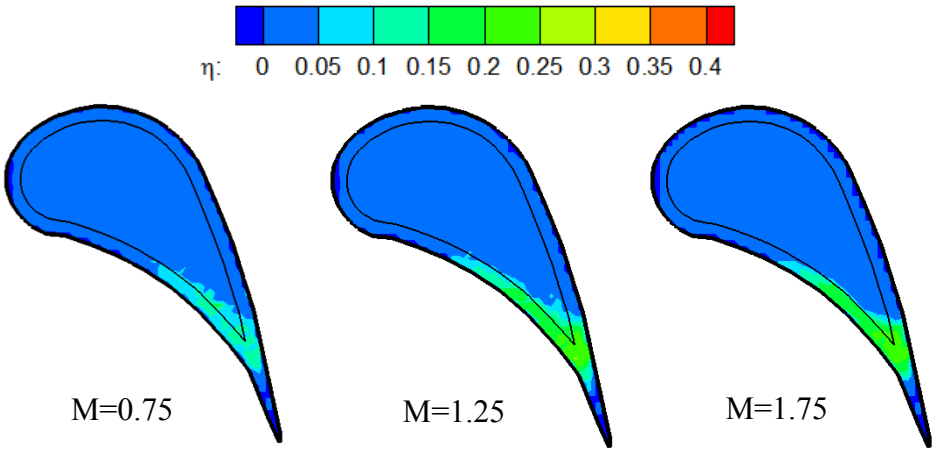

Figure 52: Film cooling effectiveness measured for squealer tip with pressure side hole cooling at 3000 rpm

As it is shown in Figure 53, the presence of a squealer tip reduces the leakage flow from pressure to suction side of the blade. The squealer cavity acts like labyrinth seal and does not allow the leakage flow goes from pressure side to suction side.

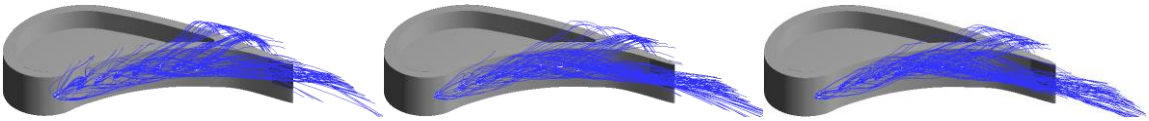

M=0.75, 3000 rpm M=1.25, 3000 rpm M=1.75, 3000 rpm

Figure 53: Streamlines based on the relative velocity (CFD results) at 3000 rpm (blue indicates cooling air) for squealer tip with pressure side hole cooling [56, 57]

6.2. Effect of Rotation Speed Change

In this section effect of rotation for all four configurations is investigated. Film cooling effectiveness data is taken for blowing ration M=1.25 for three different rpm: 3000 rpm, 2550 rpm and 2000 rpm.

At rotational speeds lower than the design speed, the blade flow deflection becomes larger leading to higher specific stage load coefficient, and the stagnation region moves towards the pressure side as the flow incidence angle increases, as sketched in Figure 38. At lower rotating speeds, the stagnation point will further move towards the blade pressure side resulting in a higher pressure zone close to the pressure surface.

6.2.1. Plane Tip with Tip Hole Cooling

Figure 54 shows film cooling effectiveness contour for plane tip with tip hole cooling. As it is shown, more coolant appears to go to the suction side of the blade where the pressure difference across the blade is larger with the lower rotational speed. This phenomenon can be clearly observed from static pressure distribution shown in Figure 46. By decreasing the rpm from 3000 rpm to 2000 rpm, pressure increases at pressure side and decreases at suction side.

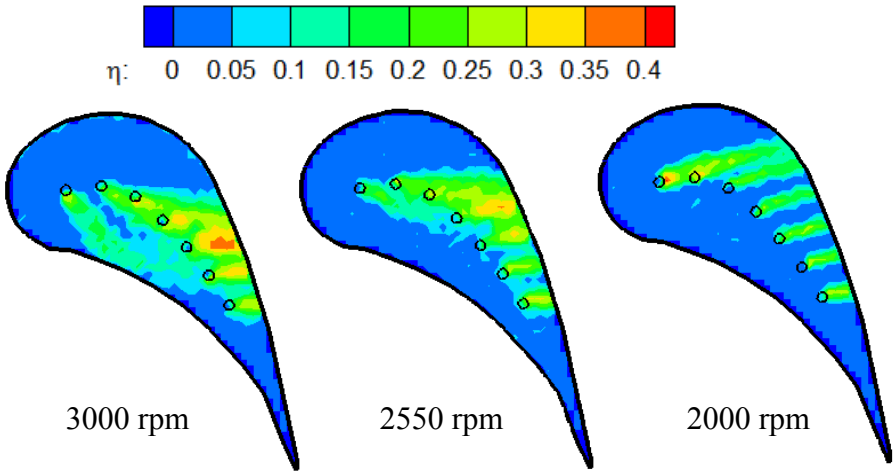

Figure 54: Effect of rotation on film cooling effectiveness measured for M=1.25 for plane tip with tip hole cooling

According to Figure 55, almost all of the cooling jet's streamlines at 2000 rpm follow the leakage flow and go to the suction side. For 2550 rpm, almost all of the cooling jets are deflected towards the suction side, except that a small amount of coolant ejecting from the first cooling hole moves to the pressure side and then leaves the tip gap together with the leakage flow on the pressure side. For 2000 rpm, all of the cooling jets

are deflected towards the suction side. This result is very similar to cascade result shown in [84].

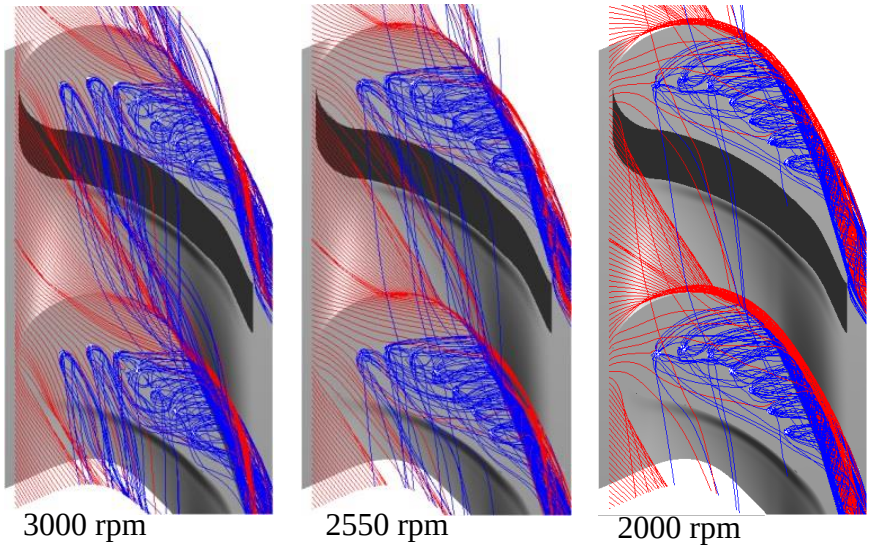

Figure 55: Streamlines based on the relative velocity (CFD results) at different rpm (blue indicates cooling air, red is freestream air)- plane tip with tip hole cooling [56, 57].

6.2.2. Squealer Tip with Tip Hole Cooling

In squealer tip, by decreasing the speed, the effectiveness and film cooling coverage increase. As shown in Figure 56, in 2000 rpm the film cooling effectiveness is almost above 0.15. As shown in Figure 49, by decreasing the rpm flow incidence angle increases and the stagnation region moves towards the pressure side resulting in a higher pressure zone close to the pressure surface. This affects the flow behavior inside the cavity. In 3000 rpm, it is observed that the region between the pressure side and the holes is not covered by the coolant. The coolant flow goes to the suction side after flow

reattachment, so the coolant jets are directed toward the suction side. When the incidence angle changes the flow reattachment location also changes. In the positive incidence angle, the leakage flow is stronger and the flow circulation inside the cavity is enhanced. The coolant is more dispersed in the tip cavity and as a result film cooling effectiveness increases over the cavity floor. In 2000 rpm, coolant gets accumulated inside the squealer cavity in the region between the mid-chord and the trailing edge due to flow recirculation in the contracting squealer passage. Figure 57 shows Streamlines based on the relative velocity (CFD results) at different rpm for squealer tip with tip hole cooling.

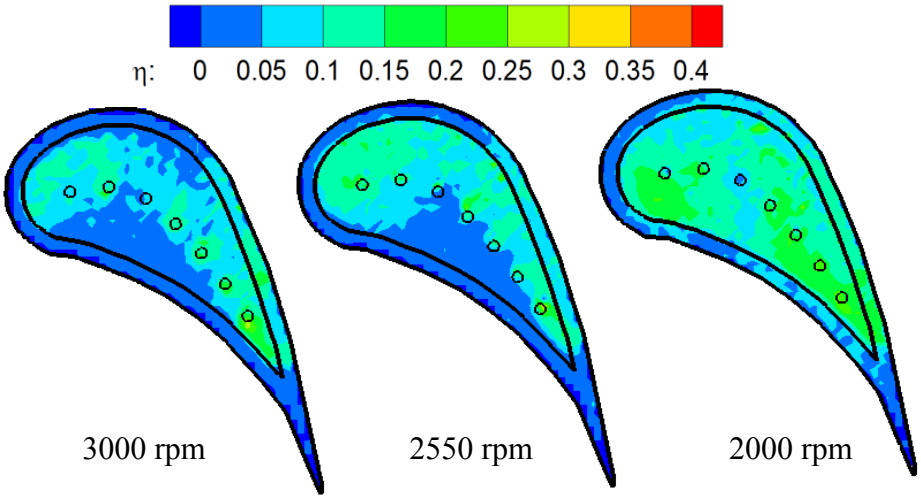

Figure 56: Effect of rotation on film cooling effectiveness measured for M=1.25 for squealer tip with tip hole cooling

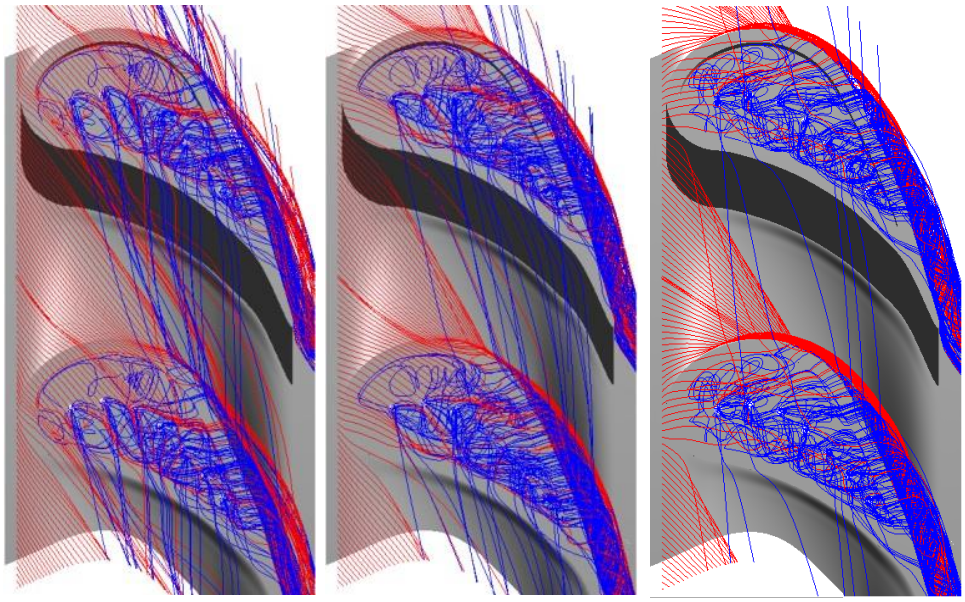

Figure 57: Streamlines based on the relative velocity (CFD results) at different rpm (blue indicates cooling air, red is freestream air) - squealer tip with tip hole cooling [56, 57]

6.2.3. Plane Tip with Pressure-Side-Edge Compound Angle Hole Cooling

Similar trend like squealer tip is obtained when it comes to plane tip with pressure side-edge cooling. As shown in Figure 58, more area of the tip surface is protected by coolant flow by decreasing rotational speed. Figure 59 shows the pressure distribution on pressure side and tip surface. As it is shown, stagnation point moves toward pressure side and it is close to first hole. Higher pressure on pressure side increases the leakage flow to suction side. Figure 60 depicts the streamline at plane tip with pressure side cooling. In 2000 rpm, compared to 3000 rpm, less flow is diverted towards leakage flow and followed main-stream velocity inside the passage between

blades. The highest value of nearly 0.4 is obtained at 2000 rpm near trailing edge due to accumulation of coolant.

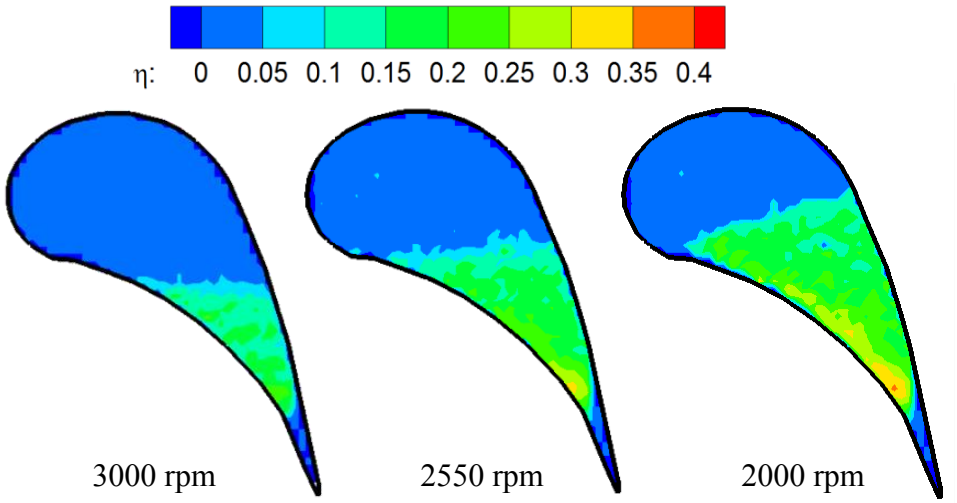

Figure 58: Effect of rotation on film cooling effectiveness measured for M=1.25 for plane tip with PS hole cooling

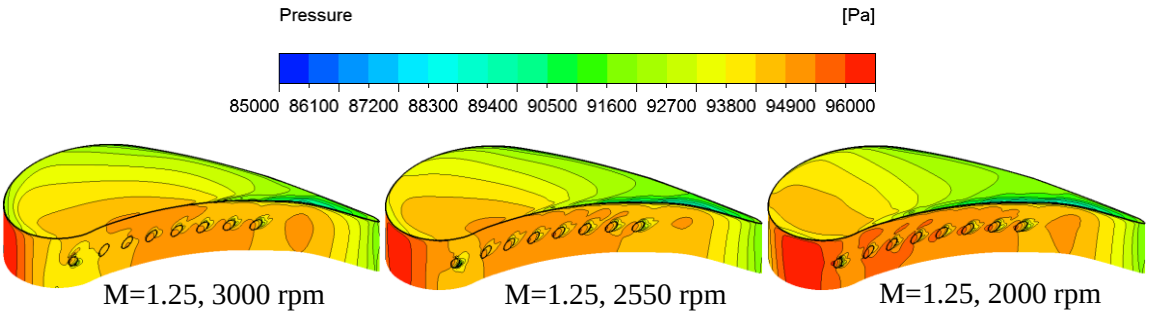

Figure 59: Distribution of the static pressure (CFD results) at plane tip with PS hole cooling [56, 57]

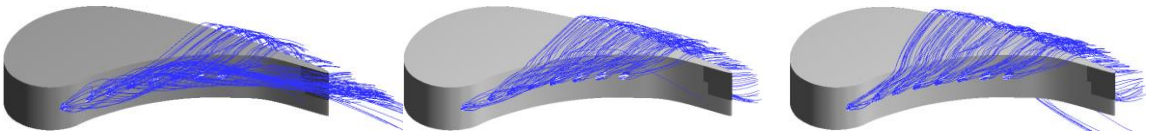

M=1.25, 3000 rpm M=1.25, 2550 rpm M=1.25, 2000 rpm

Figure 60: Streamlines based on the relative velocity (CFD results) at different rpm (blue indicates cooling air) - plane tip with PS hole cooling [56, 57]

6.2.4. Squealer Tip with Pressure-side-edge Compound Angle Hole Cooling

In squealer tip with pressure side cooling less leakage flow goes from pressure side to suction side due to existence of cavity. By decreasing the rpm, incidence angle increases, and also pressure increases on pressure side (Figure 61). This increase enhances the film cooling effectiveness on pressure side rim. The highest film cooling value among three rpms is around 0.35 that occurs at pressure side near trailing edge at 2000 rpm (Figure 62). At 2000 rpm and 2550 rpm some coolant streamlines cover some area on suction side rim. As it is shown in Figure 63 some coolant streamlines reattach the cavity floor at 2000 rpm and covered small area there.

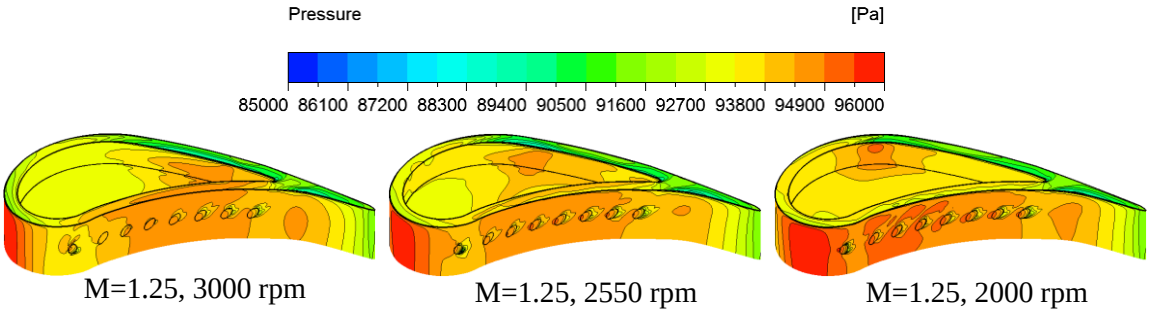

M=1.25, 3000 rpm M=1.25, 2550 rpm M=1.25, 2000 rpm

Figure 61: Distribution of the static pressure (CFD results) at squealer tip with PS hole cooling [56, 57]

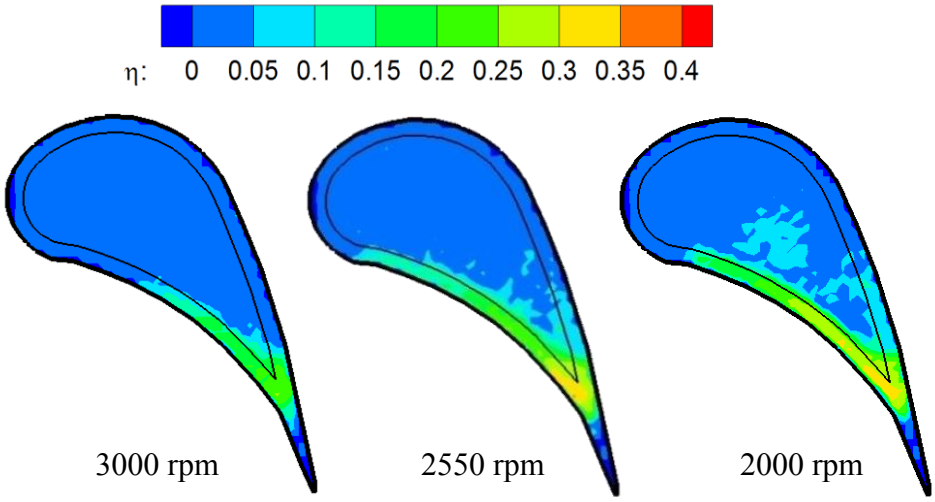

Figure 62: Effect of rotation on film cooling effectiveness measured for M=1.25 for squealer tip with PS hole cooling

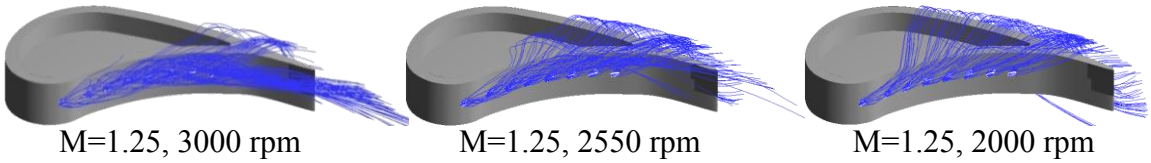

Figure 63: Streamlines based on the relative velocity (CFD results) at different rpm (blue indicates cooling air) - squealer tip with PS hole cooling [56, 57]

6.3. Comparison of Computational and Experimental Results

Figure 64 shows the comparison of computational and experimental results for different configurations. Steady-state CFD was able to predict the coolant trace. The area covered by film cooling is almost identical with experimental results. It shows that Steady-state CFD can predict the flow behavior at tip of the blade well.

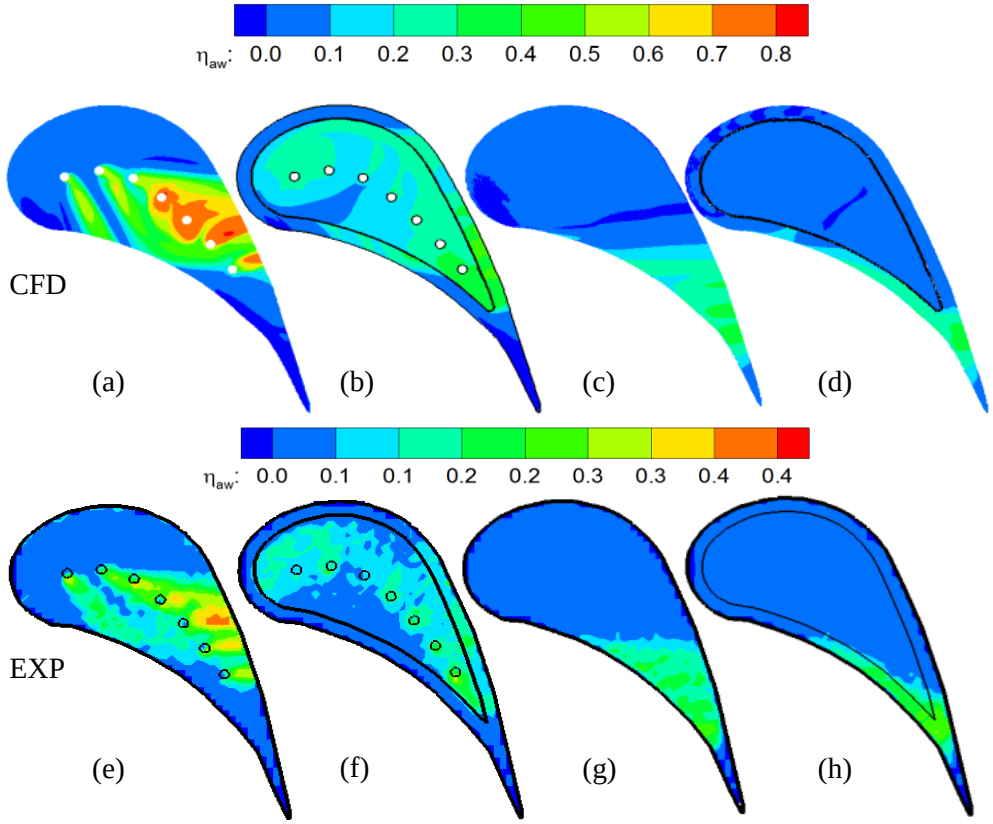

Figure 64: Comparison of CFD results (top row) and experimental results (bottom row) at 3000 rpm, M=1.25. (a, e) plane tip with tip hole cooling, (b, f) squealer tip with tip hole cooling, (c, g) plane tip with PS hole cooling and (d, h) squealer tip with PS hole cooling [56, 57]

The only problem is that Steady-state CFD over predicts the film cooling effectiveness by almost 90%. The reason is primarily attributed to a gap between the Steady-state CFD models and physical facts. For instance, the stator wakes, upstream turbulence intensity, rotor-stator interactions and so on can probably reduce the film cooling effectiveness. However these substantial characteristics have been eliminated by the mixing plane interface between stator and rotor. Importantly, inherent deficiency of the turbulence models in predicting very close-to-wall heat transfer and lacking of

proper boundary layer transition models essentially create the difficulty for CFD software in quantitative prediction. Therefore researchers often use CFD tool as a helpful assistant to attain some details which are difficult to measure in order to draw more complete pictures of the research objects. Using transient CFD to predict the film cooling effectiveness at blade tip is the subject of an ongoing research at TPFL.

6.4. Pitch-wise Average Film Cooling Effectiveness

The film cooling effectiveness results were averaged along the pitch-wise direction and the averaged data for all blowing ratios and rotational speeds are presented in Figure 65 along the axial chord.

In plane tip, it is shown that the coverage of the film cooling starts from nearly 15% C_{ax} and ends at 90% C_{ax}. For M=0.75, the averaged value seems to gradually increase along the C_{ax} within the covered area. Several peaks are observed and each of them represents the location of every film cooling hole. At M=1.25, the averaged film cooling effectiveness is slightly lower than 0.1 from 20% C_{ax} to 60% C_{ax}. However, the averaged value dramatically increases when it reaches 65% C_{ax}. Between 65% C_{ax} and 80% C_{ax}, the averaged film cooling effectiveness is as high as 0.18. Even higher film cooling effectiveness is obtained when the blowing ratio reaches M=1.75.

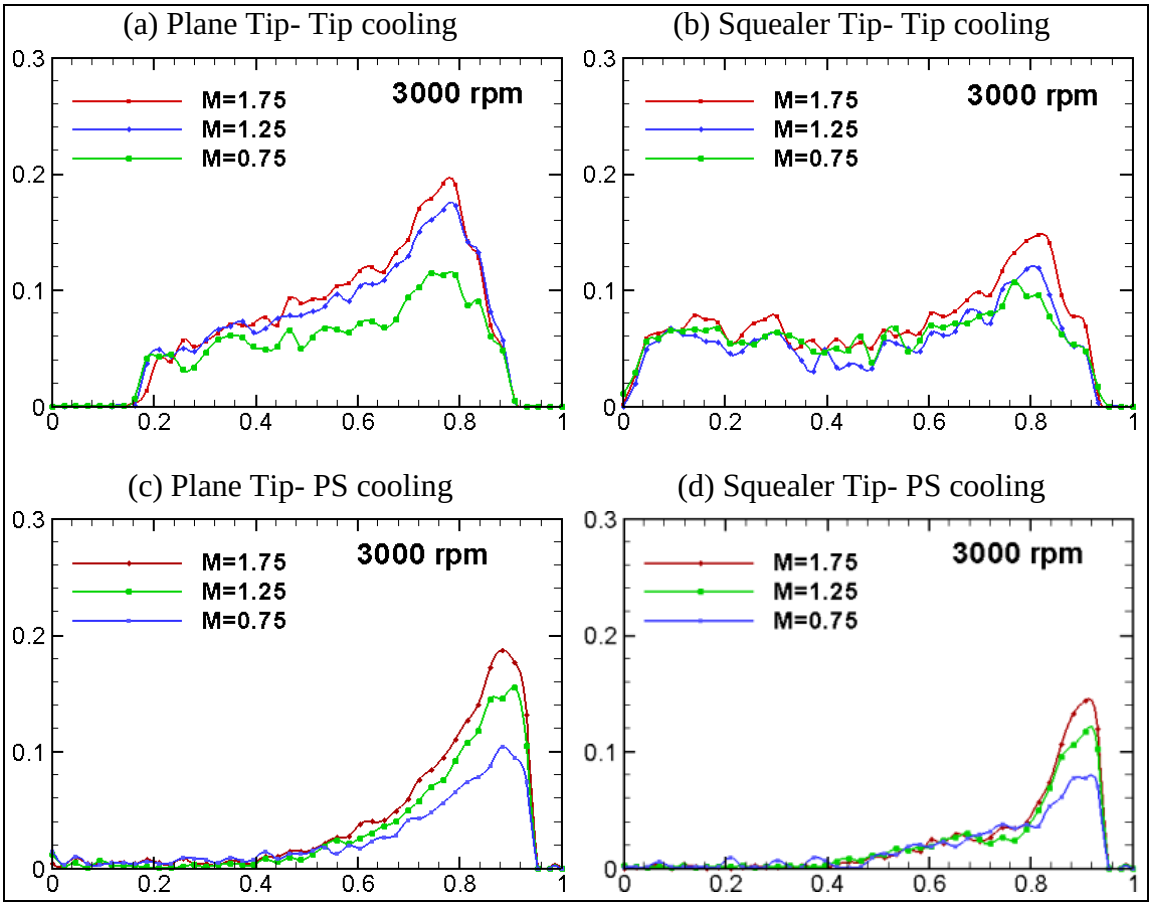

Figure 65: Pitch-wise average film cooling effectiveness measured for four different configurations - different blowing ratio at 3000 rpm

The squealer tip shows quite different trends in Figure 65(b). The film cooling is effective up to 90% C_{ax} for all the blowing ratios. For M=0.75, the pitchwise-averaged film cooling effectiveness is stabilized around 0.06 until it bumps up a bit at 80% C_{ax}. However, the averaged cooling effectiveness gradually grows 0.12 when the blowing ratio becomes 1.25. A similar trend is obtained for the blowing ratio M=1.75, but the average slope is slightly larger compared with M=1.25. The highest value of 0.15 appears at about 80% C_{ax} where it is believed to be close to the cavity trailing end. In

fact, the peak value is found in the same area for all three blowing ratios. As discussed earlier the impact of the blowing ratio on the cooling effectiveness might be less important for the squealer tip. Within 40% C_{ax} and 80% C_{ax}, the plane tip offers higher averaged cooling effectiveness than the squealer tip does.

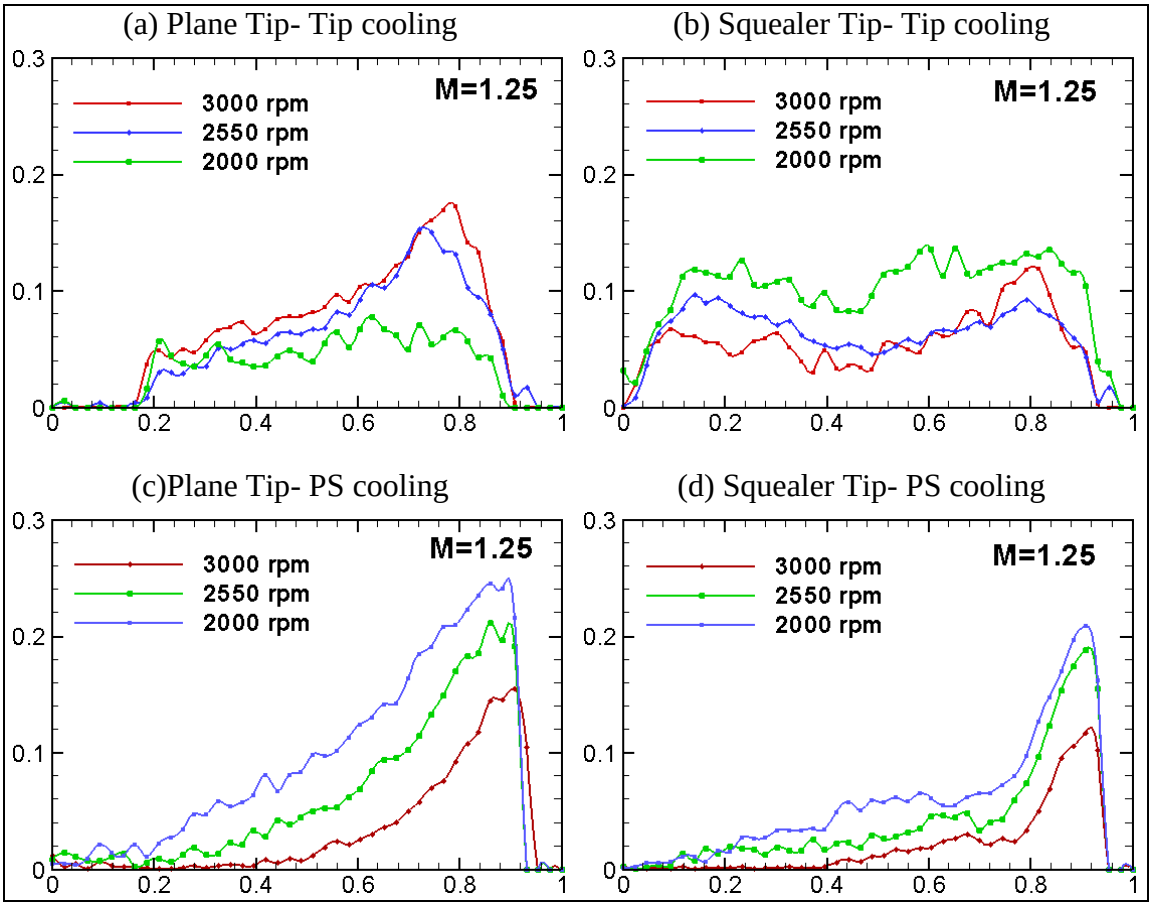

Figure 66: Pitch-wise average film cooling effectiveness measured for four different configurations - different rpm at M=1.25

The impact of the rotational speed on the film cooling effectiveness is also illustrated in Figure 66. It shows the pitch-wise averaged film cooling effectiveness

results plotted for M=1.25. The impact of turbine rotational speeds on film cooling effectiveness can be clearly perceived from these plots.

In plane tip, as rpm increases, the effectiveness magnitudes increase for the same mass flow ratio. On the other hand, the squealer tip shows completely different trends. As shown in Figure 66 in 2000 rpm from C_{ax} 10% to 90% the average film cooling effectiveness is almost higher than 0.1 while average film cooling in 2550 rpm and 3000 rpm are less than 0.1 almost along axial chord.

In plane tip with pressure side cooling, the coverage of film cooling starts from 50% C_{ax} at 3000 rpm (Figure 65(c)). The averaged film cooling increases gradually along the C_{ax} within the covered area. By increasing the blowing ratio to 1.75, higher film cooling effectiveness is obtained.

As rpm decreases to 2000 rpm, film cooling effectiveness coverage starts earlier. For example, at 2550 rpm it starts at 30% C_{ax} and at 3000 rpm it starts at 20% C_{ax}. The highest averaged film cooling effectiveness among all the cases in Figure 66(c) appears at 2000 rpm at 85%.

Squealer tip with pressure side cooling has the same trends as plane tip with pressure side cooling. For all blowing ratios, from 50% C_{ax} to 80% C_{ax} averaged film cooling effectiveness increases slightly due to pressure side rim effectiveness. The highest value of 0.15 appears at about 90% C_{ax} where it is close to the cavity trailing end. The peak value is found in the same area for all three blowing ratios.

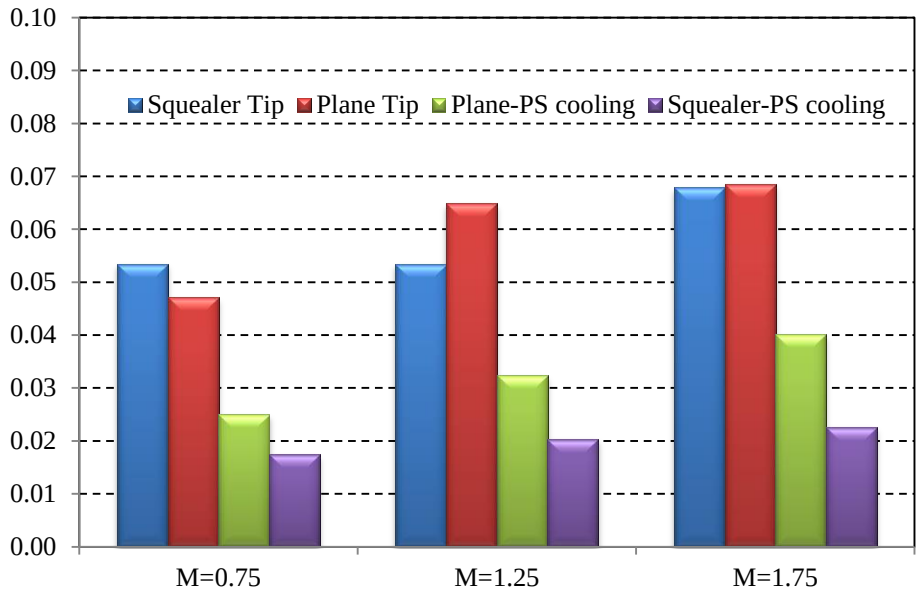

Figure 67. Area-averaged film cooling effectiveness versus blowing ratio at the blade tip region

The area-averaged film cooling effectiveness versus the blowing ratio at the blade tip region is shown in Figure 67. It is shown that the overall film cooling effectiveness for plane tip increases monotonically as the blowing ratio is increased. This is consistent with the contour plots in Figure 47. Note that the overall effectiveness on the plane tip is slightly lower than that on the squealer tip for M=0.75. With increasing blowing ratios, the situation is altered. Higher overall effectiveness is obtained on the plane tip for both M=1.25 and 1.75.

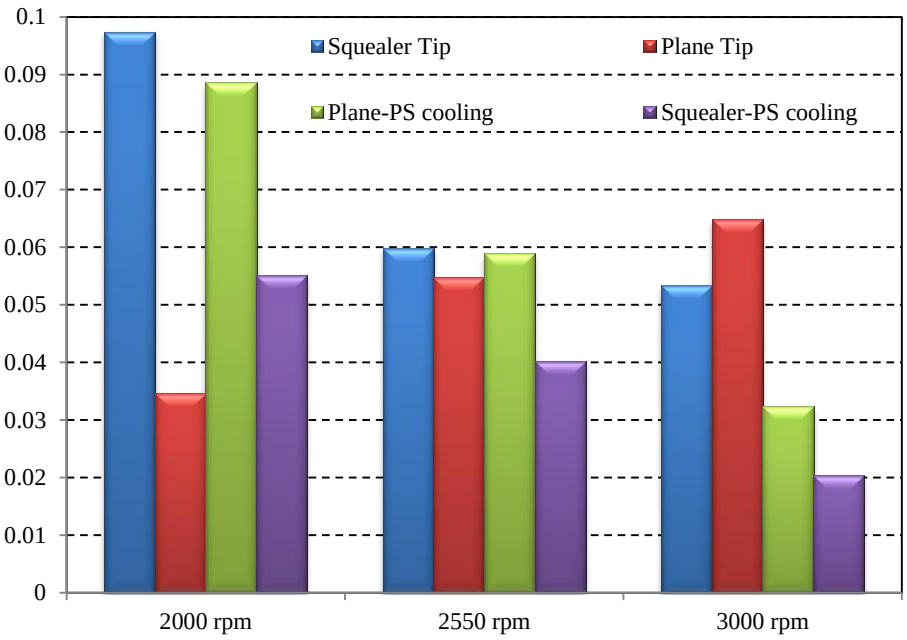

Figure 68. Area-averaged film cooling effectiveness versus rotational speed at the blade tip region at M=1.25

The area-averaged film cooling effectiveness versus rotational speed at the blade tip region is shown in Figure 68. Squealer tip at 2000 rpm has the highest value among all the cases. For all the configurations except the plane tip by increasing the rpm, the area averaged film cooling effectiveness decreases. According to Figure 47 and Figure 48, for the plane tip at 3000 rpm all the coolant particles exiting from the first and second cooling holes travel across the pressure side and form a passage flow by mixing with the mainstream. Therefore, coolant covers more of the tip, which is virtually the result of the impact of both the pressure difference and the relative motion between the tip and shroud.

As it is mentioned earlier, the objective of the dissertation is to experimentally investigate the film cooling effectiveness for different turbine blade tip configurations. Of course in real design heat transfer coefficients, cooling flow penalties and stage losses should be considered.

7. AERODYNAMIC FLOW MEASUREMENT

Endwall Secondary flow losses and vortices play a significant role in reduction of stage efficiency in high pressure (HP) turbines. As explained in section 1, endwall contouring is one of the ways to reduce endwall secondary flows. Recent studies [85-87] depicted how flow modified at the stage exit by upstream secondary vortices. Hodson et al. [85] investigated the interactions of incoming wakes and secondary flow vortices in a single stage axial turbine. Results showed that stator secondary flows have small effect on rotor secondary flows. Three dimensional flowfield inside the rotor passage forced these effects to be appeared toward the midspan. Chaluvadi et al. continued the work for understanding the blade row interaction by using smoke flow visualization and five hole probes in a single stage high pressure turbine. Figure 69 shows a simple model of vortex transport from the stator passage through the rotor passage. Downstream blade row cuts the stator hub passage vortex in a pretty similar way to the wake. As a result, the bowed vortex seems to have two counter rotating legs: suction side leg (vortex 3) and pressure side leg (vortex 4) as shown in Figure 69. Chaluvadi et al. [86] explained "At the hub the kinematic interaction between the stator and the rotor passage vortices has two effects. First, the suction side leg of the stator passage vortex is displaced radially upward over the developing rotor hub passage vortex. Additionally, the pressure side leg of the stator passage vortex is entrained into the rotor passage vortex. Similar phenomena were observed at the tip of the rotor blade row."

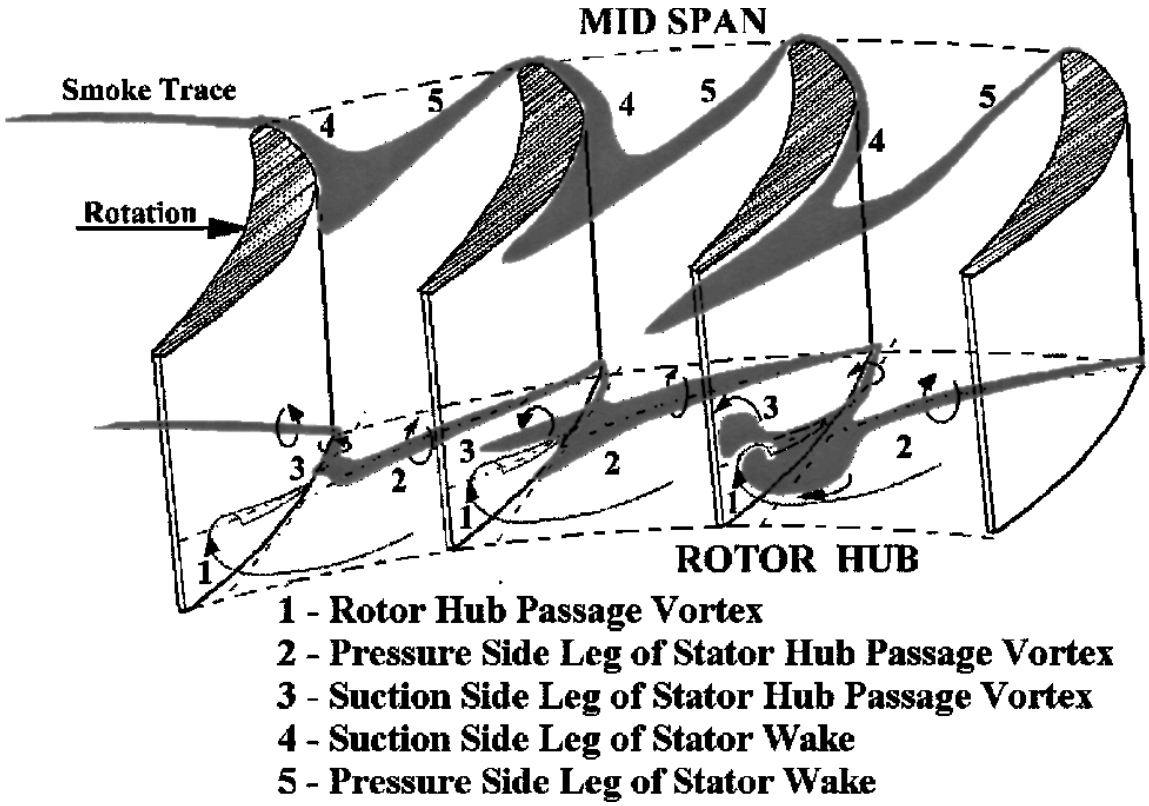

Figure 69: simple blade vortex transport model by [86]

Pullan [87] studied the secondary flows and blade row interaction in a low speed research turbine facility. Some vortical structures were seen in the rotor passage caused by stator exit flow field. Unsteady numerical simulation was also performed to understand the formation of these vortices.

Porreca et al. [88] used PIV and fast response aerodynamic probes to measure steady and unsteady pressure and velocity fields. They found that vortex stretching and wake bending due to the flow interaction with stator are primary source of losses and unsteadiness in the rotor. Porreca et al. [89] in another paper investigated the fluid

dynamics and performance of shrouded blades in axial turbines. Behr et al. [90] studied the effect of stator and rotor clocking in HP turbines.

Gaetani et al. [91] experimentally investigated the effect of stator secondary flows on rotor flow field. Two different axial gaps between stator and rotor were studied and compared. The rotor flowfield and interaction with stator vortices and wakes were explained. Persico et al. [92, 93] continued the work and performed parametric study of the blade row interaction. Results showed increase in the magnitude of the rotor inlet vortices change the structure of flow field in the rotor significantly. ANSYS-CFX were also used to evaluate the three dimensional unsteady aerodynamics of a low aspect ratio turbines.

In this section results of comprehensive performance measurements and interstage traversing at different rotational speeds and mass flow rates are presented.

7.1. Interstage Results

Interstage traversing was performed at rotational speeds of 2000 rpm, 2400 rpm and 3000 rpm. Turbine cross sections showing all stations and placed of T-rings are presented in Figure 70. As discussed in section 3, three five-hole probes are mounted on three traversing systems with a decoder and encoder for accurate probe positioning. Figure 71 shows the Angular position of the five-hole probes at stations 3, 4, and 5.

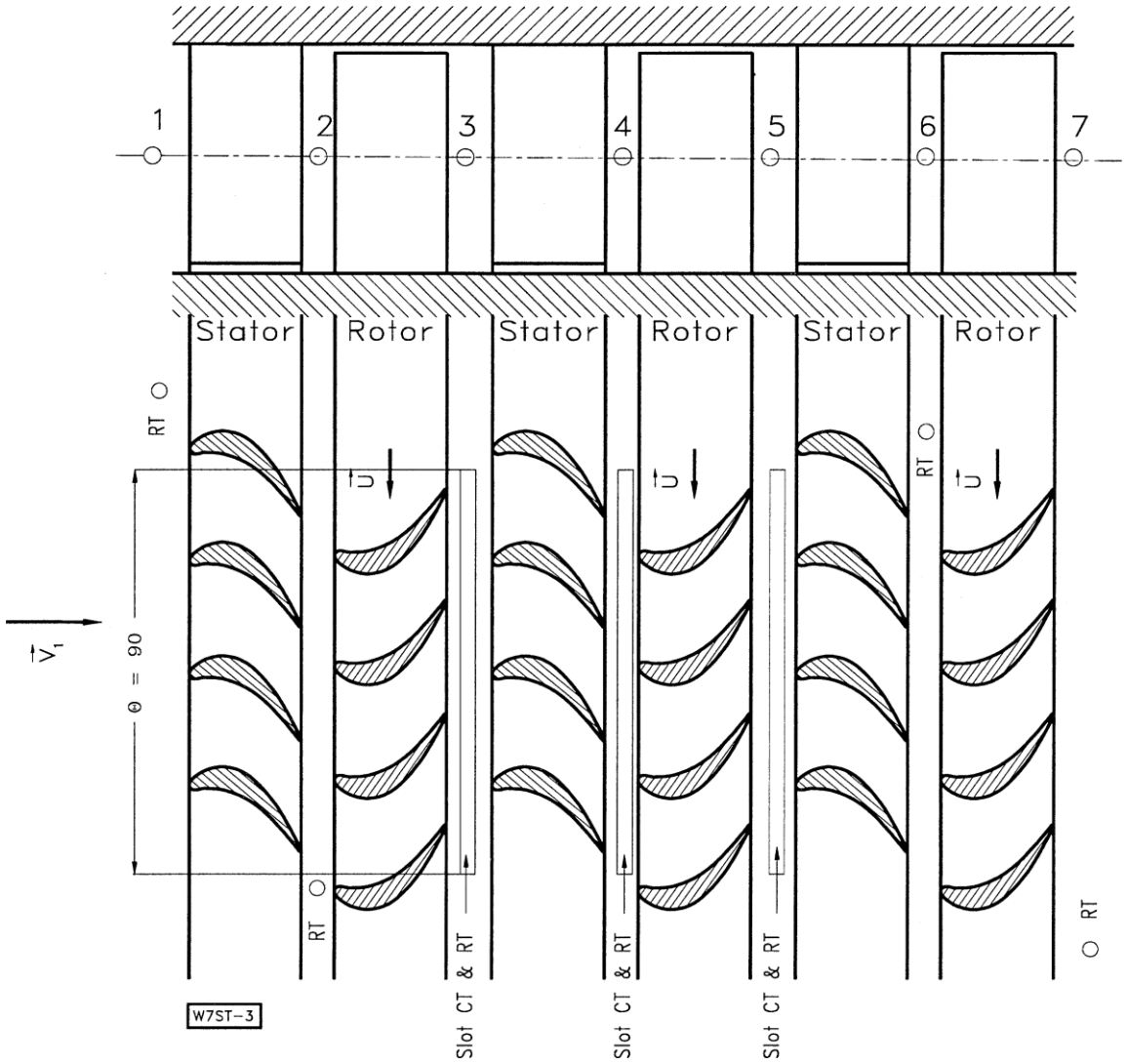

Figure 70: Turbine cross section (Schobeiri et al. [53] and [54])

Results for 3000 rpm are presented in this section. Results for 2000 rpm and 2400 rpm are presented in appendix A.

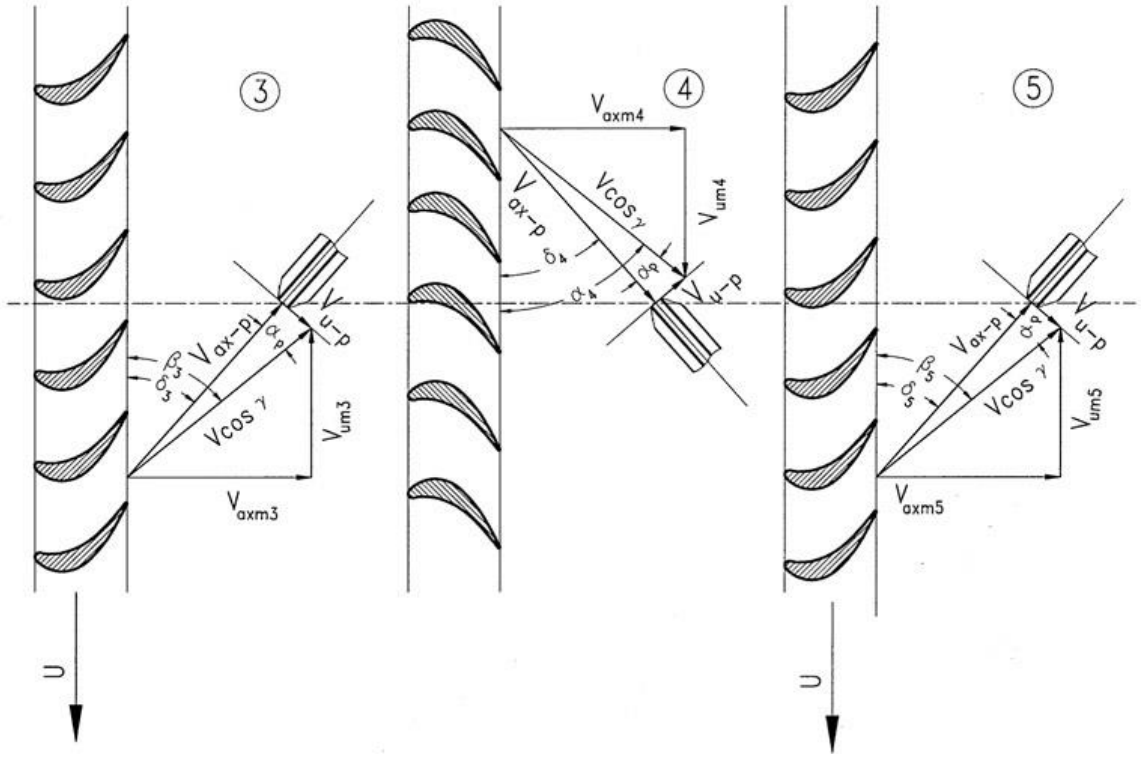

Figure 71: Angular position of the five-hole probes at station 3, 4, and 5 [54]

7.1.1. Contour plots

Figure 72 presents a general overview of the main flow features in terms of contour lines on the station 3 after rotor blades as measured by five-hole probe in the rotor. Absolute flow angle, relative flow angle, relative total pressure, total pressure, meridian flow angle and Mach number are shown in this figure.

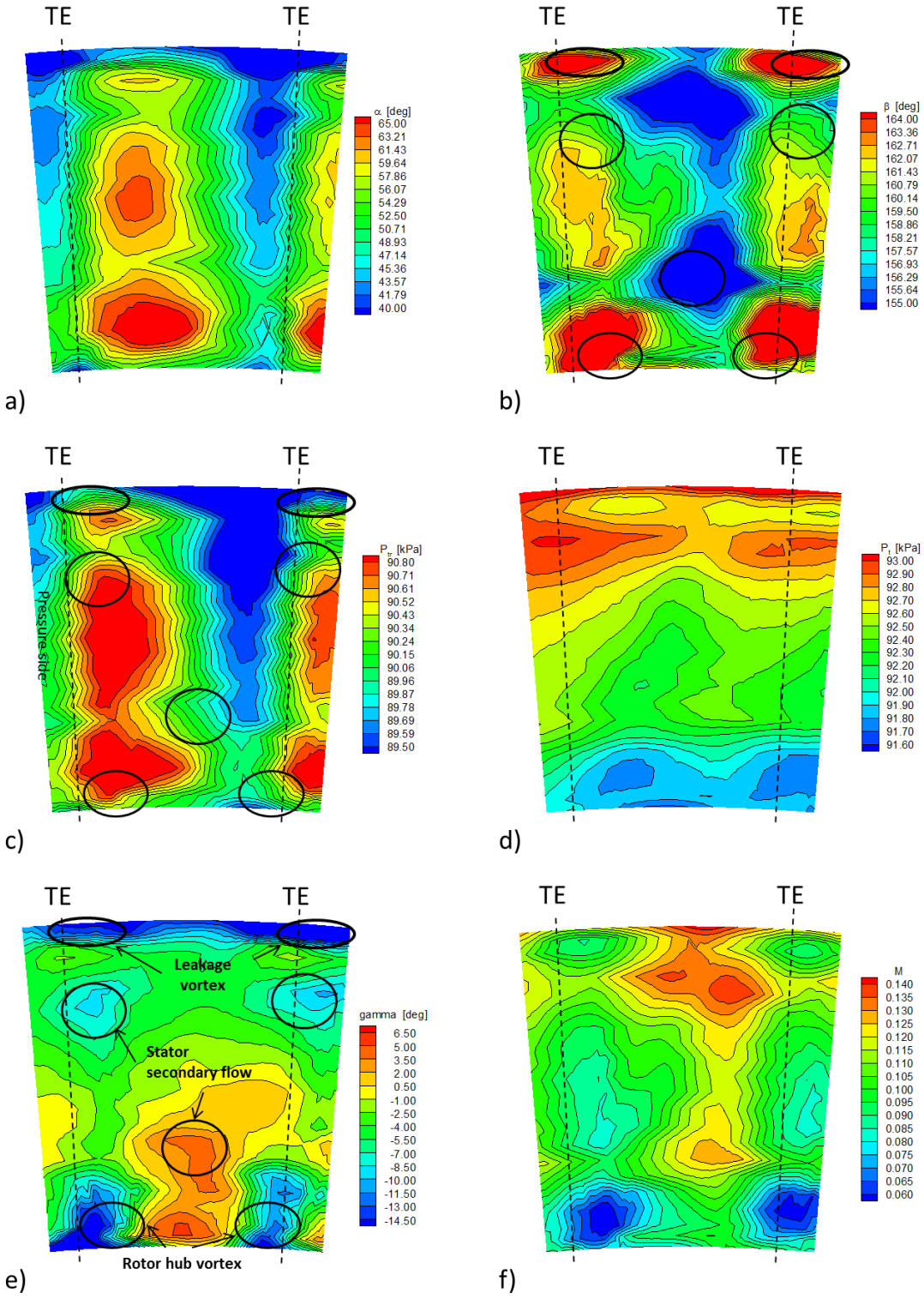

Figure 72: Contour plots of rotor exit flow ($\alpha, \beta, P_{tr}, P_t, \gamma$ and M) at station 3

According to meridian flow angle contour in Figure 72(e) almost 40% of the span (from 25–65%) is filled by essentially 2D flow. Close to the hub area, high meridian angle represents high vortical flow due to secondary flows. Similar behavior is depicted in relative total pressure contour in which relative total pressure has some sudden changes in magnitude in those regions.

Also a pretty large hub passage vortex centered at 20% of span can be seen covering up to 15% of the span. As shown in Figure 69, the interaction between the stator and the rotor passage vortices caused the suction side leg of the stator passage vortex moved radially upwards over the rotor hub passage vortex. Moreover, the rotor passage vortex swept over the pressure side leg of the stator passage vortex.

At the tip there is a region with vortical flows that covers almost 10% of the span and it centered at 95% span. It can be concluded that secondary flows and high vortical flows are caused by tip leakage flow. Another vortical structure region is placed at 80% span. This structure could be originated by either the rotor secondary flow or the interaction between stator and rotor casing secondary flow. This structure seems to be slightly weaker than tip leakage flow.

Similar to the hub stator passage vortex, this vortical structure is caused by the interaction between the tip leakage and stator casing vortex. This interaction moved the stator casing vortex toward the midspan on the suction surface.

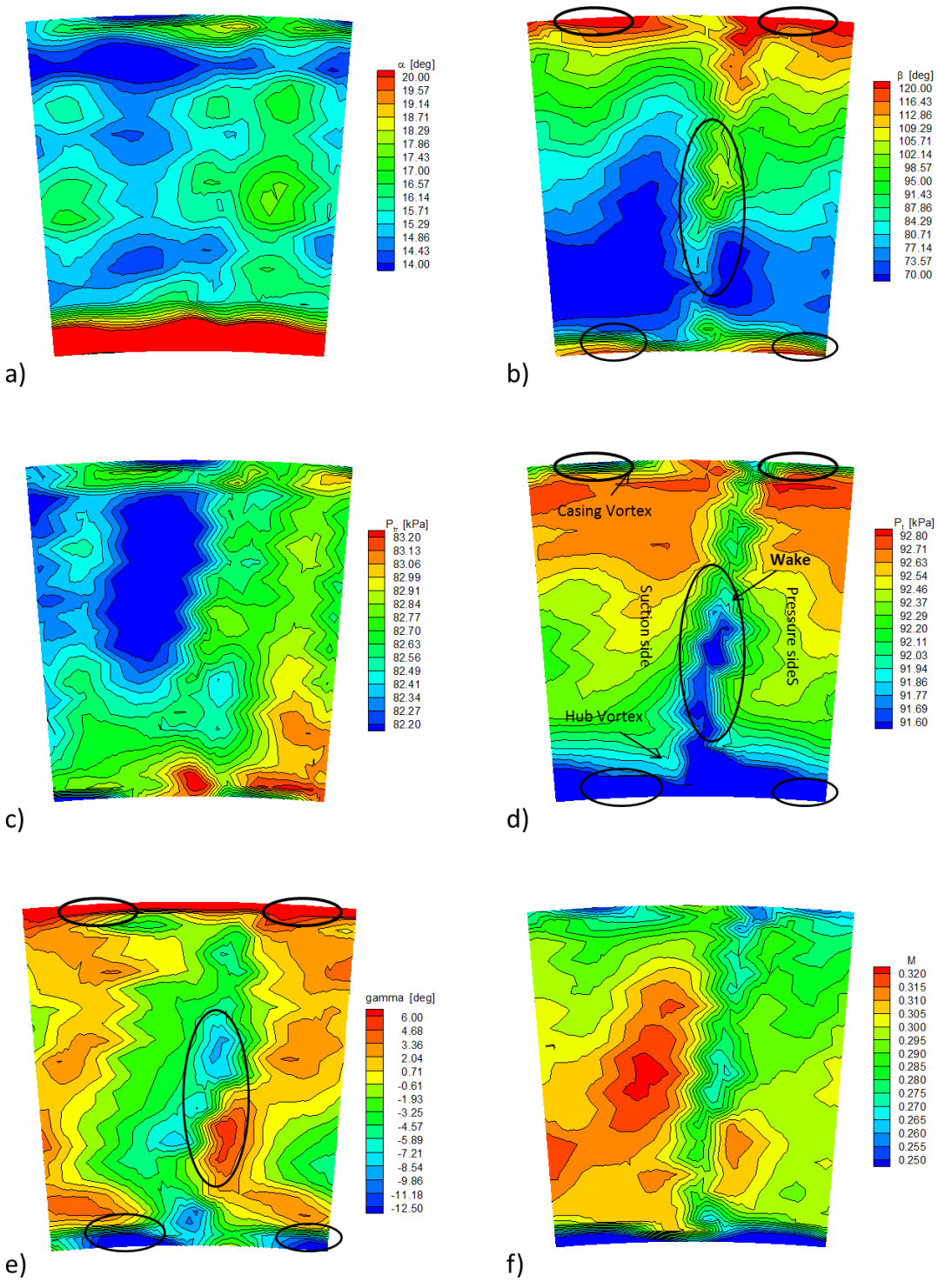

Figure 73: Contour plots of stator exit flow $\alpha, \beta, P_{tr}, P_t, \gamma$ and M at station 4

Figure 73 shows a general overview of the main flow features in terms of contour lines on the station 4 after stator blades. Absolute flow angle, relative flow angle, relative total pressure, total pressure, meridian flow angle and Mach number are presented in this figure.

The region in the middle of the plot in the total pressure contour plot Figure 73(d) is the stator wake. This region can be identified in meridian angle plot (Figure 73(e)) and relative flow angle plot (Figure 73(b)). Based on meridian angle plot, 75% of the span is almost two-dimensional flow. The Blade wake is the main reason for the loss in this region.

Stronger losses happen close to the hub and tip. Meridian angle has sudden change near the hub and tip due to endwall secondary flows. It seems secondary flows near casing (blade tip) is more diffused compare to the hub endwall. According to [85] this difference is due to the effects of the spanwise pressure gradients within the stator passage.

Figure 74 depicts a general overview of the main flow features in terms of contour lines on the station 5 after rotor blades. Absolute flow angle, relative flow angle, relative total pressure, total pressure, meridian flow angle and Mach number are shown in this figure. In general flow behavior is almost identical to station 3.

Similar to the contour plots at station 3, stator hub and casing passage vortex can be seen in this figure. Stator hub passage vortex is centered at 35% and stator casing vortex is located at 75% of span.

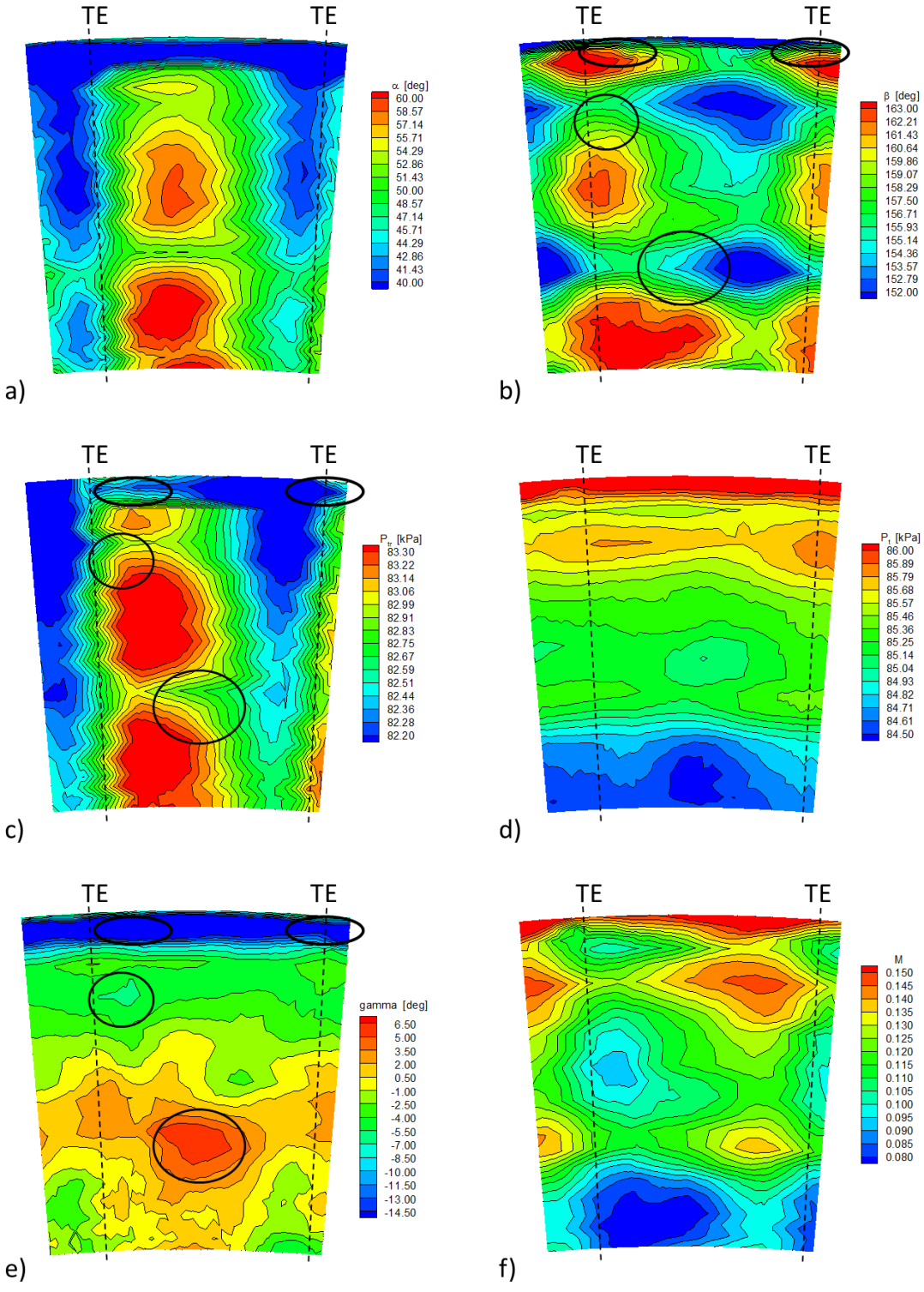

Figure 74: Contour plots of rotor exit flow $\alpha, \beta, P_{tr}, P_t, \gamma$ and M at station 5

The only difference between station 3 and station 5 is that hub secondary flows in station 5 are very limited and weaker compared to station 3. Second rotor has a contoured endwall and station 5 is right after the contouring. This is the consequence of the endwall contouring that has reduced the pressure difference between the pressure and suction surface leading to lower secondary flow vortices.

7.1.2. Radial Pitchwise Averaged Distribution

In this section radial distribution of pitchwise averaged of flow parameters as a function of the immersion ratio $R = \frac{r - r_{hub}}{r_{tip} - r_{hub}}$ are presented at 3000 rpm.

Figure 75 depicts the radial distribution of pitchwise average absolute flow angle. Some irregularities can be seen for all stations close to the tip start at 85% span. These regions are affected by tip leakage vortices and casing secondary flows which explained in previous section.

At station 3 and 4, areas near hub undergo strong changes in flow angles due to hub secondary flow vortices. These areas can be seen up to 20% of span. On the other hand, station 5 shows smooth flow angle distribution near hub which is due to endwall contouring that reduced the hub secondary flows in that region. The immersion ratio range between R = 0.3 to 0.7 shows a moderate change in the range of 5°.

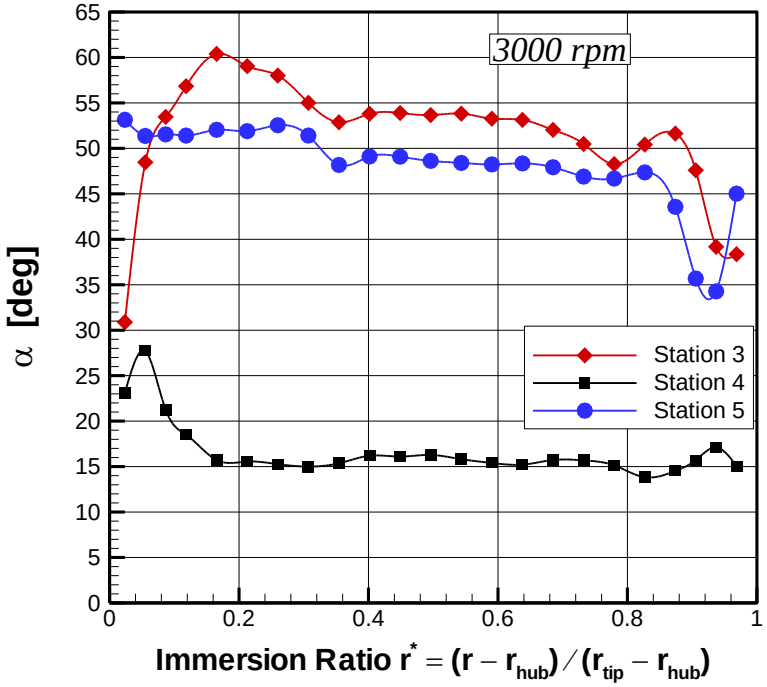

Figure 75: Radial pitchwise averaged distribution of the absolute flow angle

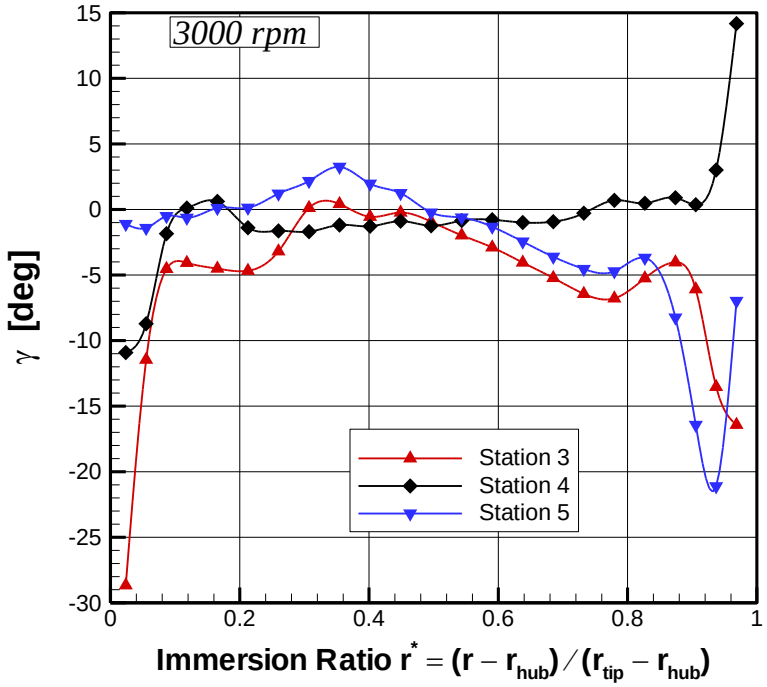

Figure 76: Radial pitchwise averaged distribution of meridian angle

Figure 76 shows radial pitchwise averaged distribution of meridian angle. Station 4 has moderate change in immersion ratio between 0.15 and 0.85. It can be concluded that flow is two dimensional in this region. Station 3 shows more changes near hub and tip. Almost 40% of span in the area between R=0.25 to R=0.65 is two dimensional and the rest is affected by hub secondary flow vortices and tip leakage vortices. Interestingly station 5 doesn't show any strong changes near hub compare to other stations. This is the result of the contoured endwall which reduced the secondary flow vortices. Station 5 similar to station 3 shows a strong changes near tip from R= 0.8 to R=1.

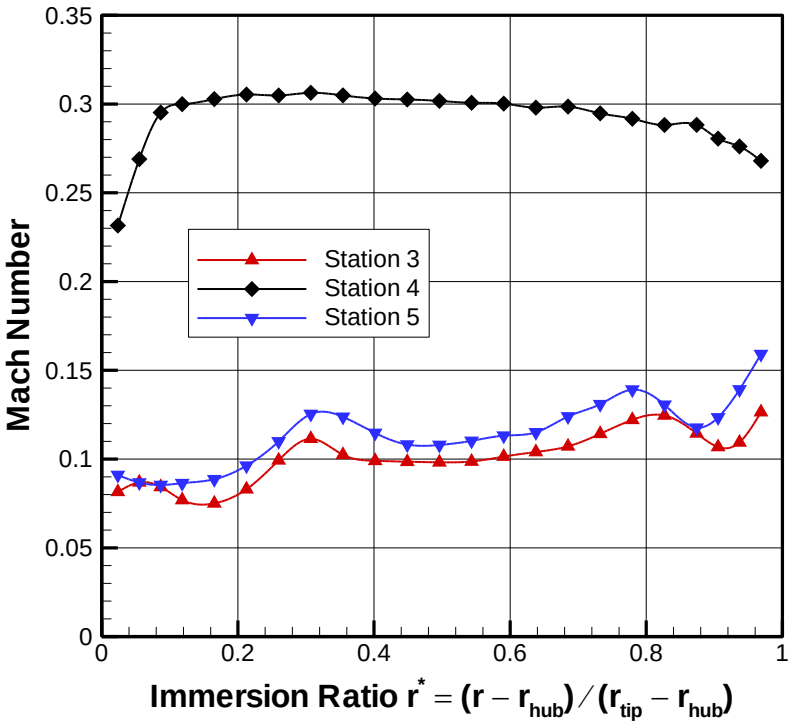

Figure 77: Radial pitchwise averaged distribution of the absolute Mach number at 3000 rpm

Absolute Mach numbers as function of immersion ratios are shown in Figure 77. Uniform low sub subsonic absolute Mach numbers around 0.1 are encountered downstream of the first and second rotor, stations 3 and 5, whereas the second stator exit Mach number, at station 4, is around 0.3. That's why five hole probes were calibrated based on Mach number 0.1 and 0.3.

Figure 78 shows radial pitchwise averaged distribution of relative velocity at 3000 rpm. Major changes near hub and tip can be seen due to secondary flows and tip leakage vortices. Considering the flow angles, Figure 79 exhibits the distribution of the axial velocity component, which is responsible for mass flow distribution in the spanwise direction.

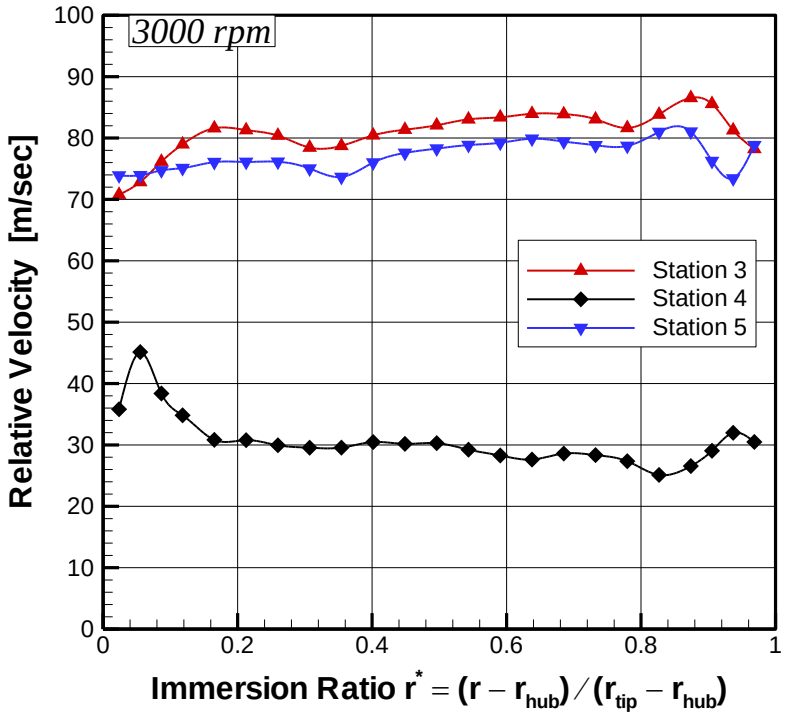

Figure 78: Radial pitchwise averaged distribution of the relative velocity

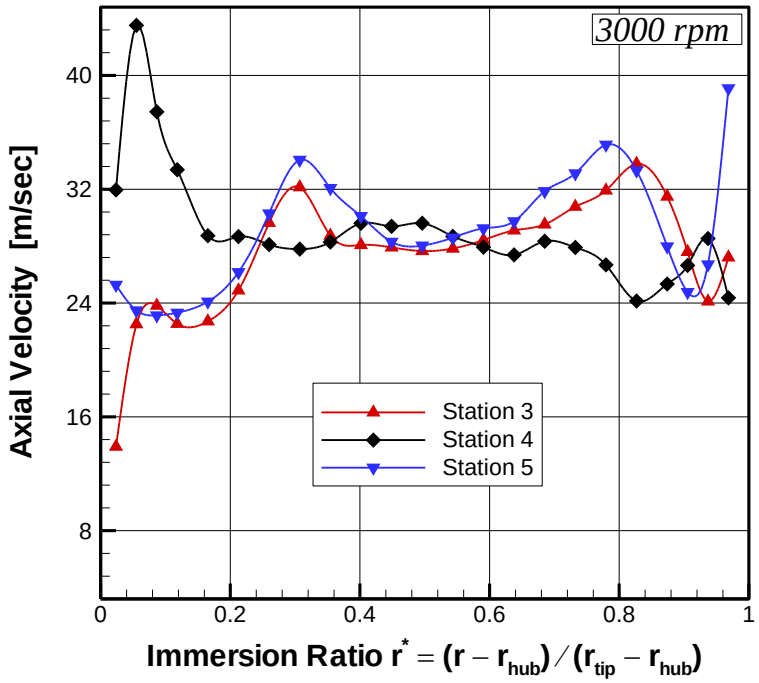

Figure 79: Radial distribution of the axial velocity at 3000 rpm

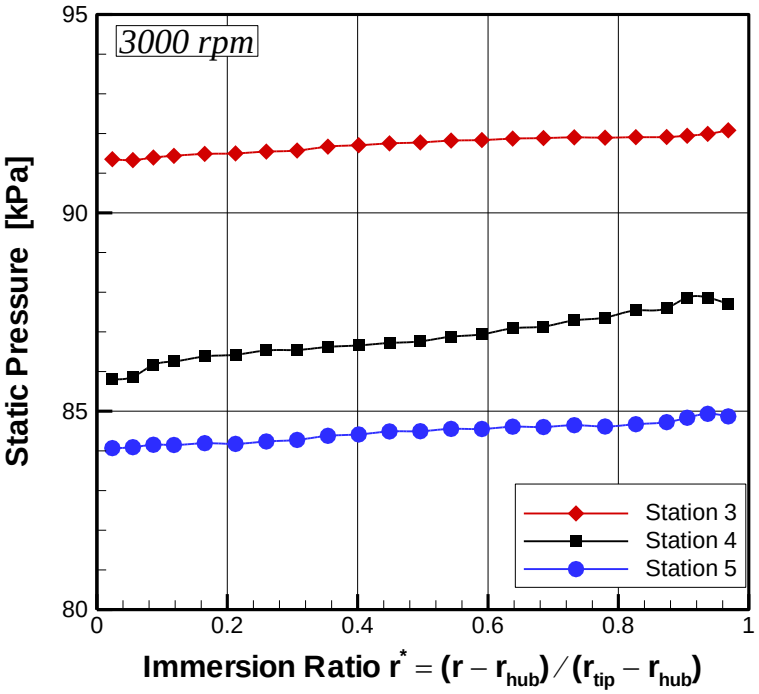

Figure 80: Radial distribution of static pressure at 3000 rpm

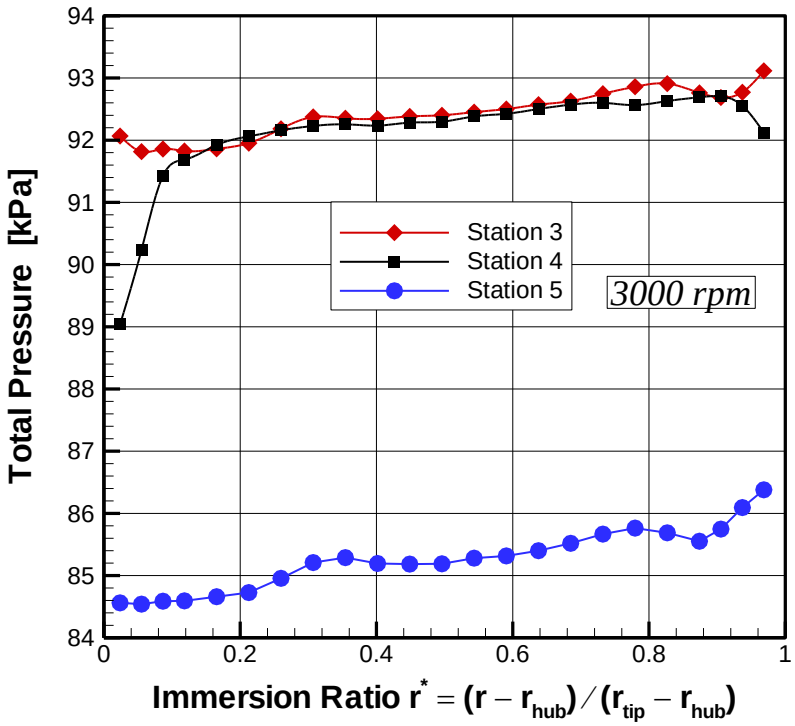

Figure 81: Radial distribution of the total pressure at 3000 rpm

Figure 80 and Figure 81 show the radial distribution of static pressure and total pressure at station 3, 4 and 5 respectively. In all stations static pressure slightly increased from hub to tip. Total pressure in station 4 shows how some irregularities at the hub and tip. In general total pressure at station 4 is slightly less than station 3 due to different losses involved. Similar to static pressure, total pressure at station 5 increased radially from hub to tip. Figure 72 shows the contour plot of the total pressure distribution downstream of the first rotor, at station 3. Three different flow regions are presented in this figure [9]. Near the hub due to the combined effect of secondary flow and mixing, a slightly lower total pressure region is visible. In the center, another region of slightly lower total pressure indicates the presence of relatively thick wakes. As stated

previously, pneumatic (five-hole) probes were used for this investigation. These probes inherently have low frequency response; however, the flow within the axial gaps is highly unsteady. To capture the flow details, high frequency response probes such as hot wire probes are required. Figure 73 reveals a relatively thick wake region immediately downstream of the stator blade trailing edge. The total pressure contour at station 5, (Figure 74), which is downstream of the second rotor, is similar to station 3 except at the hub secondary flows has been reduced by endwall contouring.

The interstage traversing provides the entire flow quantities, from which the absolute and relative total pressures and thus the total pressure loss coefficients for the stator and the rotor can be determined. By using circumferentially consistently averaged quantities, the total pressure loss coefficients for stator and rotor were defined as:

$$\zeta_{stator} = \frac{P_{t3} - P_{t4}}{\frac{1}{2}\rho V_4^{\,2}} \qquad (21)$$

$$\zeta_{rotor} = \frac{P_{tr4} - P_{tr5}}{\frac{1}{2}\rho W_5^2} \qquad (22)$$

In order to calculate the density and Mach number correctly, temperature measurements were done at four different locations at each stator. Figure 82 shows the temperature readings at each stator and presents how temperature drops at each stage.

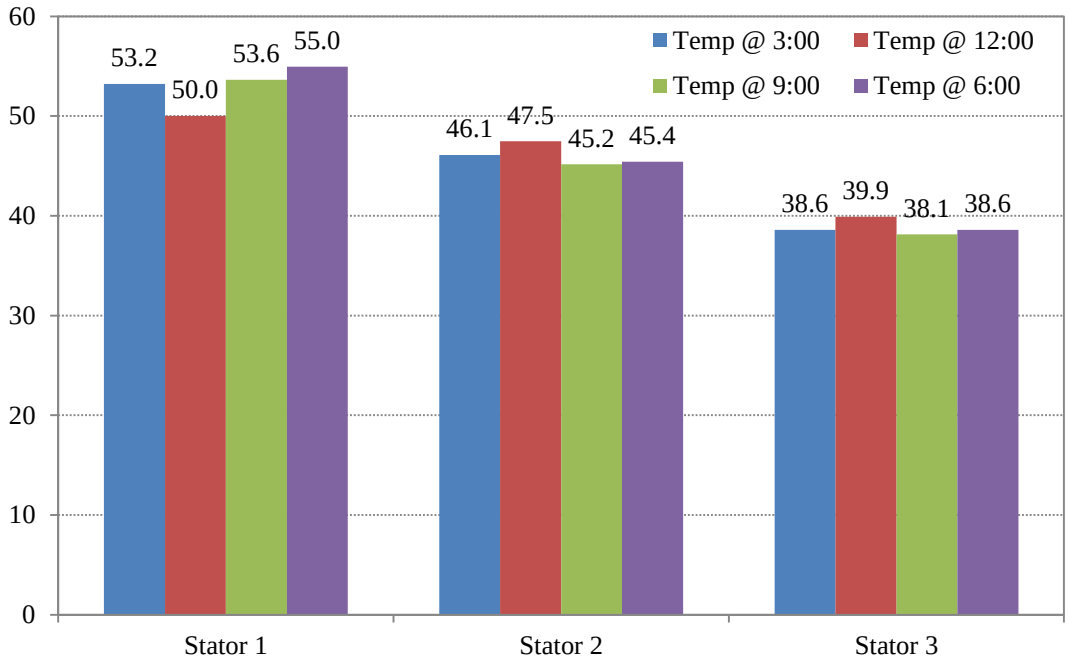

Figure 82: Temperature measurement at each stator

Total pressure loss coefficient is presented in Figure 83. In the stator, hub secondary flows play an important role to increase losses at about immersion ratio 0.15. Near the tip starts at about 90% immersion ratio, effect of casing secondary flows on total pressure loss is visible.

In the rotor, as discussed in previous section, 4 regions of high vortical flows affect the flow field. Near the hub at about immersion ratio 0.1 is affected by hub secondary flows. In this case since the endwall was contoured, significant reduction in total pressure loss coefficient can be seen.

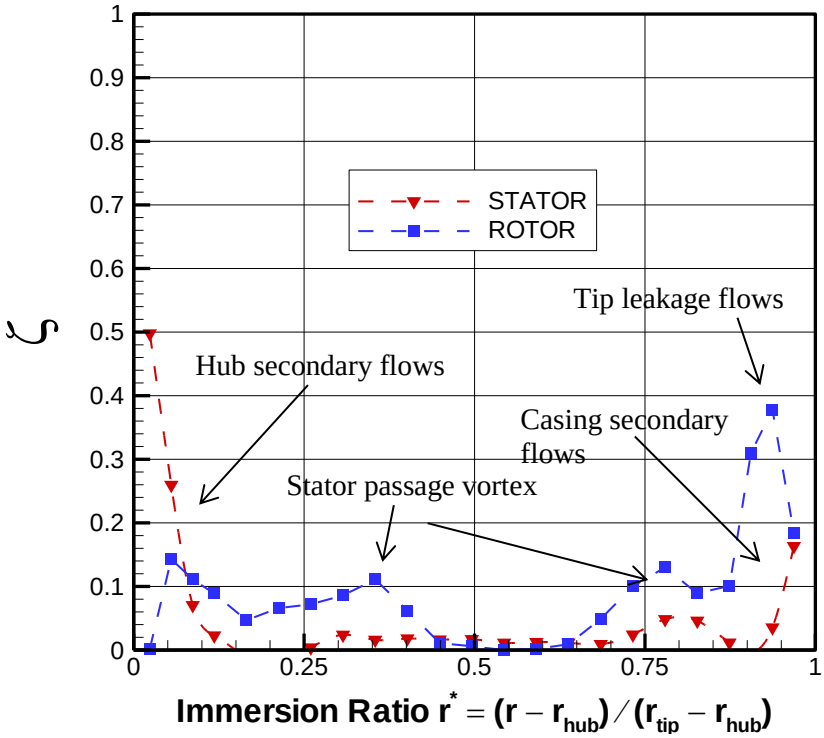

Figure 83: Total pressure loss coefficient at 3000 rpm

Second high loss area is around 35% of span. Due to the interaction between stator and rotor, stator hub passage vortex displaced radially upwards and increased the loss in this region.

Third high loss area is at immersion ration 0.8. Similar case happens at the rotor tip, where the stator tip passage vortex and tip leakage interaction causes the vortical structure move toward the midspan.

And finally the highest loss in the rotor happened at immersion ratio 0.95 where the tip leakages dominate the flow field. Pitchwise averaged total pressure loss coefficient is as high as 0.38.

7.2. Performance Results

This section focuses on the impact of the rotating purge flow on the performance of TPFL research turbine with non- axisymmetric endwall contouring. The purge flow investigation involves the reference case without endwall contouring followed by the investigation with endwall contouring. Before taking the final data, several preliminary experiments were conducted to ensure the reproducibility of the data.

After cutting the endwall contouring into the rotor hub, installing the blades, balancing, the rotor was inserted into the casing, instrumented and prepared for performance measurements. Final efficiency measurements presented in Figure 84 shows for the contoured rotor a maximum efficiency of 89.9% compared to the reference non-contoured case of $\eta_{t\text{-}s} = 88.86\%$. This is an efficiency increase of $\Delta\eta = 1.04\%$, which is almost double the value obtained from the numerical simulation of $\Delta\eta = 0.51\%$ presented in [8]. In addition to contoured endwall, second rotor blade number was also increased from 40 to 46.

This new method is particularly significant for applications to power generation steam turbines. The high, intermediate and low pressure units (HP, IP, LP) consist of many stages, with HP- and IP-units having moderate Zweifel coefficient. This coefficient makes them particularly suitable for application of this contouring method without changing the blade geometry. Contouring all rotor endwalls of these units will substantially increase the unit efficiency.

Figure 84 shows measured total-to-static efficiency as a function of u/c_o. The dimensionless parameter u/c_o is calculated from:

$$u = \omega . r_{mean}$$
$$c_o = \sqrt{\Delta H_i} \qquad (23)$$

Where r_{mean} is average turbine radius and ΔH_i is change in total enthalpy from rotor inlet to exit.

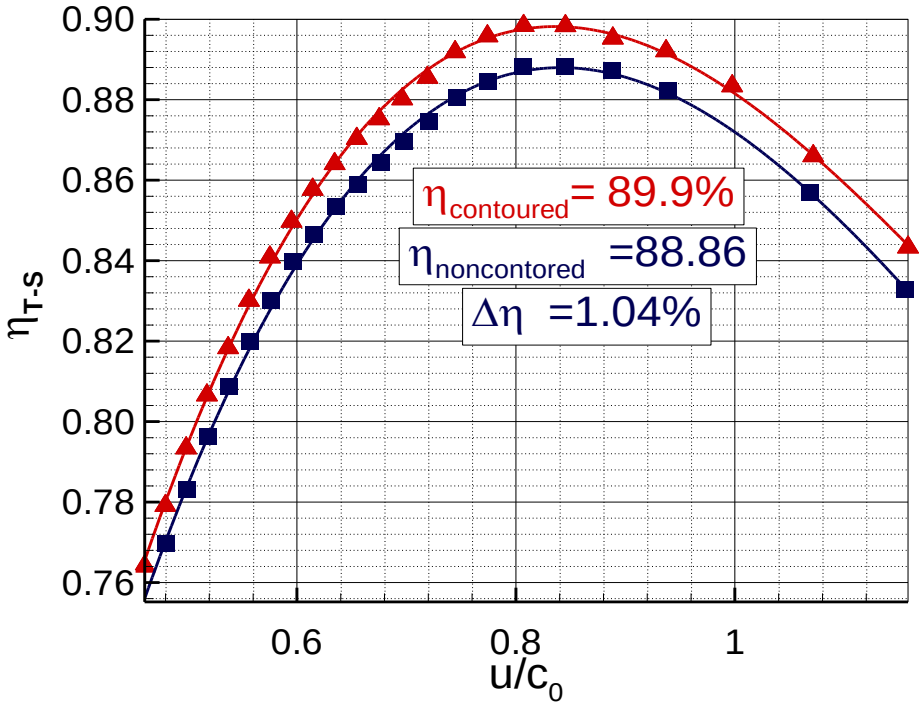

Figure 84: Measured total-to-static efficiency as a function of u/c_o

Injecting the purge mass flow causes the turbine mass flow to increase and the turbine efficiency to decrease. Figure 85 shows the mass flow distribution as a function

of turbine rotational speed with the mass flow ratio MFR as a parameter. As seen the lowest mass flow corresponds to the reference case of MFR=0. Increasing the MFR increases the turbine mass flow. The increased mass flow, however, causes a reduction of the turbine total-to-static efficiency as shown in Figure 86 and Figure 88. Moreover, Pressure ratio increased by increasing purge flow (Figure 87).

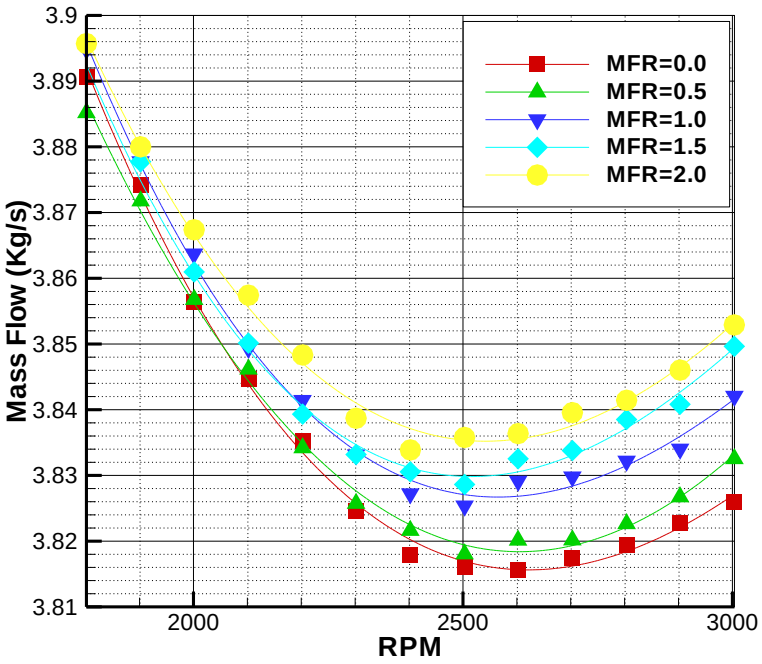

Figure 85: Measured turbine mass flow as a function of rotational speed with the purge mass flow ratio MFR as a parameter

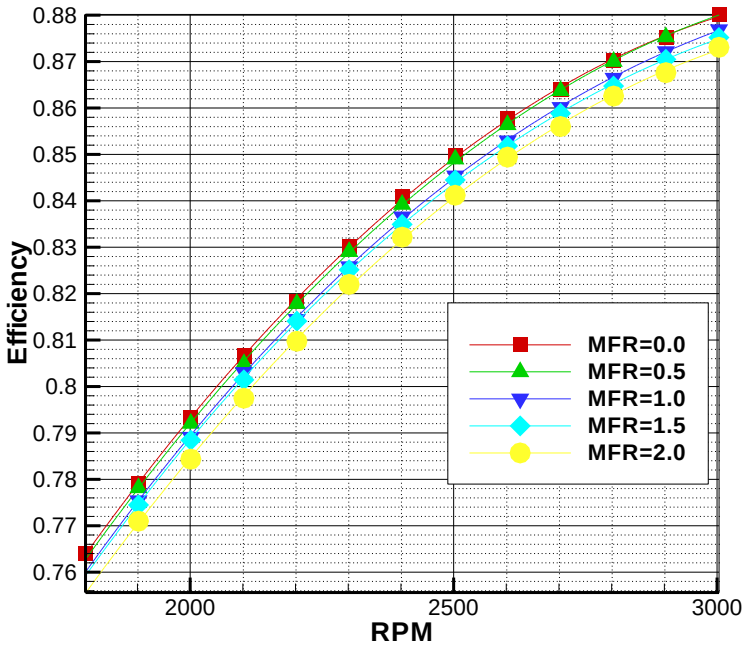

Figure 86: Measured turbine efficiency as a function of rotational speed with the purge mass flow ratio MFR as a parameter

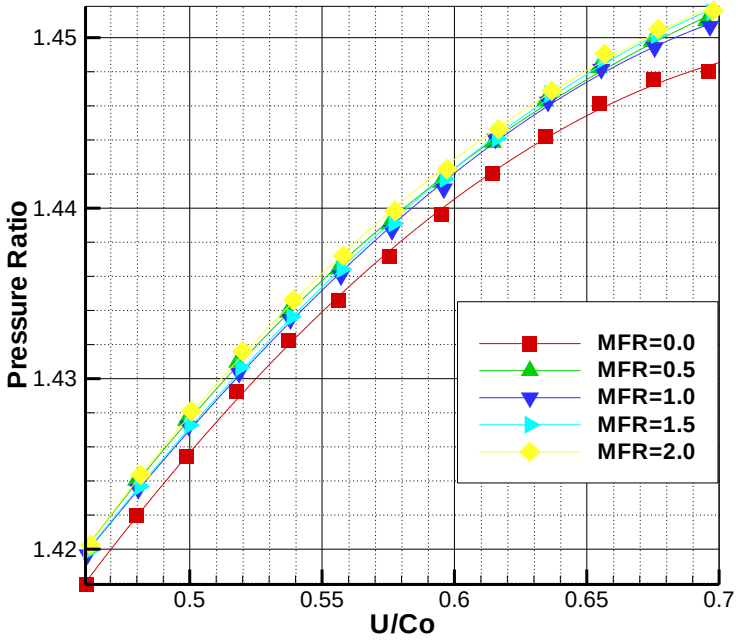

Figure 87: Measured turbine pressure ratio as a function of u/c_o with the purge mass flow ratio MFR as a parameter

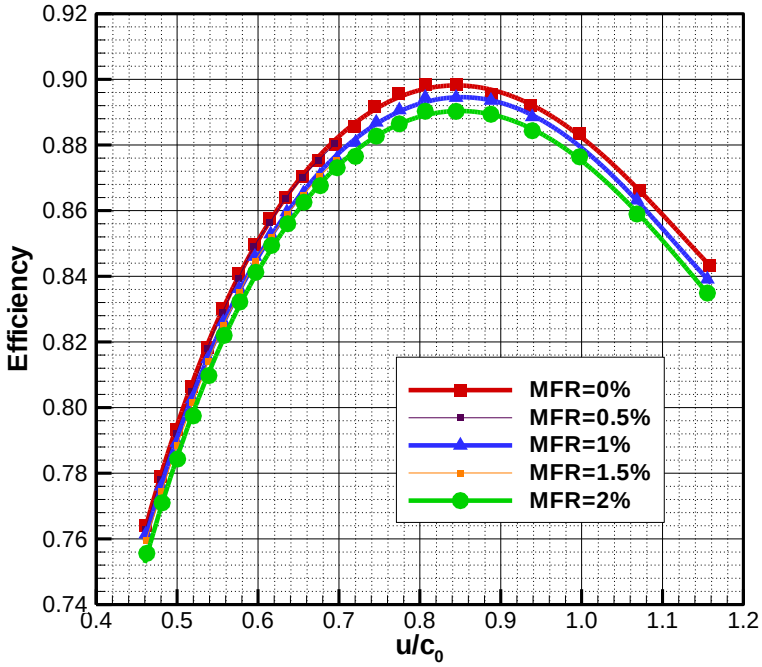

Figure 88: Measured turbine efficiency as a function of u/c_0 with the purge mass flow ratio MFR as a parameter

8. CONCLUSION

This dissertation deals with the specific heat transfer and aerodynamics problematic inherent to high pressure (HP) turbine sections. Issues of primary relevance to a turbine stage operating are: (1) decreasing the strength of the secondary flow vortices at the hub and tip regions to reduce (a), the secondary flow losses and (b), the potential for endwall deposition, erosion and corrosion due to secondary flow driven migration of gas flow particles to the hub and tip regions, (2) providing a robust film cooling technology at the hub and that sustains high cooling effectiveness less sensitive to deposition, (3) investigating the impact of blade tip geometry on film cooling effectiveness.

The experimental investigations were performed in the three-stage multi-purpose turbine research facility at the Turbomachinery Performance and Flow Research Laboratory (TPFL), Texas A&M University.

8.1. Aerodynamic Flow Measurement

Major efficiency improvement has been achieved by introducing a completely new endwall contouring technology which decreases the strength of the secondary flow vortices. The contouring was cut into the rotor hub of the three-stage TPFL-research turbine using CNC-machining. Efficiency measurements show for the contoured rotor a maximum efficiency of 89.9% compared to the reference non-contoured case of $\eta_{t\text{-}s}$ = 88.86%. This is an efficiency increase of η = 1.04%. This new method is particularly significant for applications to power generation steam turbines. The high-, intermediate

and low pressure units (HP, IP, LP) consist of many stages, with HP- and IP-units. Contouring all rotor endwalls of these units will substantially increase the unit efficiency. Interstage results also showed that how endwall contouring affected the flow field after the rotor passage and reduced the secondary flow vortices at the hub.

8.2. Contoured Endwall Film Cooling Effectiveness

The new method of endwall contouring not only has improved the turbine aerodynamic efficiency but it also has substantially improved the film cooling effectiveness of the contoured endwall. The endwall portion of the first turbine stage is generally subjected to higher temperatures requiring a thorough cooling. To accomplish this, purge air is extracted from the rotor internal cavity and is ejected through a circumferential slot onto the endwall of the first rotor row. To determine the impact of the endwall contouring on film cooling effectiveness, the new contouring technology was applied to the first rotor row. The film cooling experiments were carried out using pressure sensitive paint (PSP) measurement technique. Measurements were conducted for three coolant-to-mainstream mass flow ratios (MFR) of 0.5%, 1.0% and 1.5%. Film cooling data is also obtained for three rotational speeds, 3000 rpm (reference condition), 2550 rpm and 2400 rpm and they are compared with non-contoured endwall data. For 3000 rpm two more coolant to mainstream mass flow ratio of 0.75% and 1.25% are performed to have a better view of how film cooling effectiveness is changing. Comparing experimental results of the film cooling effectiveness investigations of the

contoured case with the reference non-contoured case, clearly shows the improving effect of contouring on film cooling effectiveness for all cases investigated in this report.

The results of the above research are summarized below:

1. The comparisons of film effectiveness results that pertain to the contoured cases with those of non-contoured ones show a noticeable quantitative improvement.
2. While the non-contoured reference case has lower effectiveness values at the leading edge, the contoured cases have much higher values.
3. Film cooling effectiveness increases with purge mass flow rate from 0.5% to 1.5%.
4. Film cooling effectiveness increases with RPM from 2400 to 3000rpm.
5. Contoured endwalls can provide better aerodynamics performance than non-contoured endwalls due to reduction in secondary flow losses.
6. Increasing the coolant to mainstream density ratio provides better passage platform coverage and increases the film cooling effectiveness.

8.3. Blade Tip Cooling

Detailed experimental investigations of film cooling effectiveness were conducted on the blade tips of the first rotor row pertaining to a three-stage research turbine. Four different blade tip ejection configurations were utilized to determine the impact of the hole arrangements on the film cooling effectiveness. The final configurations were manufactured and installed diametrically on the rotor hub to avoid

rotor imbalance. The first configuration includes a pair of blades with radially arranged ejection holes positioned along the camber of the blade flat tip. The second configuration consists of a pair of blades with radially arranged holes embedded in the blade tip squealer. The third configuration has a flat tip but the ejection holes are arranged on the pressure side under given ejection angles. The fourth configuration has the same pressure side hole arrangements as the third configuration but the tip has squealer shape. Measurements were performed using pressure sensitive paint (PSP) technique. Three blowing ratios M = 0.75, 1.25 and 1.75 at three different rotational speeds of 3000 rpm (reference condition), 2550 rpm and 2000 rpm were utilized.

The results of the above research are summarized below:

1) The film cooling ejections on both the plane tip and squealer tip dramatically affect the flow behaviors at the tip region. Strong interactions between the cooling jets and the leakage flow have been observed on both blade tips. However the flow characteristics on the plane tip differ from those on the squealer tip.
2) The overall film cooling effectiveness monotonically increases by increasing blowing ratios for all four configurations.
3) In plane tip, it is shown that the coolant particles tend to travel in the opposite direction of rotation, especially for the cooling jets exiting from the first two cooling holes. This phenomenon is due to the rotation and does not exist in a stationary cascade.

4) Film effectiveness decreases with RPM for all configurations, but increases with RPM for the Plane tip.

5) Film effectiveness for the plane tip follows net velocity vector of incident velocity and leakage velocity for three different RPM cases.

REFERENCES

[1] Lakshminarayana, B., 1995, "Fluid Dynamics and Heat Transfer of Turbomachinery," John Wiley & Sons, Inc., Hoboken, NJ, USA, .

[2] Schobeiri, M., 2012, "Turbomachinery Flow Physics and Dynamic Performance," Springer Berlin Heidelberg, Berlin ; London, .

[3] Denton, J. D., 1993, "Loss Mechanisms in Turbomachines," Journal of Turbomachinery, **115**(4) pp. 621-656.

[4] Langston, L. S., 1980, "Crossflows in a Turbine Cascade Passage," Journal of Engineering for Power, **102**(4) pp. 866-874.

[5] Goldstein, R. J., and Spores, R. A., 1988, "Turbulent Transport on the Endwall in the Region between Adjacent Turbine Blades," Journal of Heat Transfer, **110**(4) pp. 862-869.

[6] Sieverding, C. H., 1985, "Recent Progress in the Understanding of Basic Aspects of Secondary Flows in Turbine Blade Passages," Journal of Engineering for Gas Turbines and Power, **107**(2) pp. 248-157.

[7] Wang, H. P., Olson, S. J., Goldstein, R. J., 1997, "Flow Visualization in a Linear Turbine Cascade of High Performance Turbine Blades," Journal of Turbomachinery, **119**(1) pp. 1-8.

[8] Schobeiri, M. T., and Lu, K., 2013, "Endwall Contouring using Continuous Diffusion: A New Method and its Application to a Three-Stage High Pressure Turbine," Journal of Turbomachinery, **136**(1) pp. 011006.

[9] Schobeiri, M. T., Suryanarayanan, A., Jermann, C., 2004, "A Comparative Aerodynamic and Performance Study of a Three-Stage High Pressure Turbine With 3-D Bowed Blades and Cylindrical Blades," Proceedings of the ASME Turbo Expo, **GT2004-53650,** pp. 1237-1246.

[10] Abdelfattah, S. A., Chibli, H. A., and Schobeiri, M. T., 2011, "Aerodynamic Investigation of the Performance of a Two Stage Axial Turbine at Design and Off-Design Conditions," Proceedings of the ASME Turbo Expo, **GT2011-45909,** pp. 775-785.

[11] Sauer, H., Muller, R., and Vogeler, K., 2001, "Reduction of Secondary Flow Losses in Turbine Cascades by Leading Edge Modifications at the Endwall," Journal of Turbomachinery, **123**(2) pp. 207-213.

[12] Hartland, J., and Gregory-Smith, D., 2002, "A Design Method for the Profiling Of End Walls in Turbines," Proceedings of the ASME Turbo Expo, Amsterdam, Netherlands, **GT2002-30433,** pp. 697-704.

[13] Ingram, G., Gregory-Smith, D., Rose, M., 2002, "The Effect of End-Wall Profiling on Secondary Flow and Loss Development in a Turbine Cascade," Proceedings of the ASME TURBO EXPO, Amsterdam, Netherlands, **GT2002-30339,** pp. 135-145.

[14] Eymann, S., Reinmoller, U., Niehuis, R., 2002, "Improving 3D Flow Characteristics in a Multistage LP Turbine by Means of Endwall Contouring and Airfoil Design Modification - Part 1: Design and Experimental Investigation," Proceedings of the ASME TURBO EXPO, Amsterdam, Netherlands, **GT2002-30352,** pp. 249-260.

[15] Ingram, G., Gregory-Smith, D., and Harvey, N., 2005, "Investigation of a Novel Secondary Flow Feature in a Turbine Cascade with End Wall Profiling," Journal of Turbomachinery, **127**(1) pp. 209-214.

[16] Saha, A. K., and Acharya, S., 2008, "Computations of Turbulent Flow and Heat Transfer through a Three-Dimensional Nonaxisymmetric Blade Passage," Journal of Turbomachinery, **130**(3) pp. 031008-031008.

[17] Praisner, T. J., Allen-Bradley, E., Grover, E. A., 2013, "Application of Nonaxisymmetric Endwall Contouring to Conventional and High-Lift Turbine Airfoils," Journal of Turbomachinery, **135**(6) pp. 061006-061006.

[18] Harvey, N. W., Rose, M. G., Taylor, M. D., 1999, "Nonaxisymmetric Turbine End Wall Design: Part I- Three-Dimensional Linear Design System," Journal of Turbomachinery, **122**(2) pp. 278-285.

[19] Hartland, J. C., Gregory-Smith, D., Harvey, N. W., 1999, "Nonaxisymmetric Turbine End Wall Design: Part II- Experimental Validation," Journal of Turbomachinery, **122**(2) pp. 286-293.

[20] Brennan, G., Harvey, N. W., Rose, M. G., 2003, "Improving the Efficiency of the Trent 500-HP Turbine using Nonaxisymmetric End Walls-Part I: Turbine Design," Journal of Turbomachinery, **125**(3) pp. 497-504.

[21] Harvey, N. W., Brennan, G., Newman, D. A., 2002, "Improving Turbine Efficiency Using Non-Axisymmetric End Walls: Validation in the Multi-Row Environment and with Low Aspect Ratio Blading," Proceedings of the ASME Turbo Expo, Amsterdam, Netherlands, **GT2002-30337,** pp. 119-126.

[22] Germain, T., Nagel, M., Raab, I., 2010, "Improving Efficiency of a High Work Turbine using Nonaxisymmetric Endwalls— Part I: Endwall Design and Performance," Journal of Turbomachinery, **132**(2) pp. 021007.

[23] Snedden, G., Dunn, D., Ingram, G., 2009, "The Application of Non-Axisymmetric Endwall Contouring in a Single Stage, Rotating Turbine," Proceedings of the ASME Turbo Expo, Orlando, FL, United states, **GT2009-59169,** pp. 831-840.

[24] Snedden, G., Dunn, D., Ingram, G., 2010, "The Performance of a Generic Non-Axisymmetric End Wall in a Single Stage, Rotating Turbine at On And Off-Design Conditions," Proceedings of the ASME Turbo Expo, Glasgow, United kingdom, **GT2010-22006,** pp. 1069-1080.

[25] Khajavi, M. R., and Shariat, M. H., 2004, "Failure of First Stage Gas Turbine Blades," Engineering Failure Analysis, **11**(4) pp. 589-597.

[26] Han, J., Dutta, S., and Ekkad, S., "Gas Turbine Heat Transfer and Cooling Technology," Taylor & Francis Group, .

[27] Suryanarayanan, A., Mhetras, S. P., Schobeiri, M. T., 2009, "Film-Cooling Effectiveness on a Rotating Blade Platform," Journal of Turbomachinery, **131**(1) pp. 011014.

[28] Suryanarayanan, A., Ozturk, B., Schobeiri, M. T., 2010, "Film-Cooling Effectiveness on a Rotating Turbine Platform using Pressure Sensitive Paint Technique," Journal of Turbomachinery, **132**(4) pp. 041001.

[29] Schuepbach, P., Abhari, R. S., Rose, M. G., 2011, "Influence of Rim Seal Purge Flow on the Performance of an Endwall-Profiled Axial Turbine," Journal of Turbomachinery, **133**(2) .

[30] Jenny, P., Abhari, R. S., Rose, M. G., 2012, "A Low Pressure Turbine with Profiled Endwalls and Purge Flow Operating with a Pressure Side Bubble," Journal of Turbomachinery, **134**(6) pp. 061038 (9 pp.).

[31] Metzger, D. E., Bunker, R. S., and Chyu, M. K., 1989, "Cavity Heat Transfer on a Transverse Grooved Wall in a Narrow Flow Channel," Journal of Heat Transfer, **111**(1) pp. 73-79.

[32] Kim, Y. W., and Metzger, D. E., 1995, "Heat Transfer and Effectiveness on Film Cooled Turbine Blade Tip Models," Journal of Turbomachinery, **117**(1) pp. 12-21.

[33] Kim, Y. W., Downs, J. P., Soechting, F. O., 1995, "Summary of the Cooled Turbine Blade Tip Heat Transfer and Film Effectiveness Investigations Performed by Dr. D. E. Metzger," Journal of Turbomachinery, **117**(1) pp. 1-11.

[34] Bunker, R. S., 2006, "Axial Turbine Blade Tips: Function, Design, and Durability," Journal of Propulsion and Power, **22**(2) pp. 271-285.

[35] Azad, G. S., Han, J., and Boyle, R. J., 2000, "Heat Transfer and Flow on the Squealer Tip of a Gas Turbine Blade," Journal of Turbomachinery, **122**(4) pp. 725.

[36] Azad, G. S., Han, J., Teng, S., 2000, "Heat Transfer and Pressure Distributions on a Gas Turbine Blade Tip," Journal of Turbomachinery, **122**(4) pp. 717.

[37] Bunker, R. S., Bailey, J. C., and Ameri, A. A., 1999, "Heat Transfer and Flow on the First-Stage Blade Tip of a Power Generation Gas Turbine: Part 1-Experimental Results," Journal of Turbomachinery, **122**(2) pp. 263-271.

[38] Ameri, A. A., and Bunker, R. S., 2000, "Heat Transfer and Flow on the First-Stage Blade Tip of a Power Generation Gas Turbine: Part 2-Simulation Results," Journal of Turbomachinery, **122**(2) pp. 272-277.

[39] Kwak, J. S., and Han, J., 2003, "Heat Transfer Coefficients and Film-Cooling Effectiveness on a Gas Turbine Blade Tip," Journal of Heat Transfer, **125**(3) pp. 494-502.

[40] Kwak, J. S., and Han, J., 2003, "Heat Transfer Coefficients and Film Cooling Effectiveness on the Squealer Tip of a Gas Turbine Blade," Journal of Turbomachinery, **125**(4) pp. 648-657.

[41] Christophel, J. R., Thole, K. A., and Cunha, F. J., 2005, "Cooling the Tip of a Turbine Blade using Pressure Side Holes-Part I: Adiabatic Effectiveness Measurements," Journal of Turbomachinery, **127**(2) pp. 270-7.

[42] Gao, Z., Narzary, D., Mhetras, S., 2009, "Effect of Inlet Flow Angle on Gas Turbine Blade Tip Film Cooling," Journal of Turbomachinery, **131**(3) .

[43] Park, J. S., Lee, D. H., Cho, H. H., 2010, "Heat Transfer and Effectiveness on the Film Cooled Tip and Inner Rim Surfaces of a Turbine Blade," Proceedings of the ASME Turbo Expo, Glasgow, United kingdom, **GT2010-23203,** pp. 1751-1761.

[44] Dring, R. P., Blair, M. F., and Joslyn, H. D., 1980, "An Experimental Investigation of Film Cooling on a Turbine Rotor Blade," Journal of Engineering for Power, **102**(1) pp. 81-7.

[45] Takeishi, K., Aoki, S., Sato, T., 1992, "Film Cooling on a Gas Turbine Rotor Blade," Journal of Turbomachinery, **114**(4) pp. 828.

[46] Abhari, R. S., and Epstein, A. H., 1994, "Experimental Study of Film Cooling in a Rotating Transonic Turbine," Journal of Turbomachinery, **116**(1) pp. 63-70.

[47] Acharya, S., and Moreaux, L., 2014, "Numerical Study of the Flow Past a Turbine Blade Tip: Effect of Relative Motion between Blade and Shroud," Journal of Turbomachinery, **136**(3) .

[48] Yang, D., Yu, X., and Feng, Z., 2010, "Investigation of Leakage Flow and Heat Transfer in a Gas Turbine Blade Tip with Emphasis on the Effect of Rotation," Journal of Turbomachinery, **132**(4) pp. 041010 (9 pp.).

[49] Lu, K., Schobeiri, M. T., and Han, J. C., 2013, "Numerical simulation of film cooling on rotating blade tips within a high-pressure turbine," Proceedings of the ASME Turbo Expo, San Antonio, Tx, United states, **GT2013-94806,** .

[50] Molter, S. M., Dunn, M. G., Haldeman, C. W., 2006, "Heat-Flux Measurements and Predictions for the Blade Tip Region of a High-Pressure Turbine," Proceedings of the ASME TURBO EXPO, Barcelona, Spain, **GT2006-90048,** pp. 49-60.

[51] Ahn, J., Schobeiri, M. T., Han, J., 2006, "Film Cooling Effectiveness on the Leading Edge Region of a Rotating Turbine Blade with Two Rows of Film Cooling Holes using Pressure Sensitive Paint," Journal of Heat Transfer, **128**(9) pp. 879.

[52] Ahn, J., Schobeiri, M. T., Han, J., 2007, "Effect of Rotation on Leading Edge Region Film Cooling of a Gas Turbine Blade with Three Rows of Film Cooling Holes," International Journal of Heat and Mass Transfer, **50**(1-2) pp. 15-25.

[53] Schobeiri, M.T., Gilarranz, J., and Johansen, E., 1999, "Final Report on: Efficiency, Performance, and Interstage Flow Field Measurement of Siemens-Westinghouse HP Turbine Blade Series 9600 and 5600," TPFL-Westinghouse, .

[54] Schobeiri, M., Gilarranz, J., and Johansen, E., 2004, "Aerodynamic and Performance Behavior of a Three-Stage High Efficiency Turbine at Design and Off-Design Operating Points," The International Journal of Rotating Machinery, **10**(1) pp. 33-44.

[55] Schobeiri, M. T., Lu, K., and Han, J. C., 2012, "Numerical Investigation of the Effect of Purge Flow on Aerodynamic Performance and Film Cooling Effectiveness on a Rotating Turbine with Non-Axisymmetric Endwall Contouring," Proceedings of the ASME Turbo Expo, Copenhagen, Denmark, **GT2012-69069,** pp. 413-423.

[56] Lu, K., 2014, "Numerical Investigations of Flow and Film Cooling with Endwall Contouring and Blade Tip Ejection Under Rotating Turbine Conditions," Texas A & M University, Doctoral Dissertation.

[57] Rezasoltani, M., Lu, K., Schobeiri, M. T., 2015, "A Combined Experimental and Numerical Study of the Turbine Blade Tip Film Cooling Effectiveness Under Rotation Condition," Journal of Turbomachinery, **137**(5) pp. 051009.

[58] Krause, L. N., and Dudzinski, T. J., 1969, "Flow-Direction Measurement with Fixed-Position Probes in Subsonic Flow over a Range of Reynolds Numbers," 15th international ISA aerospace instrumentation symposium, Pittsburgh, PA, USA, pp. 217-23.

[59] Morrison, G. L., Schobeiri, M. T., and Pappu, K. R., 1998, "Five-Hole Pressure Probe Analysis Technique," Flow Measurement and Instrumentation, **9**(3) pp. 153-158.

[60] Wendt, B. J., and Reichert, B. A., 1993, "New Algorithm for Five-Hole Probe Calibration and Data Reduction and Its Application to a Rake-Type Probe," Proceedings of the Fluids Engineering Conference, Washington, DC, USA, **161,** pp. 29-35.

[61] Town, J., and Camci, C., 2011, "Sub-Miniature Five-Hole Probe Calibration Using a Time Efficient Pitch and Yaw Mechanism and Accuracy Improvements," Proceedings of ASME Turbo Expo, Vancouver, BC, Canada, **GT2011-46391,** pp. 349-359.

[62] Rubner, K., and Bohn, D., 1972, "Method for the Evaluation of Measurement Results of Flow Probes by Means of Multidimensional Approximation of Calibration Curves and Calibration Planes; Verfahren Fuer Die Auswertung Der Messergebnisse Von Stroemungssonden Durch Mehrdimensionale

Approximation Der Eichkurven Und Eichflaechen," Zeitschrift Fuer Flugwissenschaften, **20**(1-2) pp. 36-42.

[63] Nicoll, W. B., and Whitelaw, J. H., 1967, "The Effectiveness of the Uniform Density, Two-Dimensional Wall Jet," International Journal of Heat and Mass Transfer, **10**(5) pp. 623-639.

[64] Friedrichs, S., Hodson, H. P., and Dawes, W. N., 1996, "Heat Transfer Committee Best Paper of 1995 Award: Distribution of Film-Cooling Effectiveness on a Turbine Endwall Measured using the Ammonia and Diazo Technique," Journal of Turbomachinery, **118**(4) pp. 613.

[65] Goldstein, R. J., and Jin, P., 2001, "Film Cooling Downstream of a Row of Discrete Holes with Compound Angle," Journal of Turbomachinery, **123**(2) pp. 222.

[66] Zhang, L. J., and Jaiswal, R. S., 2001, "Turbine Nozzle Endwall Film Cooling Study using Pressure-Sensitive Paint," Journal of Turbomachinery, **123**(4) pp. 730-738.

[67] Kays, W.M., Crawford, M.E., and Weigand, B., 2005, "Convective Heat and Mass Transfer," Mcgraw-Hill, .

[68] Han, J., and Rallabandi, A. P., 2010, "Turbine Blade Film Cooling using PSP Technique," Frontiers in Heat and Mass Transfer, **1**(1) .

[69] Jones, T. V., 1999, "Theory for the Use of Foreign Gas in Simulating Film Cooling," International Journal of Heat and Fluid Flow, **20**(3) pp. 349-354.

[70] Peterson, J. I., and Fitzgerald, R. V., 1980, "New Technique of Surface Flow Visualization Based on Oxygen Quenching of Fluorescence," Review of Scientific Instruments, **51**(5) pp. 670-671.

[71] Ardasheva, M. M., Nevskii, L. B., and Pervushin, G. E., 1985, "Measurement of Pressure Distribution by Means of Indicator Coatings," Journal of Applied Mechanics and Technical Physics, **26**(4) pp. 469-474.

[72] Vollan, A., and Alati, L., 1991, "A New Optical Pressure Measurement System (OPMS)," Proceedings of the Instrumentation in Aerospace Simulation Facilities, IEEE, Rockville, MD, USA, pp. 10-16.

[73] Kavandi, J., Callis, J., Gouterman, M., 1990, "Luminescent Barometry in Wind Tunnels," Review of Scientific Instruments, **61**(11) pp. 3340-3347.

[74] McLachlan, B. G., Kavandi, J. L., Callis, J. B., 1993, "Surface Pressure Field Mapping using Luminescent Coatings," Experiments in Fluids, **14**(1-2) pp. 33-41.

[75] McLachlan, B. G., and Bell, J. H., 1995, "Pressure-Sensitive Paint in Aerodynamic Testing," Experimental Thermal and Fluid Science, **10**(4) pp. 470-485.

[76] MORRIS, M. J., DONOVAN, J. F., KEGELMAN, J. T., 1993, "Aerodynamic Applications of Pressure Sensitive Paint," AIAA Journal, **31**(3) pp. 419-425.

[77] Dowgwillo, R., Morris, M., Donovan, J., 1994, "The Application of the Pressure Sensitive Paint Technique to High Speed Wind Tunnel Testing of a Fighter Aircraft Configuration with Complex Store Loadings," Proceedings of the 12th Applied Aerodynamics Conference, Colorado Springs, CO, USA, **AIAA-94-1932-CP,** .

[78] Engler, R. H., Hartmann, K., and Schulze, B., 1991, "Aerodynamic Assessment of an Optical Pressure Measurement System (OPMS) by Comparison with Conventional Pressure Measurements in a High Speed Wind Tunnel," Proceedings of the Instrumentation in Aerospace Simulation Facilities, IEEE, Rockville, MD, USA, pp. 17-24.

[79] Wright, L. M., Gao, Z., Varvel, T. A., 2005, "Assessment of Steady State PSP, TSP, and IR Measurement Techniques for Flat Plate Film Cooling," Proceedings of the ASME Summer Heat Transfer Conference, San Francisco, CA, United states, **HT2005-72363,** pp. 37-46.

[80] Rallabandi, A. P., Grizzle, J., and Je-Chin Han, 2011, "Effect of Upstream Step on Flat Plate Film-Cooling Effectiveness using PSP," Journal of Turbomachinery, **133**(4) pp. 041024 (8 pp.).

[81] Coleman, H.W., and Steele, W.G., 2009, "Experimentation, Validation, and Uncertainty Analysis for Engineers," Wiley, pp. 336.

[82] Holman, J.P., 2001, "Experimental Methods for Engineers," McGraw-Hill, Boston, pp. 698.

[83] Narzary, D. P., Liu, K., and Han, J., 2012, "Influence of Coolant Density on Turbine Blade Platform Film-Cooling," Journal of Thermal Science and Engineering Applications, **4**(2) pp. 021002-021002.

[84] Ahn, J., Mhetras, S., and Han, J., 2005, "Film-Cooling Effectiveness on a Gas Turbine Blade Tip using Pressure-Sensitive Paint," Journal of Heat Transfer, **127**(5) pp. 521-530.

[85] Hodson, H. P., Banieghbal, M. R., and Dailey, G. M., 1995, "Three-Dimensional Interactions in the Rotor of an Axial Turbine," Journal of Propulsion and Power, **11**(2) pp. 196-204.

[86] Chaluvadi, V. S. P., V., Kalfas, A. I., Banieghbal, M. R., 2001, "Blade-Row Interaction in a High-Pressure Turbine," Journal of Propulsion and Power, **17**(4) pp. 892-901.

[87] Pullan, G., 2004, "Secondary Flows and Loss Caused by Blade Row Interaction in a Turbine Stage," Journal of Turbomachinery, **128**(3) pp. 484-491.

[88] Porreca, L., Kalfas, A. I., Abhari, R. S., 2008, "Interstage Flow Interactions and Loss Generation in a Two-Stage Shrouded Axial Turbine," Journal of Turbomachinery, **131**(1) pp. 011002-011002.

[89] Porreca, L., Behr, T., Schlienger, J., 2004, "Fluid Dynamics and Performance of Partially and Fully Shrouded Axial Turbines," Journal of Turbomachinery, **127**(4) pp. 668-678.

[90] Behr, T., Porreca, L., Mokulys, T., 2005, "Multistage Aspects and Unsteady Effects of Stator and Rotor Clocking in an Axial Turbine with Low Aspect Ratio Blading," Journal of Turbomachinery, **128**(1) pp. 11-22.

[91] Gaetani, P., Persico, G., Dossena, V., 2006, "Investigation of the Flow Field in a High-Pressure Turbine Stage for Two Stator-Rotor Axial Gaps-Part II: Unsteady Flow Field," Journal of Turbomachinery, **129**(3) pp. 580-590.

[92] Persico, G., Gaetani, P., and Osnaghi, C., 2009, "A Parametric Study of the Blade Row Interaction in a High Pressure Turbine Stage," Journal of Turbomachinery, **131**(3) pp. 031006-031006.

[93] Persico, G., Mora, A., Gaetani, P., 2012, "Unsteady Aerodynamics of a Low Aspect Ratio Turbine Stage: Modeling Issues and Flow Physics," Journal of Turbomachinery, **134**(6) pp. 061030-061030.

APPENDIX A

INTERSTAGE RESULTS

In this appendix the results of the interstage traversing measurements tests performed are plotted. Results for 2000 rpm were taken at compressor frequency=55Hz, Pressure ratio= 1.3 and mass flow rate around 3.46 kg/s. Results for 2000 rpm were taken at compressor frequency=65Hz, Pressure ratio= 1.435 and mass flow rate around 3.84 kg/s.

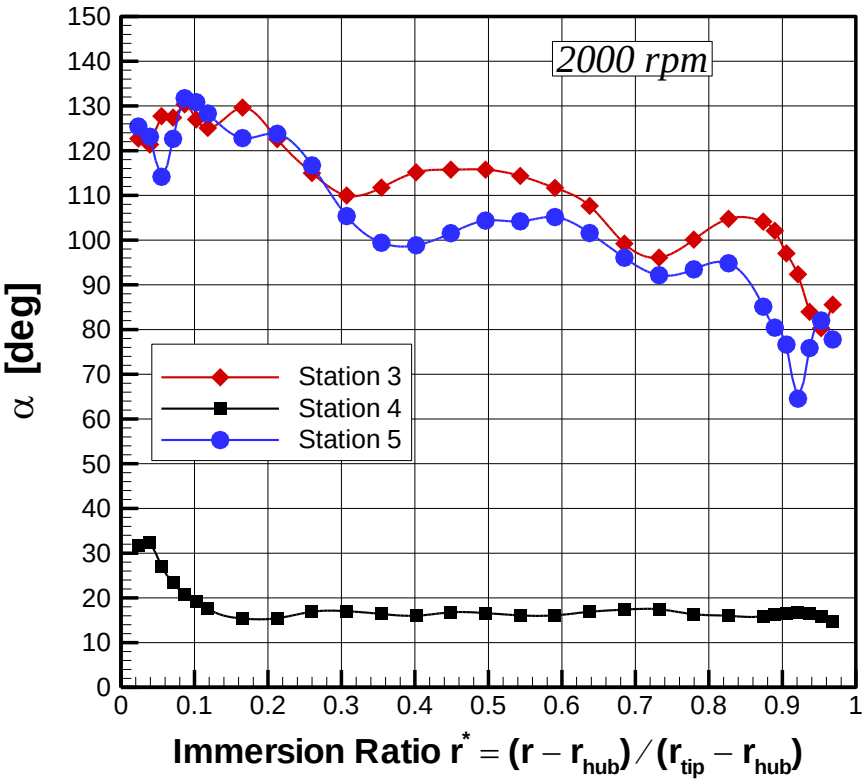

FigureA-1: Radial distribution of the absolute flow angle at 2000 rpm

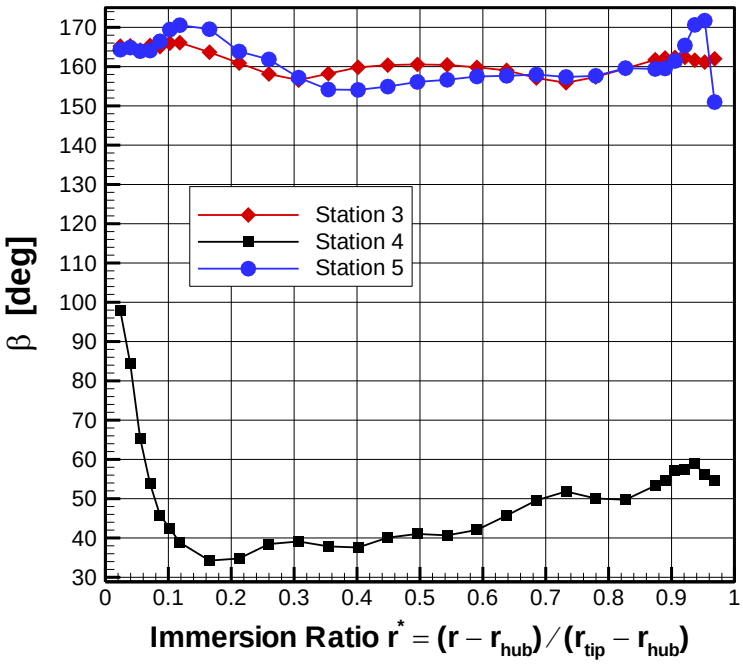

FigureA-2: Radial distribution of relative flow angle at 2000 rpm

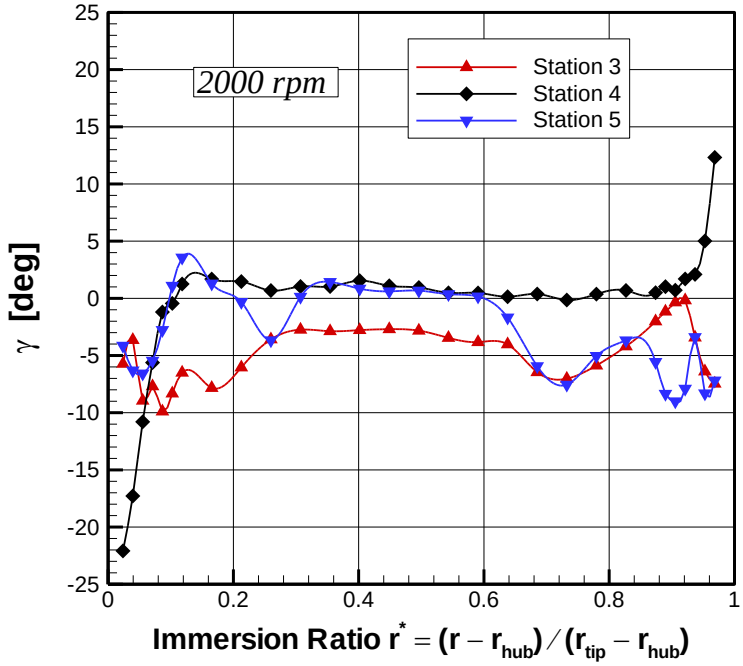

FigureA-3: Radial distribution of meridian flow angle at 2000 rpm

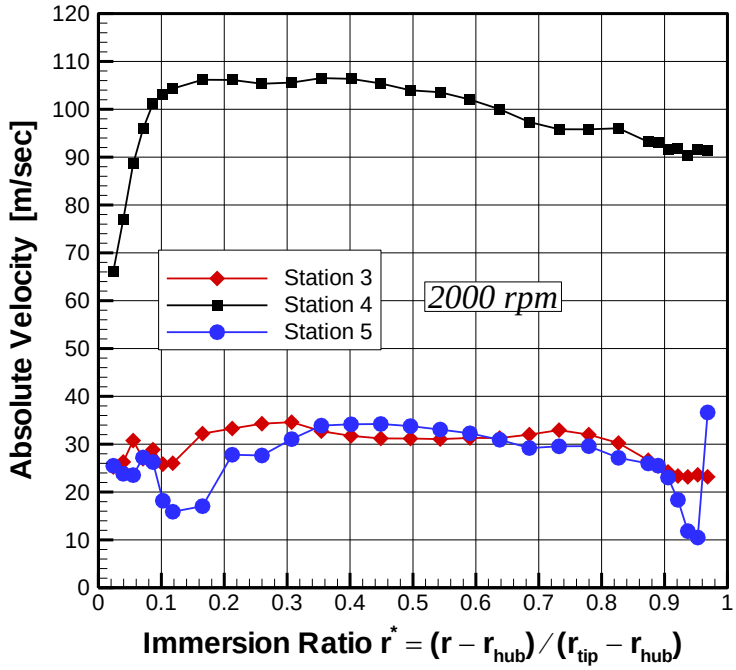

FigureA-4: Radial distribution of absolute velocity at 2000 rpm

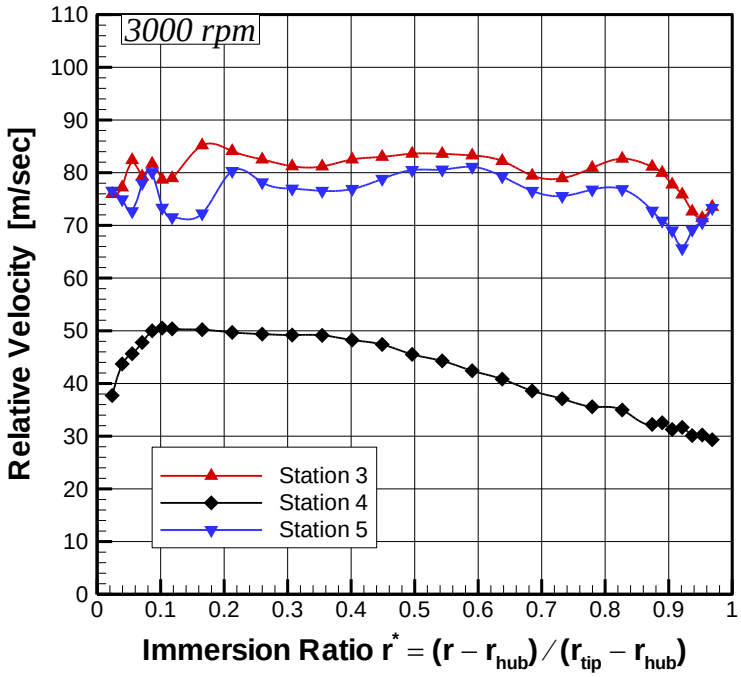

FigureA-5: Radial distribution of relative velocity at 2000 rpm

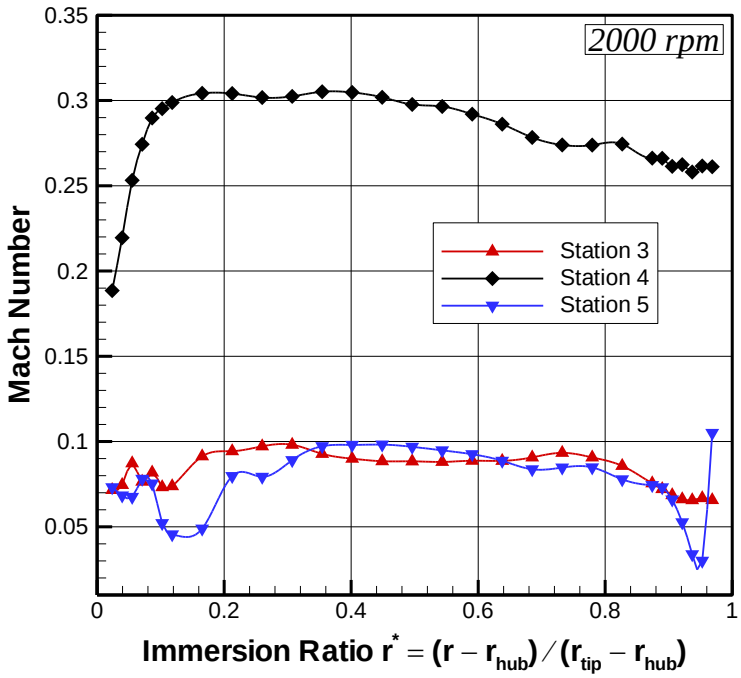

FigureA-6: Radial distribution of Mach number at 2000 rpm

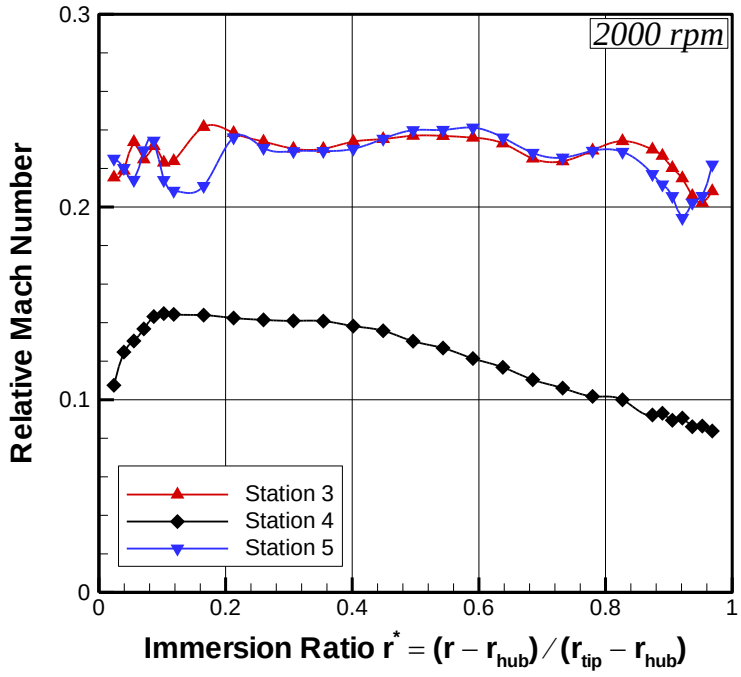

FigureA-7: Radial distribution of relative Mach number at 2000 rpm

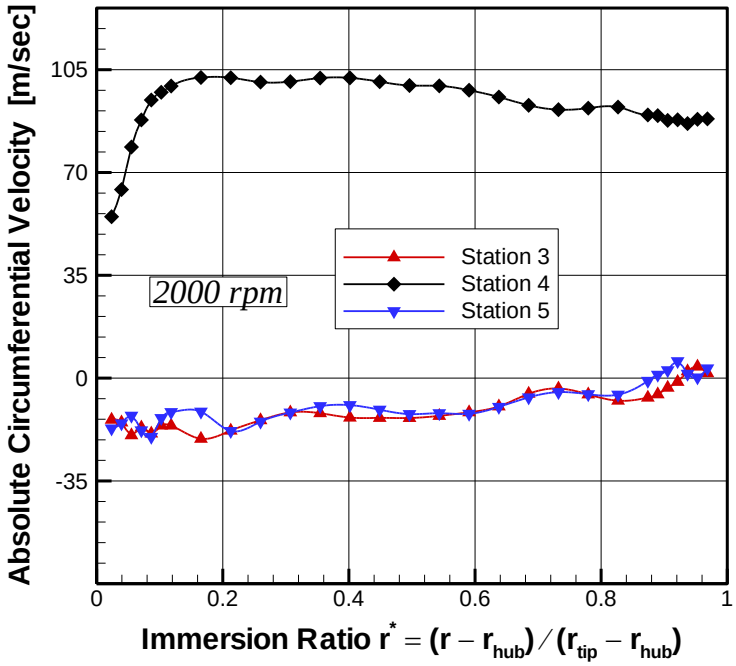

FigureA-8: Radial distribution of absolute circumferential velocity at 2000 rpm

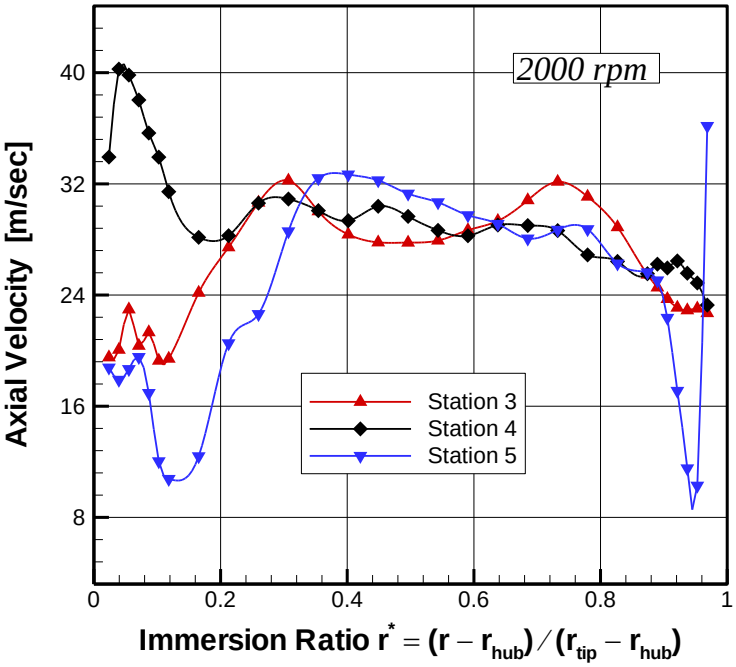

FigureA-9: Radial distribution of axial velocity at 2000 rpm

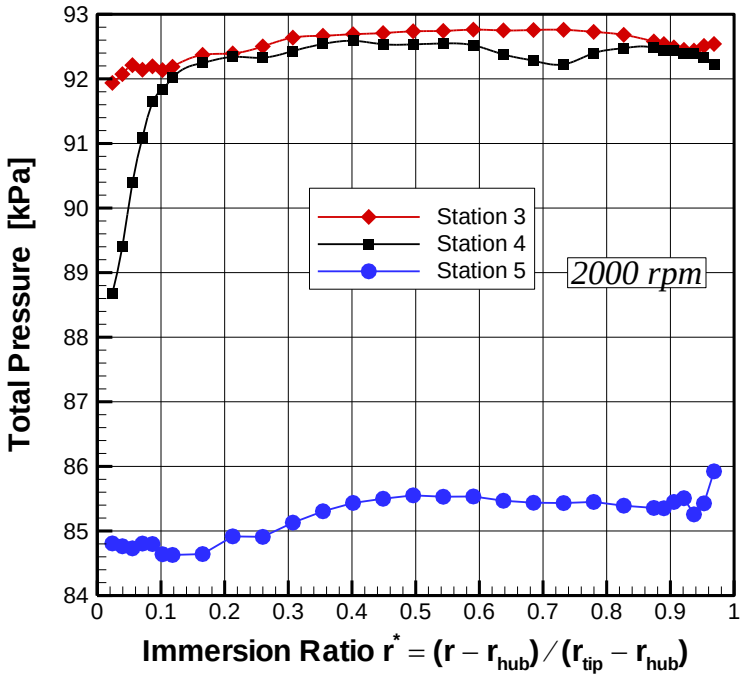

FigureA-10: Radial distribution of total pressure at 2000 rpm

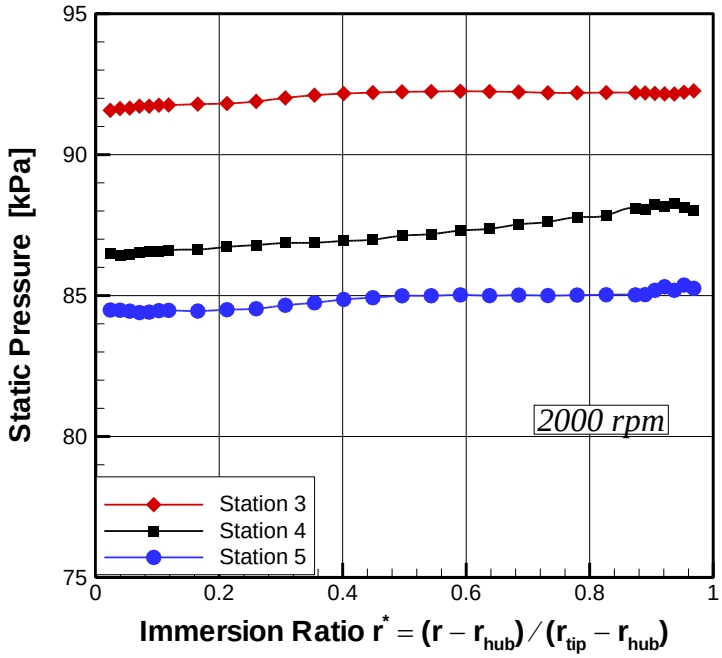

FigureA-11: Radial distribution of static pressure at 2000 rpm

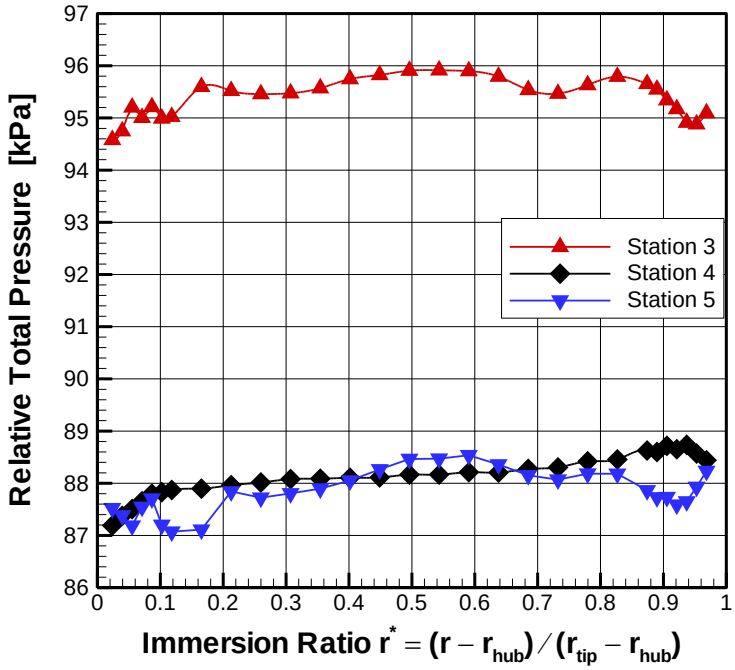

FigureA-12: Radial distribution of relative total pressure at 2000 rpm

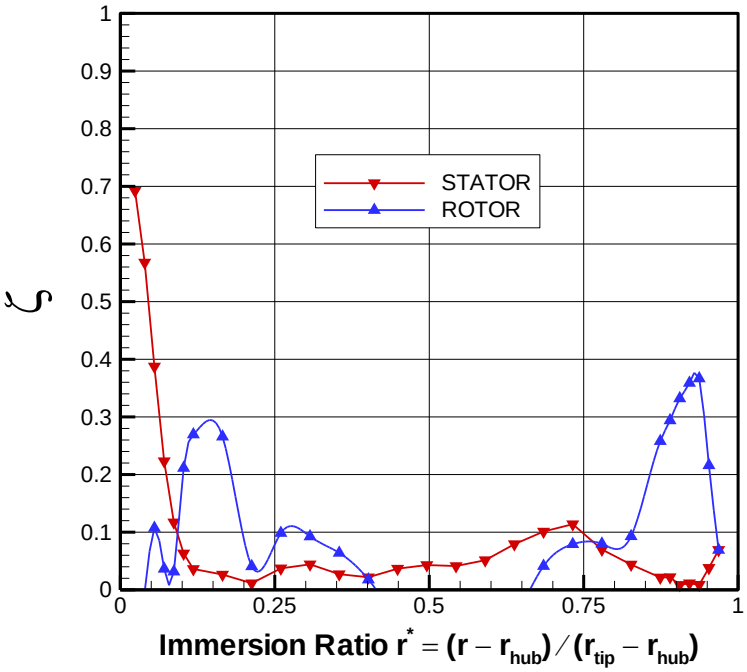

FigureA-13: Radial distribution of loss coefficient at 2000 rpm

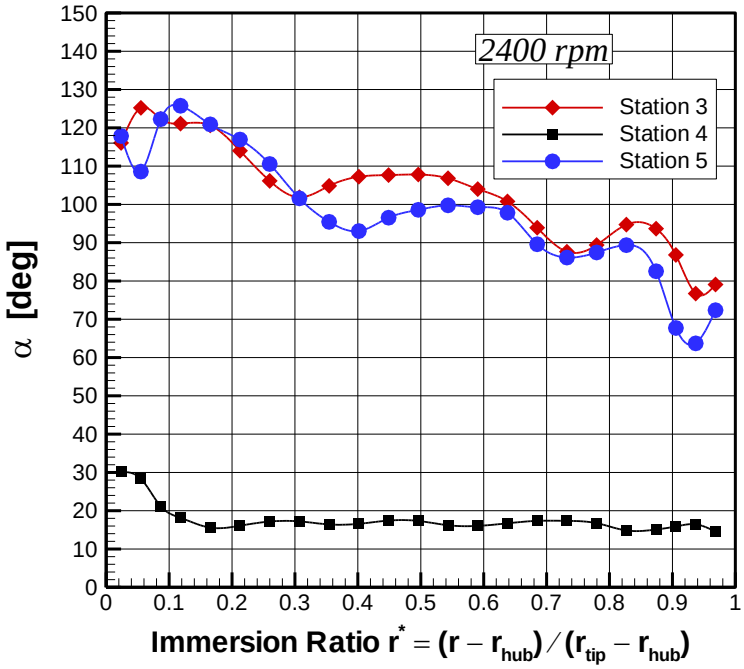

FigureA-14: Radial distribution of absolute flow angle at 2400 rpm

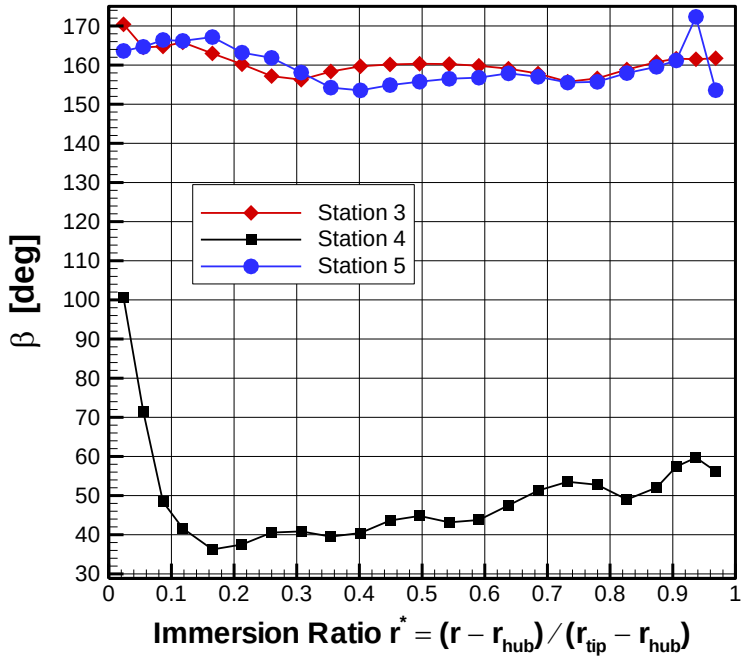

FigureA-15: Radial distribution of relative flow angle at 2400 rpm

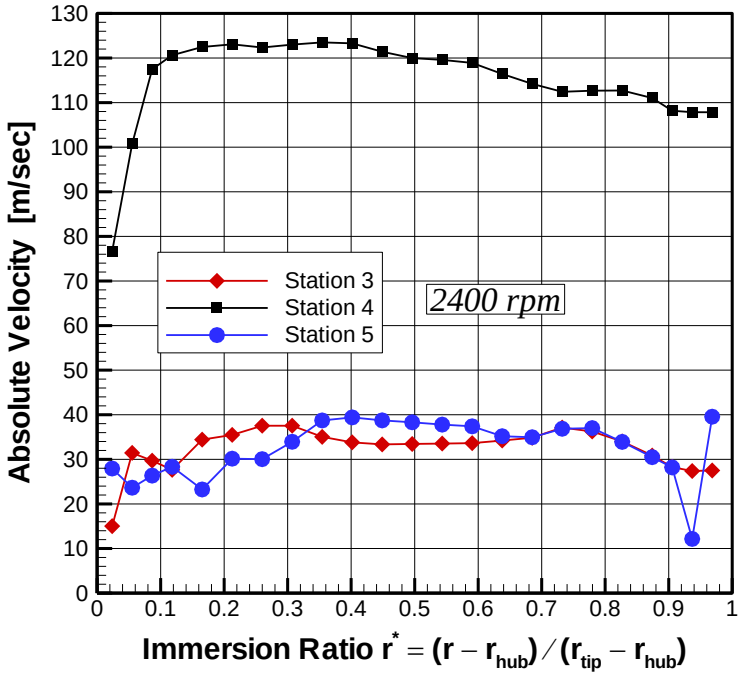

FigureA-16: Radial distribution of absolute velocity at 2400 rpm

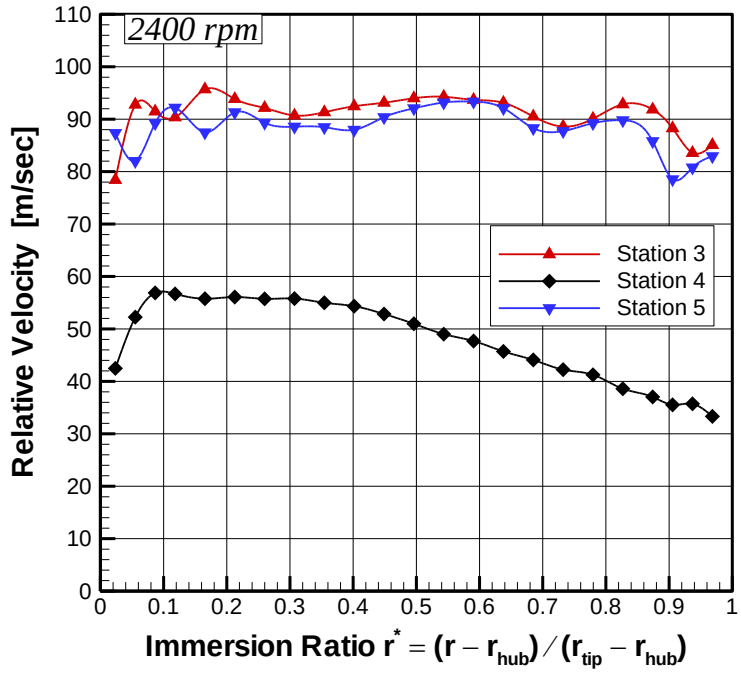

FigureA-17: Radial distribution of relative velocity at 2400 rpm

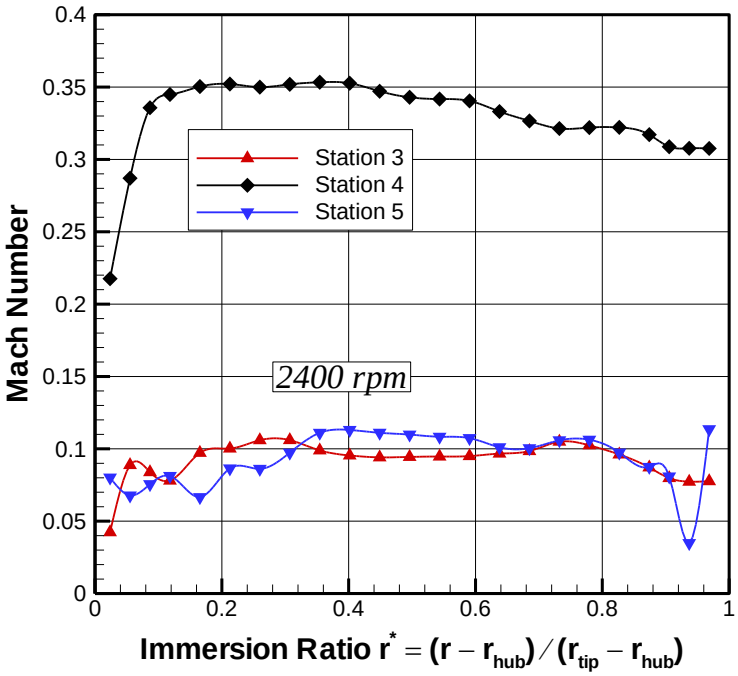

FigureA-18: Radial distribution of absolute Much number at 2400 rpm

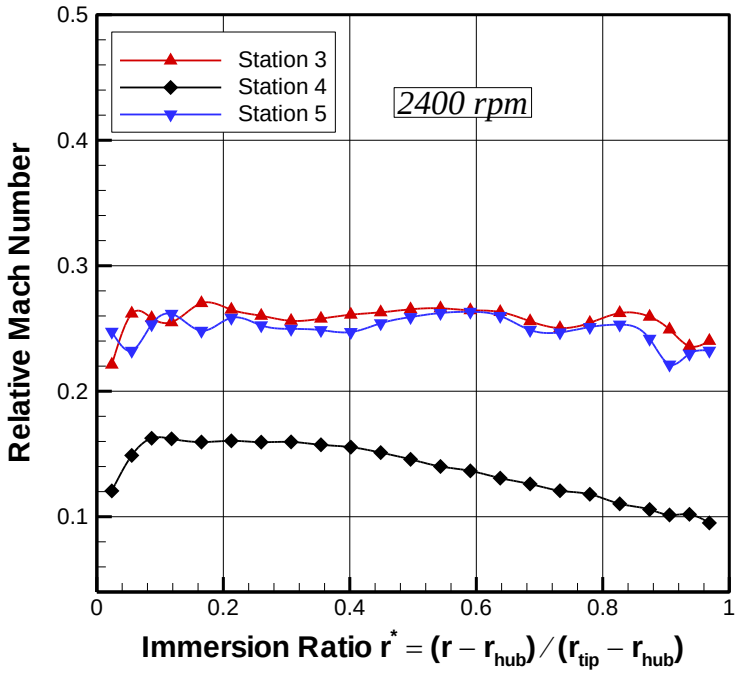

FigureA-19: Radial distribution of relative Mach number at 2400 rpm

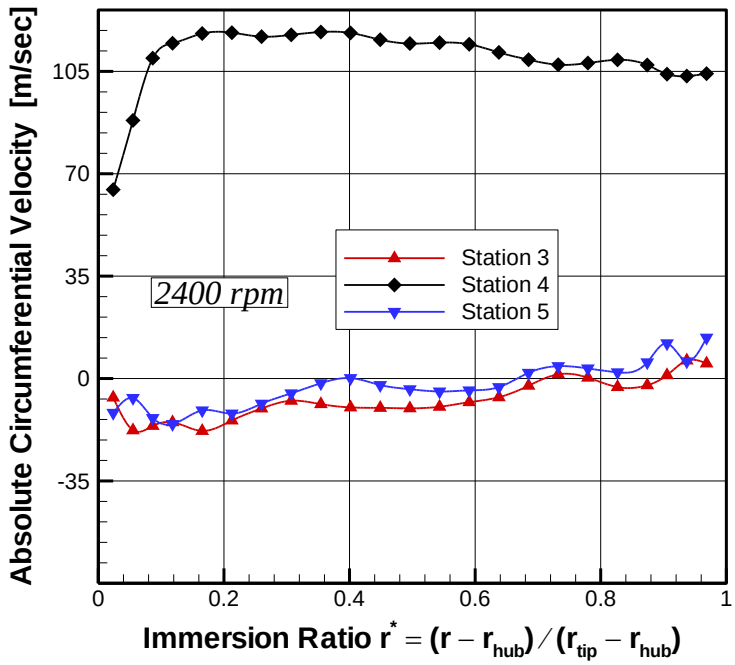

FigureA-20: Radial distribution of absolute circumferential velocity at 2400 rpm

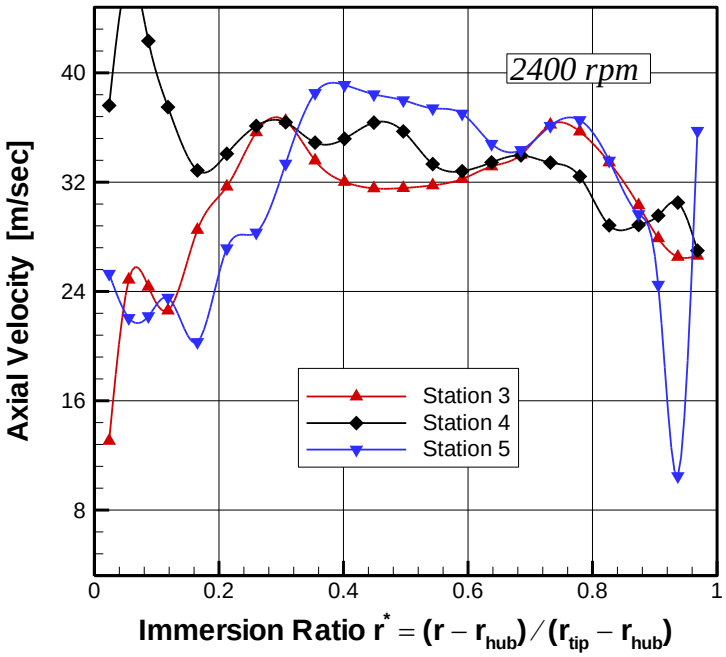

FigureA-21: Radial distribution of axial velocity at 2400 rpm

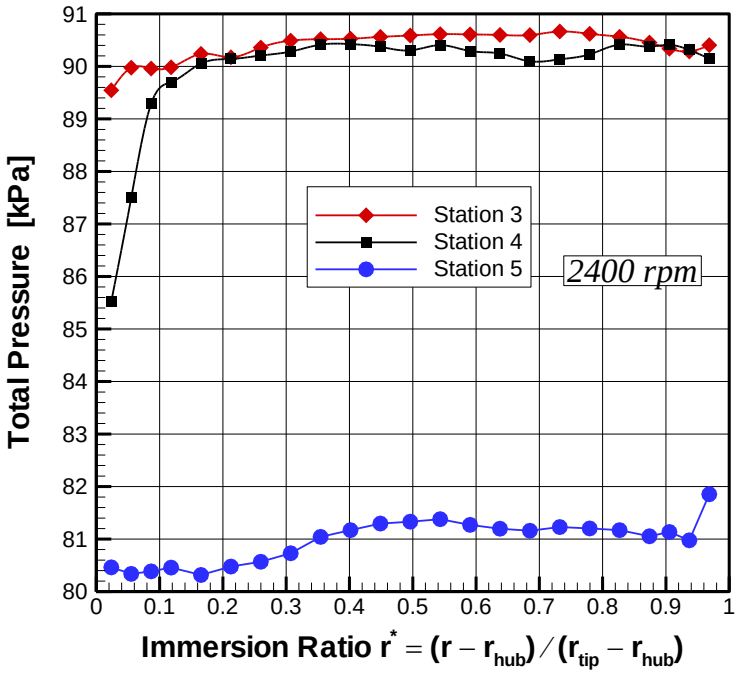

FigureA-22: Radial distribution of total pressure at 2400 rpm

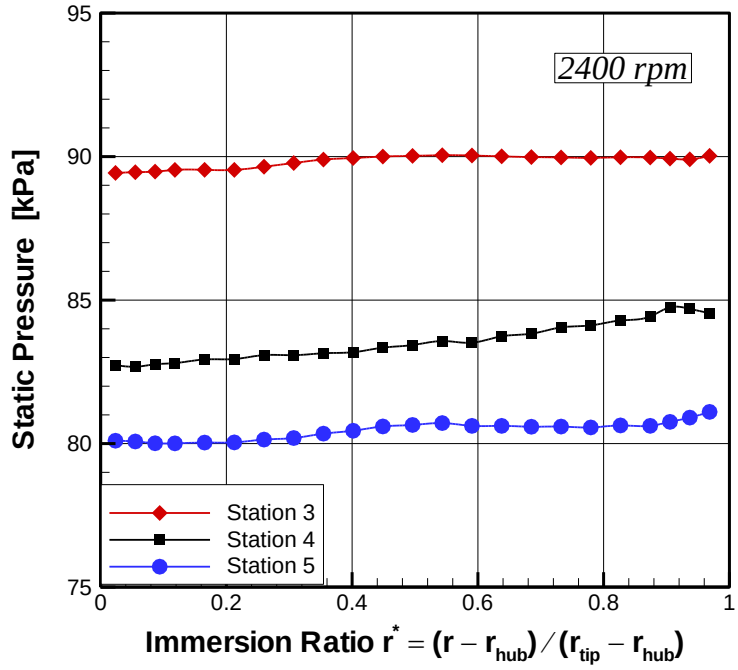

FigureA-23: Radial distribution of static pressure at 2400 rpm

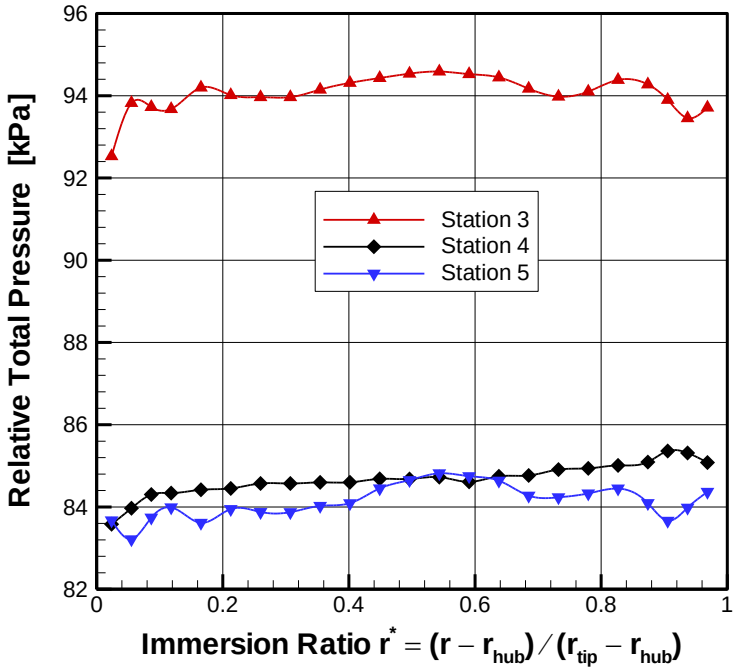

FigureA-24: Radial distribution of relative total pressure at 2400 rpm

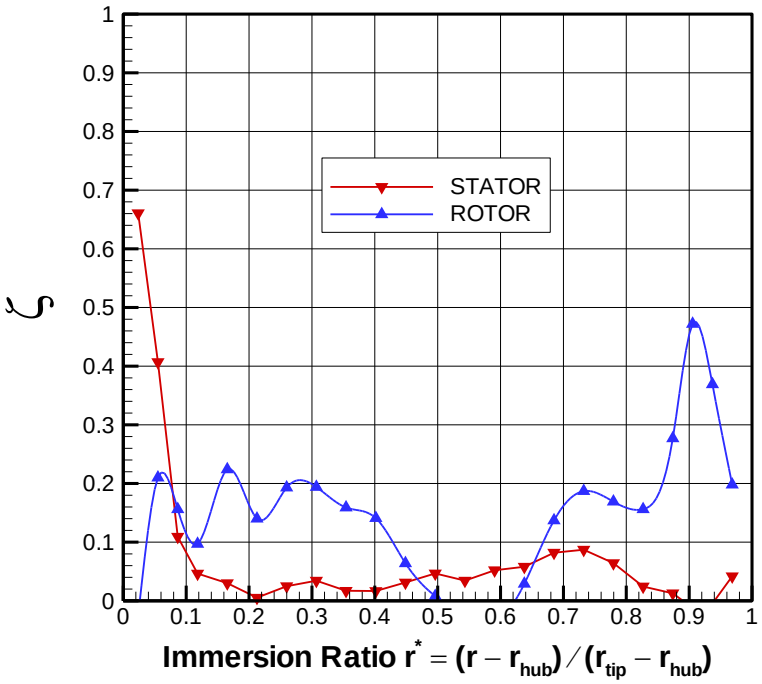

FigureA-25: Radial distribution of loss coefficient at 2400 rpm

APPENDIX B

PSP UNCERTAINTY ANALYSIS

From PSP calibration curve, we have polynomial equation:

$$y = Ax^3 + Bx^2 + Cx + D$$

From equation (19) we have:

$$\eta = \frac{\left(P_{O_2}\right)_{air} - \left(P_{O_2}\right)_{mix}}{\left(P_{O_2}\right)_{air}}$$

Film cooling effectiveness uncertainty calculated from:

$$\frac{\partial \eta}{\eta} = \left(\frac{n1p}{a1p - n1p}\right)\sqrt{\left[\left(\frac{\partial P}{P}\right)_{air}\right]^2 + \left[\left(\frac{\partial P}{P}\right)_{N_2}\right]^2} \qquad (24)$$

Where for air:

$$\left(\frac{\partial P}{P}\right)_{air} = \left(\frac{1}{a1p}\right)\left(\frac{\partial I}{I}\right)\left[3 * A\left(\frac{I_{ref}}{I_{a1}}\right) + 2 * B\left(\frac{I_{ref}}{I_{a1}}\right) + C\left(\frac{I_{ref}}{I_{a1}}\right)\right] \qquad (25)$$

For nitrogen:

$$\left(\frac{\partial P}{P}\right)_{N_2} = \left(\frac{1}{n1p}\right)\left(\frac{\partial I}{I}\right)\left[3 * A\left(\frac{I_{ref}}{I_{n1}}\right) + 2 * B\left(\frac{I_{ref}}{I_{n1}}\right) + C\left(\frac{I_{ref}}{I_{n1}}\right)\right] \qquad (26)$$

For example if we assume $\frac{\partial I}{I} = 0.5\%$, $\eta = 0.12$, a1p=1.0542, n1p=0.927, $I_{ref} = 181$, $I_{a1} = 172.406$ and $I_{n1} = 186.411$ then:

$$\left(\frac{\partial P}{P}\right)_{air} = 0.005981, \left(\frac{\partial P}{P}\right)_{N_2} = 0.006355$$

And therefore $\frac{\partial \eta}{\eta} = 6.36\%$

APPENDIX C

PSP MEASUREMENTS PROBLEMS

Camera program and calculate film cooling effectiveness based on PSP intensity are thoroughly explained in Arun's dissertation. In this section problems involved during endwall and blade tip cooling will be discussed.

Contoured endwall cooling: when the contoured ring was installed on the rotor, PSP was painted on the endwall and blades with tip cooling as shown in Figure C-1.

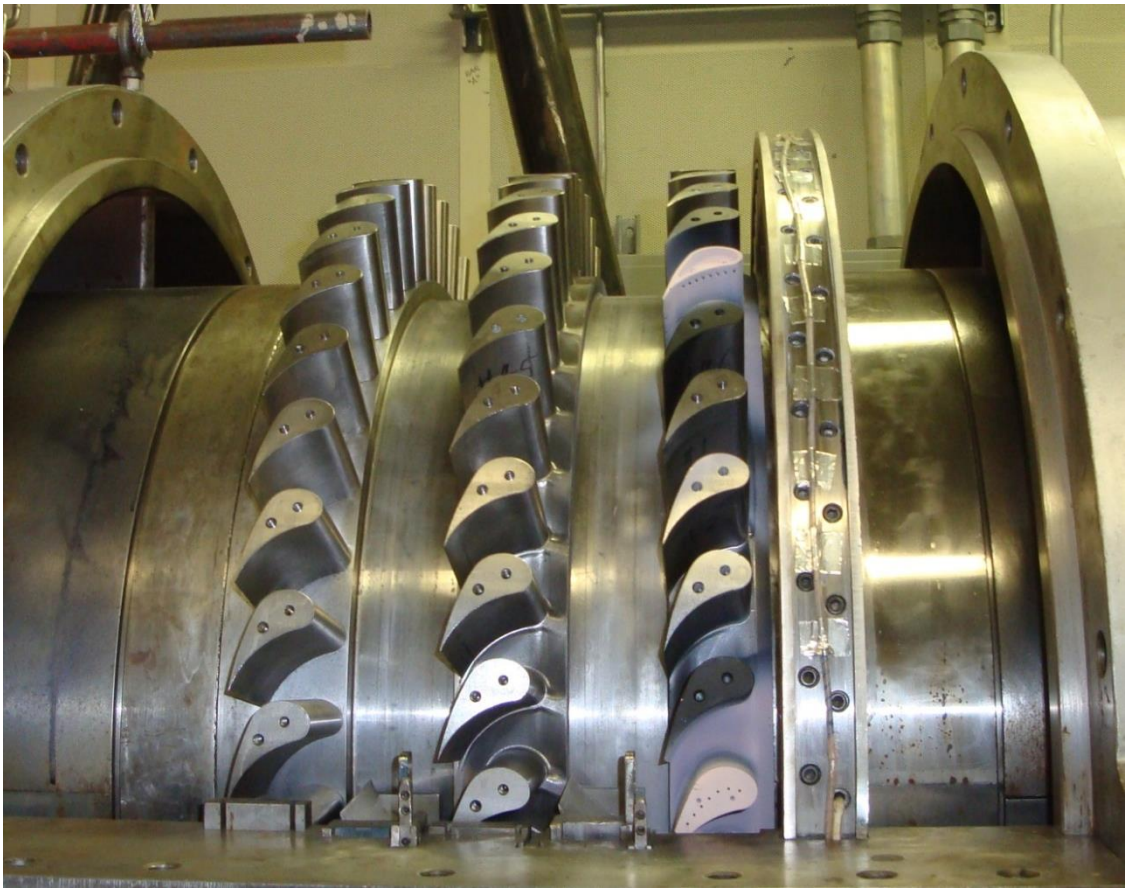

Figure C-1: blades and endwalls painted with PSP

Since the body of the blades next to the contoured endwall were painted as well, it was difficult to recognize the contouring effect alone and blade body was capture in the images. In order to solve this problem body of the blades next to the endwall, we wanted to take the measurement, were covered by tape and then PSP was painted on the endwall passage (Figure C-2)

Figure C-2: Covering the blades body by tape

Blade Tip cooling: main problem in blade tip cooling was calculating the true exit velocity at tip of the blades. The following procedure was done to calculate the true velocity and corresponding blowing ratio.

The schematic of the blade cooling system is shown in Figure below.

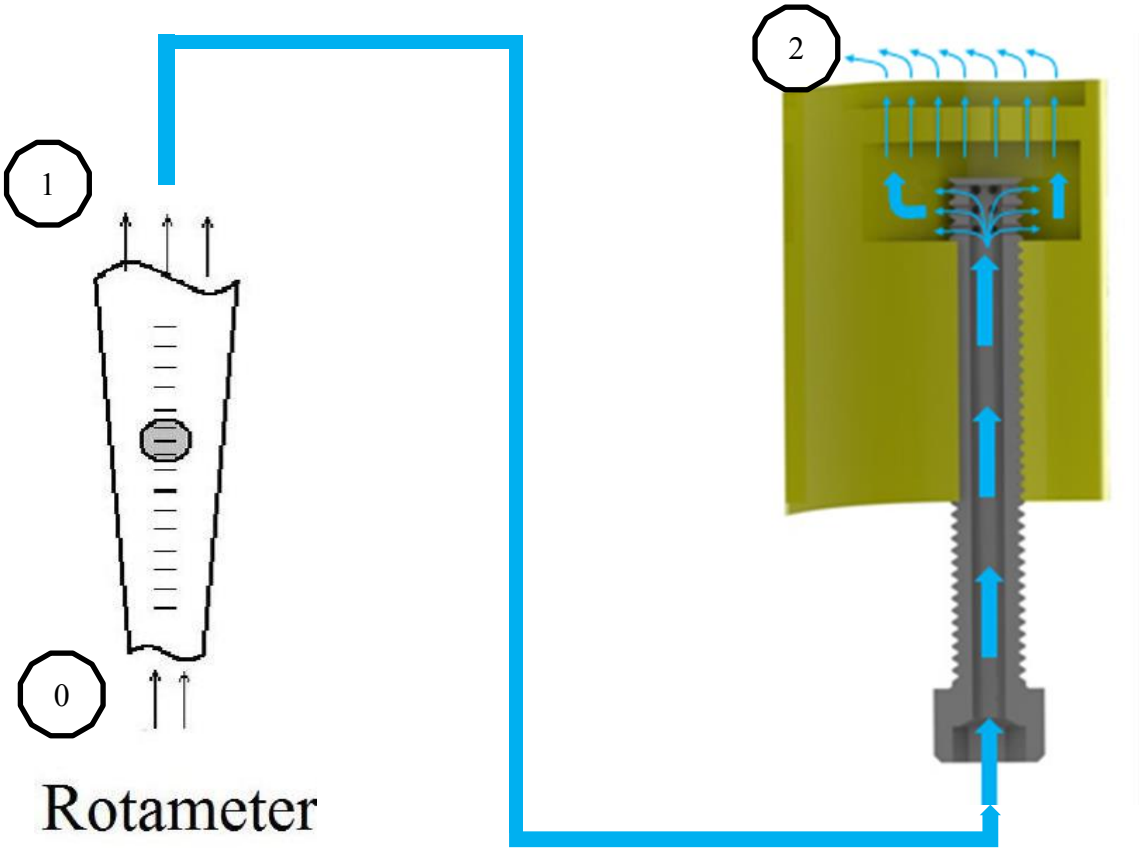

Figure C-3: Schematic of the blade cooling system

In this case that we have lots of pressure drop due to the complexity of the blade cooling system, it is needed to define the total pressure loss coefficient:

$$\zeta = \frac{P_{0_1} - P_{0_2}}{\frac{1}{2}\rho V_2^2}$$

Since the total pressure at 2 cannot be measured during experiment we can find total pressure loss at reference condition (no rotation) and then correct the loss coefficient for real case.

$$\zeta_{ref} = \frac{P_{0_1} - P_{0_2}}{\frac{1}{2}\rho V_2^2}$$

From literature if the Reynolds number of the blading under consideration is different from the reference Reynolds number at which the experimental measurements have been carried out, the loss coefficient must be corrected by the following relation:

$$\frac{\zeta}{\zeta_{ref}} = \left(\frac{Re_{ref}}{Re}\right)^m, with\ Re = \frac{\rho V_1 D}{\mu}\ and\ m = -\frac{1}{5} = -0.2$$

So in order to calculate the true exit velocity we should find ζ_{real}:

$$\zeta_{real} = \zeta_{ref}\left(\frac{Re_{ref}}{Re}\right)^{-0.2}$$

where

$$\zeta_{real} = \frac{P_{0_1} - P_{0_2}}{\frac{1}{2}\rho V_1^2}_{real}$$

Then

$$P_{0_2} = P_{0_1} - \frac{1}{2}\rho V_{1_{real}}^2 \zeta_{real}$$

Finally Velocity can be calculated based on total pressure P_{0_2} and Static pressure P_{s_2}:

$$V_{2_{real}} = \sqrt{\frac{2(P_{0_2} - P_{s_2})}{\rho}}$$

Results for different cooling flow are shown in Tables 1 and 2. (Static pressure at exit of holes= -5940 Pa)

Table C-1: Results for Reference condition (without rotation)

SCFM	V_1	Assuming no pressure loss		Actual data		
		V_2	BL	$V_{2\,Ref}$	BL	ζ_{ref}
10	8.12	61.19	1.03	37.70	0.63	0.88
15	12.09	91.10	1.53	53.43	0.89	0.86
20	15.94	120.09	2.02	71.97	1.20	0.83
25	19.72	148.52	2.49	86.37	1.44	0.82
30	23.32	175.64	2.95	103.27	1.72	0.80
35	26.78	201.75	3.39	119.36	1.99	0.78
40	29.96	225.68	3.79	139.60	2.33	0.75
45	32.92	247.96	4.16	158.68	2.64	0.74

Table C-2: Results for Real Condition for 3000 rpm

SCFM	V_1	Assuming no pressure loss		Real Data				
		V_2	BL	ζ_{real}	P_{0_2}	$P_{Dynamic}$	V_2	New BL
10	9.12	68.67	1.12	0.85	-14326.57	-8386.57	0	0
15	13.51	101.76	1.66	0.83	-12165.01	-6225.01	0	0
20	17.76	133.81	2.18	0.81	-9621.43	-3681.43	0	0
25	21.96	165.43	2.70	0.80	-7347.83	-1407.83	0	0
30	26.01	195.90	3.20	0.77	-4743.30	1196.70	48.25	0.80
35	30.02	226.13	3.69	0.75	-2701.71	3238.29	79.38	1.32
40	33.72	254.04	4.14	0.72	497.82	6437.82	111.92	1.87
45	37.30	280.95	4.58	0.71	4502.46	10442.46	142.54	2.38

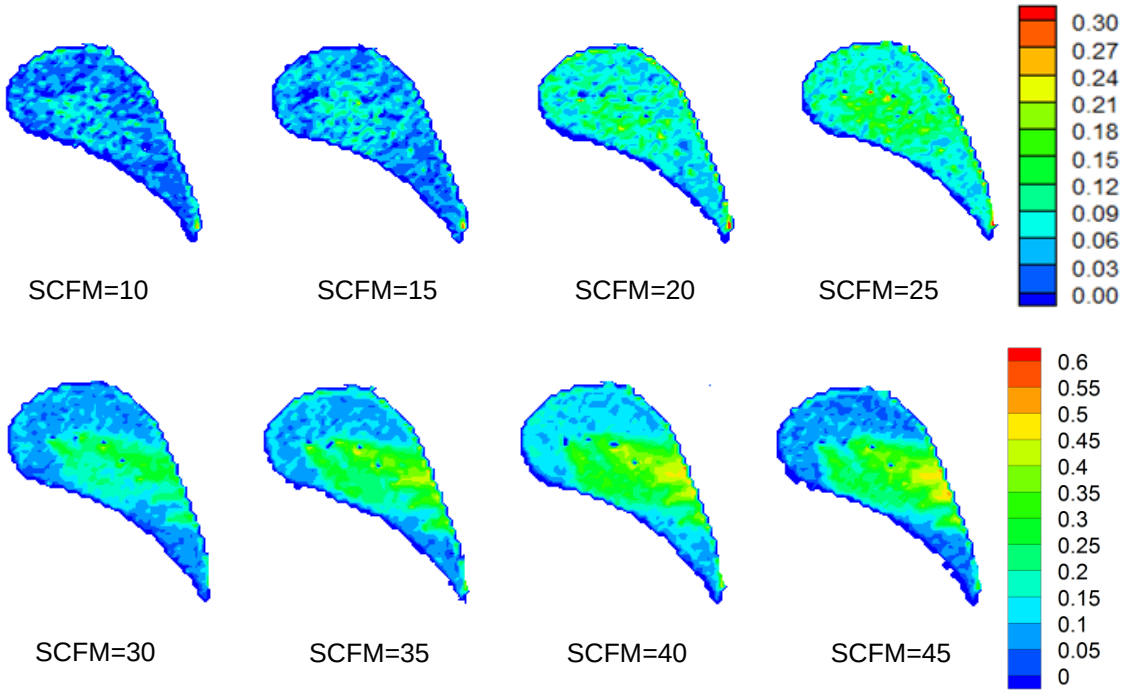

Figure C-4: Tip cooling preliminary results

Results from this calculation are completely adopted with film cooling experiment results. As shown in Figure 2, no flow is coming out from the holes when flow is less than 25 SCFM.

Figure C-5 shows blades painted with PSP and installed on the rotor. Figure C-6 depicts the optical setup used for film cooling effectiveness measurement.

Figure C-5: Four different blade configurations used in this study

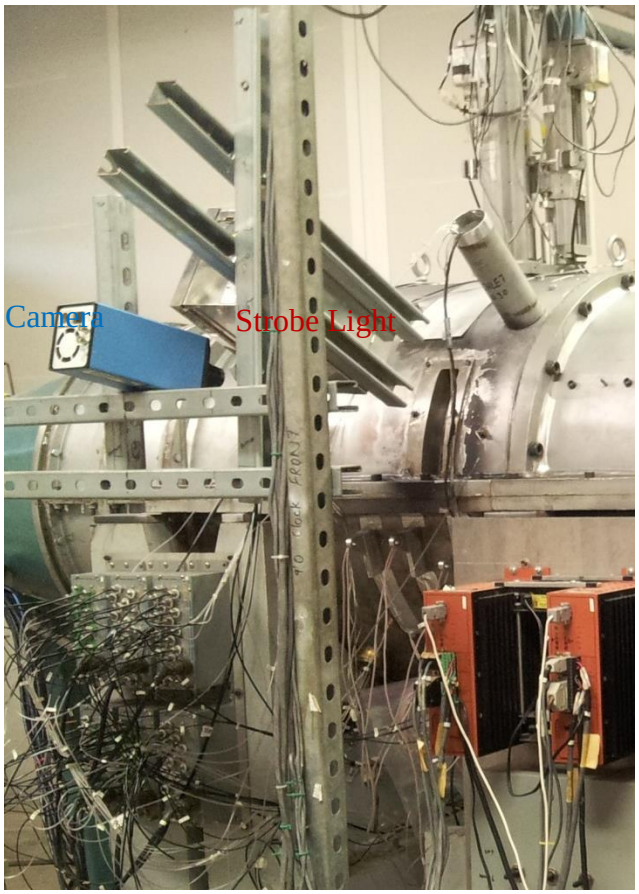

Figure C-6: PSP optical setup